UNIVERSITÀ DEGLI STUDI DI MODENA E REGGIO EMILIA

Dottorato di ricerca in Computer and Data Science for Technological and Social Innovation

Ciclo XXXVIII

IoT and Remote Sensing for Multi-Scale Monitoring of Livestock Effluents and Environmental Impacts in the Po Valley

Candidato Giovanni Triboli

Relatore (Tutor): Prof. Marco Picone

Correlatore (Co-Tutor): Prof. Marko Bertogna

Coordinatore del Corso di Dottorato: Prof. Andrea Marongiu

Contents

Abstract

Modern intensive agro-industrial and livestock farming practices, particularly widespread in the Po Valley, generate significant environmental pressures due to the large-scale production and dispersion of nutrient-rich effluents. The disposal of livestock waste through land spreading, although widely adopted, contributes—because of the excessive quantities involved—to the contamination of soil, surface and groundwater, and the atmosphere, making the monitoring and sustainable management of these processes highly challenging. This thesis presents the results of an in-depth state-of-the-art review addressing the issue of contemporary unsustainable industrial agricultural and livestock practices, as well as the critical environmental conditions of the territories affected by them. It proposes a coherent set of computational methodologies for environmental monitoring that combines process modeling, Internet of Things (IoT) architectures, simulation, and the analysis of territorial data provided by satellite-based remote sensing platforms.

Subsequently, a systematic analysis of the operational phases associated with livestock waste management is presented, culminating in the design and prototyping of an IoT architecture for the real-time monitoring of transport and spreading operations. To support the development and validation of this architecture, a simulated environment is introduced to reproduce waste dissemination activities in the Po Valley, including an emulator of drivers' op-

erational behaviors aimed at identifying critical issues and system limitations prior to real-world deployment. Based on this framework, a fully functional prototype was subsequently developed to support traceability, continuous data collection, and interoperability among sensors, vehicles, and control systems.

In parallel, the thesis investigates the downstream effects of excessive nutrient inputs on surface water systems, focusing on eutrophication phenomena, macrophyte growth, and turbidity variations. Automated tools based on satellite imagery are presented, integrating well-established remote sensing indices for vegetation, water, and turbidity with cloud-filtering techniques and post-processing steps. Applications to real-world case studies in the Po Valley demonstrate the ability of the proposed processing pipelines to quantify complex spatiotemporal dynamics along lakes and river courses. These results are achieved through the combined use of satellite raster data and georeferenced vector data from open sources, together with the application of original spatial segmentation and aggregation techniques tailored to these specific contexts.

Overall, the contributions presented in this thesis outline a unified methodological framework for the development of scalable and integrated digital tools for environmental monitoring, providing scientific, operational, and decision-support capabilities for the sustainable management of agro-livestock practices and their impacts on ecosystems, as well as for the generation of datasets suitable for subsequent studies.

Chapter 1

Introduction

More than two-thirds of the Earth's surface is covered by water, which constitutes one of the most critical natural resources for sustaining life and ecosystem functioning. Despite the widespread recognition of its importance, anthropogenic activities continue to compromise water quality through the pollution of rivers, lakes, and oceans. As a result, freshwater is increasingly becoming a scarce resource on a global scale, particularly in terms of supplies that meet acceptable physicochemical and microbiological quality standards. Over the past several decades, freshwater systems—lakes and rivers—have been progressively affected by eutrophication processes, primarily driven by elevated concentrations of nitrogen and phosphorus compounds—most notably nitrates and phosphates—originating from human activities such as intensive agriculture, urban effluents, and industrial discharges.

1.1 Context

The research described in this thesis concerns the surface water bodies of the Mantua area in Northern Italy. Water is the environmental resource that

(a) Livestock

(b) A farm

Figure 1.1: Examples of so-called Concentrated Animal Feeding Operations (CAFO). These structures are widespread in the Po Valley and the harmful excretions of the animals raised here are dispersed throughout the territory.

most characterizes the territory surrounding the city, which is encircled by three lakes, as described in [79], traversed by the Mincio River, and interlaced with a network of canals and marshy zones. These water bodies are subjected to nutrient enrichment, primarily caused by persistent poor agricultural management and excessive use of fertilizers, which negatively affect aquatic ecosystems, navigation, and hydrogeological stability. Industrialized Western countries, particularly those with intensive agricultural practices, generate considerable amounts of polluting waste [9]. The Po Valley represents a critical hotspot, particularly in the Lombardy region. Although it covers only 5% of the national territory, it hosts 48% of the eight million pigs raised in Italy [1].

Indeed, among modern food production techniques, intensive livestock

[1](Anagrafe Zootecnica Regionale: banca dati regionale (BDR) (2025)): https://www.regione.lombardia.it/wps/portal/istituzionale/HP/DettaglioServizio/servizi-e-informazioni/imprese/imprese-agricole/zootecnia/servizi-di-veterinaria-per-la-zootecnia/anagrafe-zootecnica/anagrafe-zootecnica

(a) A tank lorry.

(b) Another tank lorry.

Figure 1.2: Wastewater spills on agricultural fields. Fertigation is the traditional way of disposing of wastewater, regardless of the consequences.

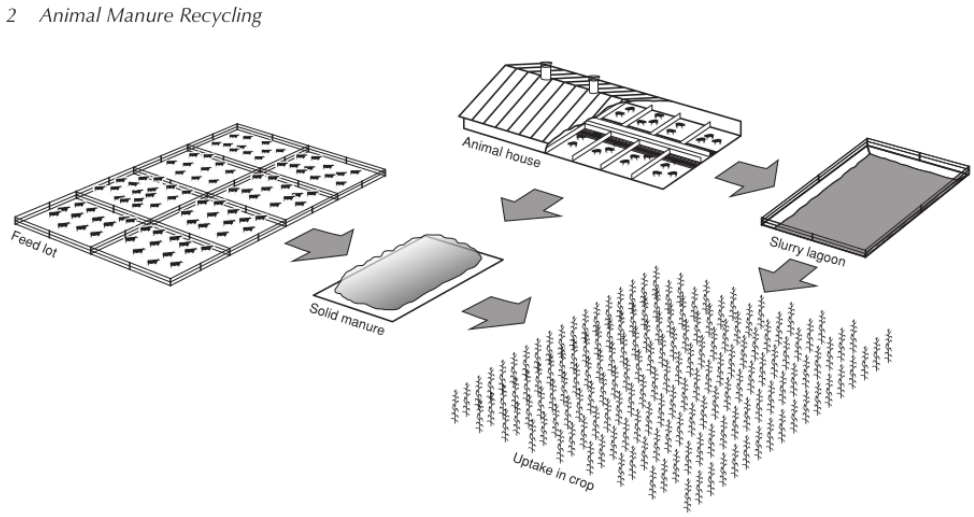

Figure 1.3: Animal manure management (bold arrows) is a chain of interlinked operations and technologies, of which the major steps are collection of excreta in animal houses or beef feedlots, storage of manure in-house and/or outside, treatment of the manure (not shown), transport to fields and spreading in the fields. At each stage there is a risk of emission of components, which represents a loss to the farmer and a risk to the environment. (Source [64]).

(a) The shot includes the entire area affected by eutrophication

(b) Detail on the vegetation carpet

(c) Detail on sedimentation

Figure 1.4: Critical situation at the confluence with the Osone, a drainage channel, near Rivalta sul Mincio. (a) The confluence : Osone flows into the Mincio. The incoming waters are very cloudy; (b) Invasive macrophytic vegetation tends to obstruct the passage.; (c) Sedimentation is highlighted by the profile graph of the riverbed, in the immediate vicinity of the river outlet.

farming is one of the most significant sources of environmental problems; so much so that it has become a subject of interest for the research community, which has begun to address these critical issues using innovative tools recently made available, including IoT and satellite imagery. Livestock farming has now taken on the characteristics of a true industry, concentrating a large number of animals in confined spaces, as shown in 1.1.

It represents an important economic factor and contributes to financial well-being; however, it produces a large amount of by-products, the disposal of which is difficult. Over time, no alternative methods have been devised for the disposal of pig slurry other than spreading it on fertile agricultural land; some examples are reported in Figure 1.2. This is why, every day, a fleet of tank trucks crosses the territory with the mission of transporting it from farms to designated fields. The entire process is described in [64] and illustrated in Figure 1.3.

The authors of [62, 2, 76] study the effects of manure and fertilizers on soil fertility and quality, highlighting the importance of essential nutrients for sustainable crop production and discussing how repeated applications of livestock manure can impact soil composition. The manure is very rich in nutritious nitrates, which must be used wisely to prevent it from contaminating the water system as a consequence of runoff or leaching episodes, as portrayed in Figure 1.8.

So much so that the European Commission enacted a specific Water Directive in 2000, which the agri-livestock industry was required to comply with. A scientific workshop [51], where nearly a hundred posters were dedicated to efficient nitrate management, was held in 2006. The fertigation technique can benefit crops if synchronized with the plants' nutrient needs, typically during the summer. On the contrary, untimely or excessive distribution [14] leads to

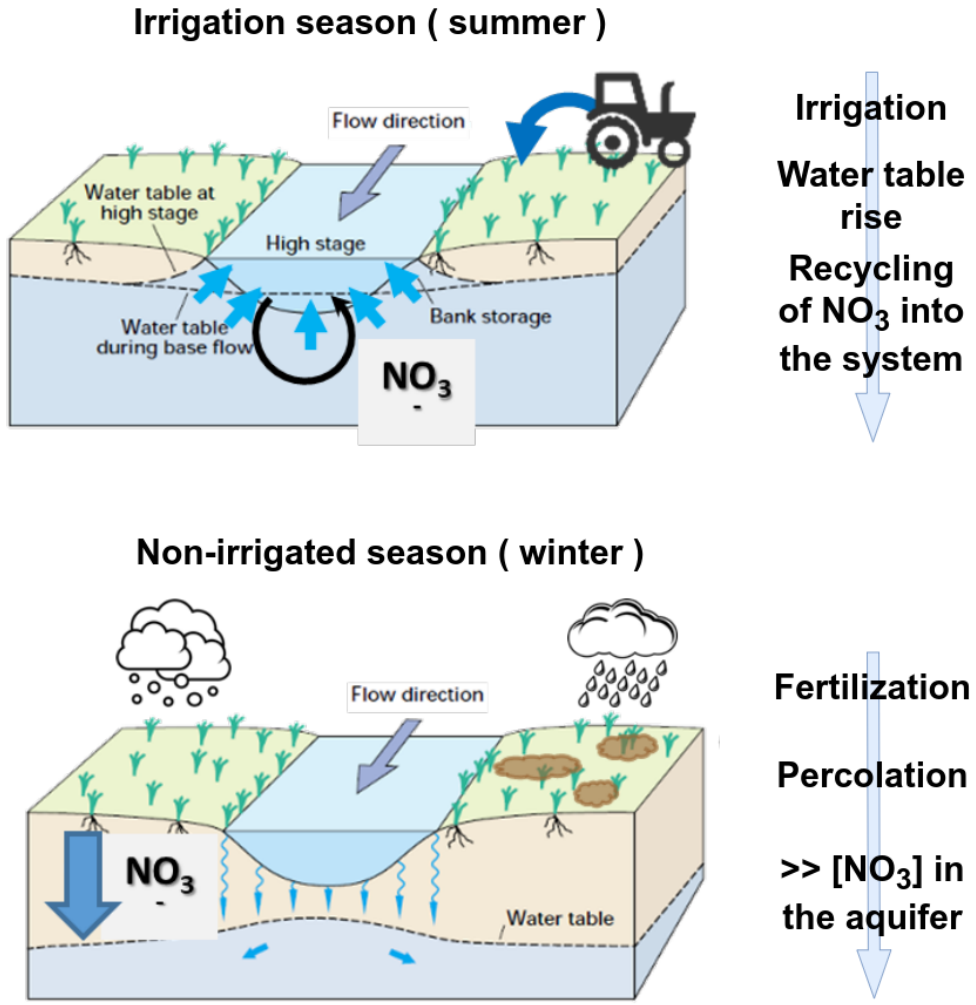

Figure 1.5: The irrigation loop and its effect on nitrates (Source [5]). Irrigation and rainfall bring fertilizing nitrogen to waterways, a boost for wild vegetation.

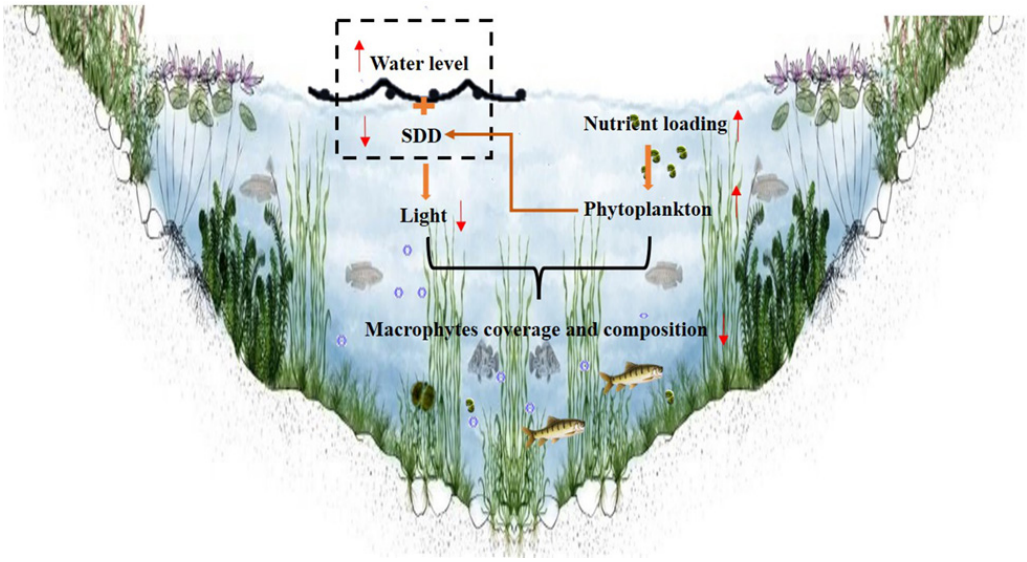

Figure 1.6: Nutrient loading in the ecosystem of a surface water body (Source [15]). Phytoplankton presence is measured with Secchi disk depth (SDD). The present thesis aims to correlate nutrient overload with the proliferation of floating vegetation species.

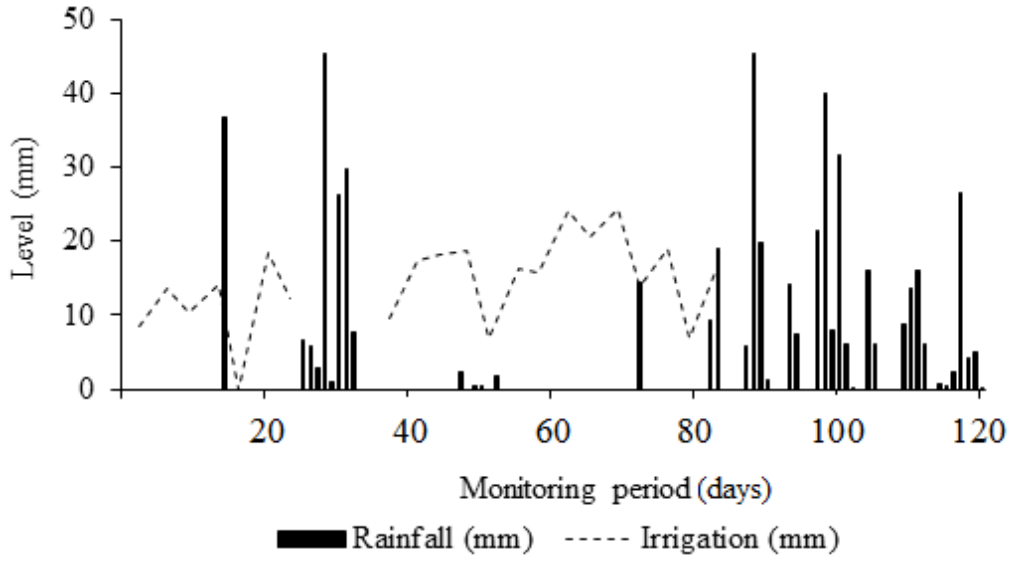

Figure 1.7: The experiment conducted in [47] considers the influence of rainfall and irrigation on the effects of agricultural activities on the territory.

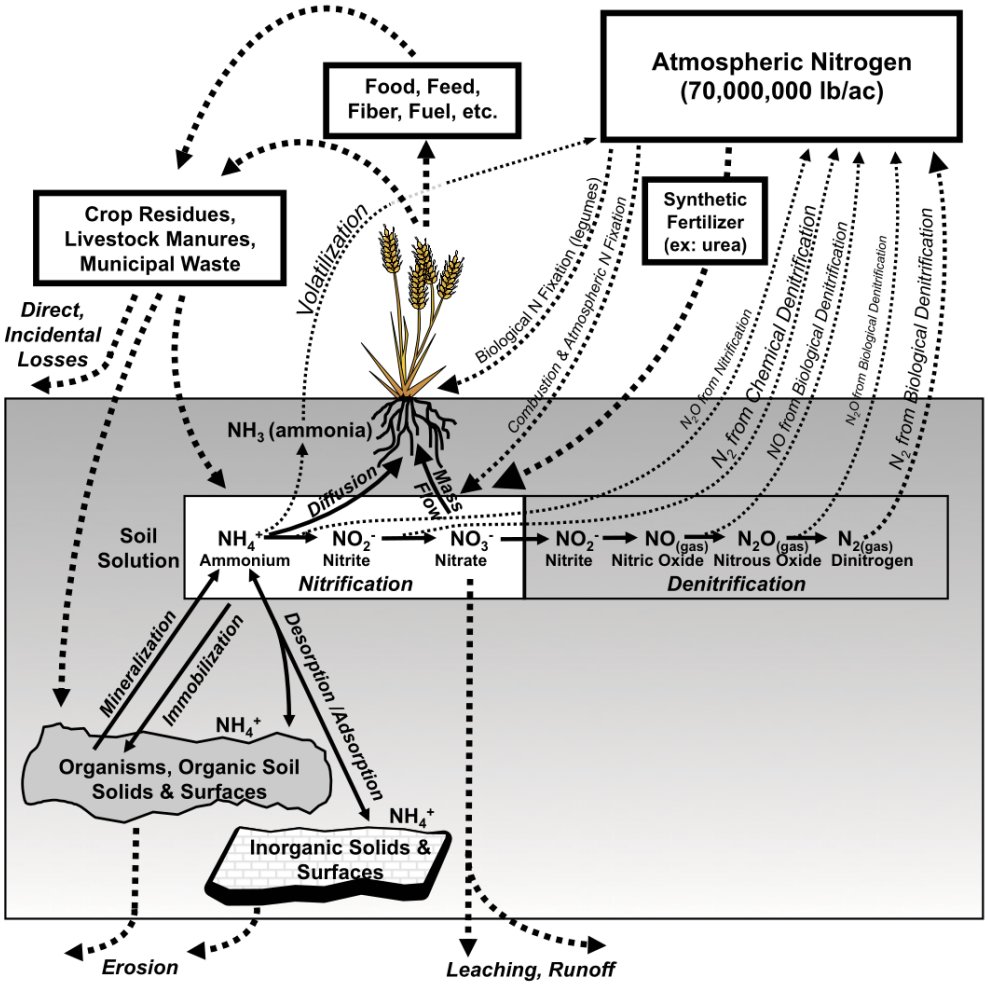

Figure 1.8: The N cycle. Nitrogen behaviour in soil is complex and dynamic, with many forms, transformations and potential losses. Dashed lines represent N gains or losses in the soil system; solid lines represent internal transformations within the soil system (Source [62]).

severe environmental pollution [33], given the complexity of the path taken by manure to become an effective nutrient for crops, illustrated in Figure 1.9.

A critical problem lies precisely in the seasonal imbalance between manure production and the soil's absorption capacity. European Union (EU) regulations prohibit the winter spreading of livestock effluents [12], as impermeable soils during this period can cause pollutant volatilization and contribute to atmospheric particulate matter, as reported in the study [20] and [2]. These regulations require manure storage until February, after which large-scale spreading resumes. The nitrogen contained in liquid manure is more volatile [65] than that in synthetic fertilizers, with a substantial portion infiltrating the soil along with bacteria [3], carried by irrigation and rainfall [50], as illustrated in figure 1.5. In [47], the authors attempted to measure the effect of rainfall and irrigation during the period of their experiment, as reported in Figure 1.7, on manure percolation into the soil. The nutrient overload in a lacustrine ecosystem, such as the one illustrated in Figure 1.6, is presumably responsible for the proliferation of floating vegetation species.

Part of the nitrogen contained in the slurry, once spread on the ground, reaches the aquifer [50] [3] as reported in Figure 1.10; however, the most evident impacts of these nutrients are observed on the surface, in rivers and lakes [33, 26], where they promote the excessive growth of aquatic vegetation and are potentially dangerous, as the authors of [6] argue and state in the table in Figure 1.12. It is reasonable to hypothesize that part of the wastewater spread on the fields ultimately drains into the river, where a mass of suspended

[2]LEGAMBIENTE - MAL'ARIA DI CITTÀ (2025): `https://www.legambiente.it/wp-content/uploads/2021/11/MalAria-2025.pdf`

[3]ISPRA - NITRATI NELLE ACQUE SOTTERRANE (2020): `https://indicatoriambientali.isprambiente.it/it/acque-interne/nitrati-nelle-acque-sotterranee`

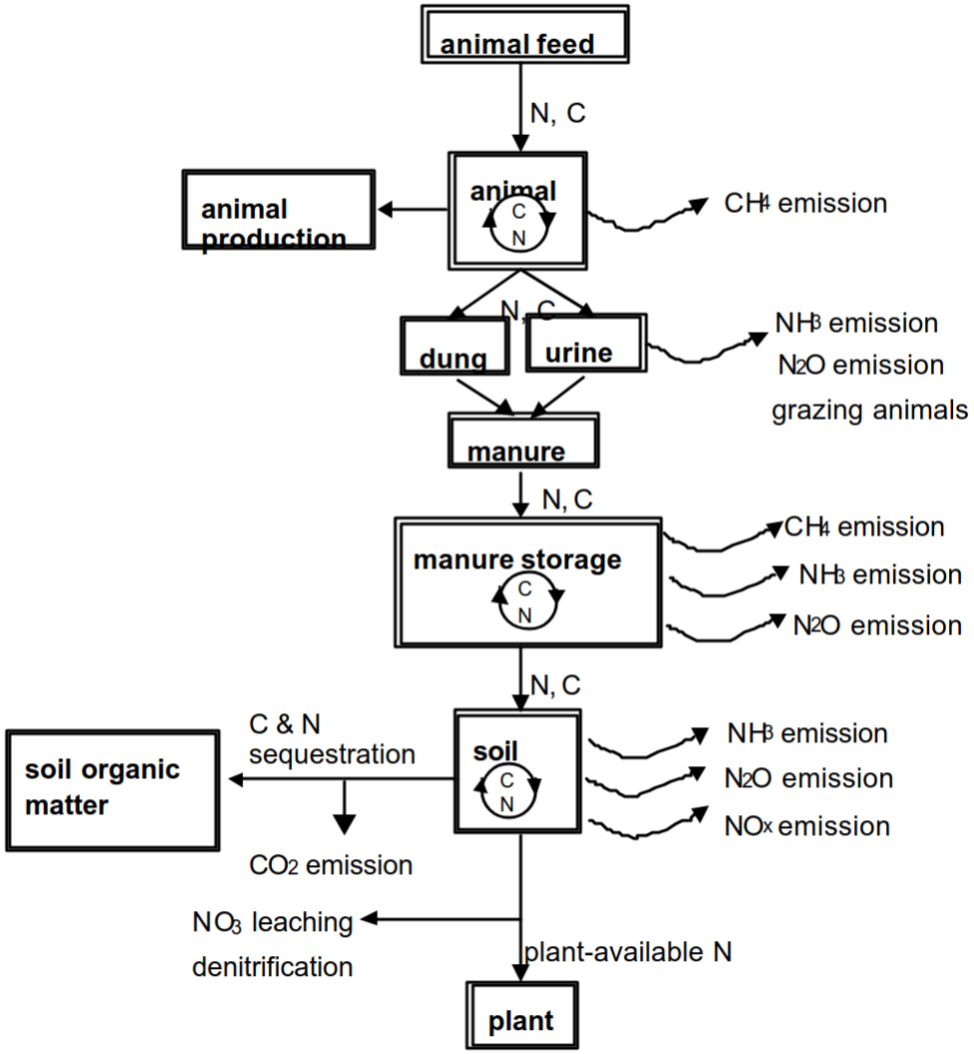

Figure 1.9: Schematic presentation of the Carbon (C) and Nitrogen (N) flows in the chain animal feed – animal - dung/urine – stored manure – soil – plant, showing that the composition of the animal feed affects the agricultural (C and N sequestration, plant-available N) and environmental (NH3, N2O, NOx and CH4 emission and NO3 leaching) performance of manure (Source [78]).

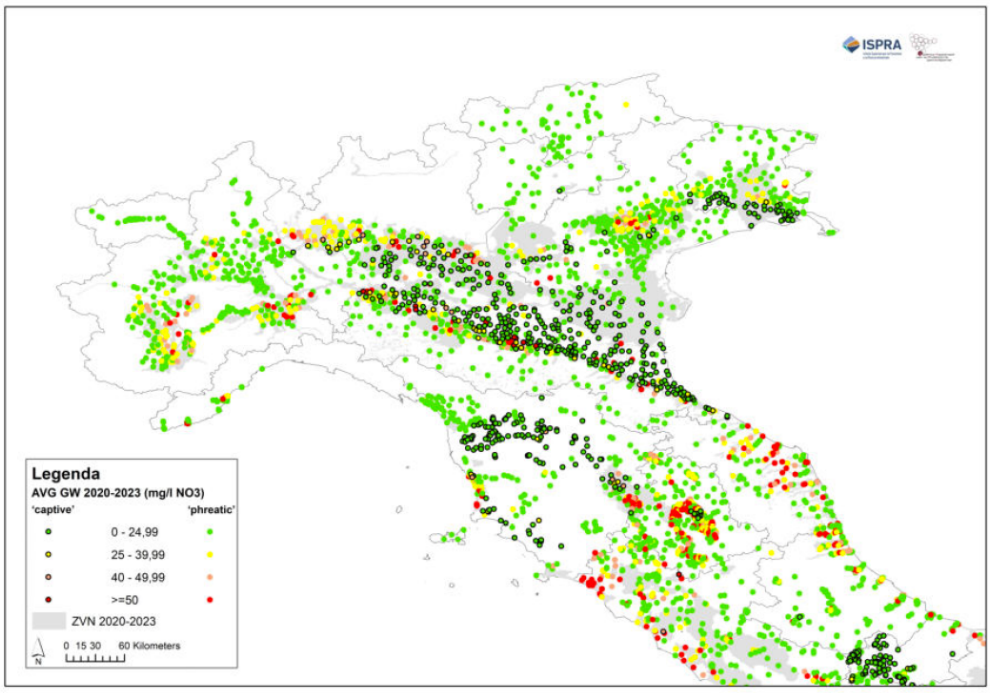

Figure 1.10: Nitrate pollution linked to intensive livestock farming in central and northern Italy. ISPRA-Sintai report with average concentration values at groundwater monitoring sites for the four-year period 2020-2023. Groundwater in Lombardy, Emilia, and Veneto shows nitrate concentrations exceeding legal limits (50 mg/l), especially in areas with high pig and poultry density.

(a) The invasive green carpet occupies a large part of the body of water.

(b) Note the cuts made in the vegetation to allow navigation.

(c) The cuts are also visible in the satellite image.

Figure 1.11: The summer greenery that grows abnormally in two areas of Lake Superiore di Mantua (source: Gazzetta di Mantova) is a consequence of the nutrient-rich waters of anthropogenic origin.

Parameter	Unit	Average	NOM-001/USDA	Water Bodies	Soils
pH value		7	6-9	-	b
EC*	dS m^{-1}	4.04	0.75	X	XXX
BOD**	mg L^{-1}	3946.17	150	XXX	b
COD***	mg L^{-1}	9960.83		XXX	b
Phosphates	mg L^{-1}	8.71		P	B
Bicarbonates	mg L^{-1}	137.45		I	X
Chlorides	mg L^{-1}	138.35	106.36	I	XXX
Sulphates	mg L^{-1}	34.04		P	I
Nitrogen	mg L^{-1}	806.4	40	P	B

X=harmful, XX= very harmful, XXX= extremely harmful, b= beneficial, B= very beneficial, I= indifferent and P= potentially dangerous; EC*, electrical conductivity; BOD**, biochemical oxygen demand; COD***, chemical oxygen demand.

Figure 1.12: Characteristics of swine wastewater and its positive and negative, albeit significant, effects on soil and water bodies (Source [6]).

particles may cause sedimentation events that are hazardous for navigation and accelerate the natural process of riverbed infilling through deposition, as illustrated in Figure 1.4 and suggested by a research group at the University of Parma, which has studied this phenomenon [5]. Sedimentation phenomena can create navigation difficulties, especially during dry seasons, as demonstrated in the figure, and they can increase flood risks.

These processes occur spontaneously in nature on a secular timescale; however, acceleration is observed due to human intervention, which discharges waste from agricultural and livestock production activities into the hydrographic network. The lakes surrounding Mantua (in Italy), as reported by local media [4] and shown in Figure 1.11, experience an abnormal summer proliferation of macrophytes due to the shallow and slow waters—conditions similar to those described in [73, 38].

Such vegetation, which develops at the water surface, limits sunlight penetration and reduces the oxygen available in deeper layers, thus threatening aquatic life [87]. To reduce nitrate input, redistributing livestock across other

[4]YouTube Gazzetta di Mantova (2022): `https://www.youtube.com/watch?v=pzihTLucPVA`

Experimental animals used	Reduction of dietary CP levels (%)	Reduction of N in animal manure (%, dry matter basis)	References
Growing-finishing pigs	3–4	35–45	Dourmad *et al.* (1993); Canh *et al.* (1998)
Swine	No data	25–30	Lenis (1989); Hartung and Phillips (1994)
Broilers	3–4	10–27	Blair *et al.* (1999)
Broilers	2–4	12–17	Wang *et al.* (2014); Zeng *et al.* (2015)
Layers	3.5	30–35	Blair *et al.* (1999)
Turkeys	10	16	Parks *et al.* (1996)

Figure 1.13: Reducing concentrations of nitrogen (N) in animal manure through reducing dietary crude protein (CP) levels and adding synthetic amino acids to diets (Source [37]).

territories could be helpful; however, it remains economically unfeasible and logistically difficult, partly because a large part of Italy is unsuitable for livestock farming due to orographic reasons. Alternatively, several mitigation strategies can be applied; the following are the most promising: It has been demonstrated that manure composition depends on the animals' diet and metabolism [78]; nutritionists recommend low-nitrogen diets to breeders [37] to obtain a significant reduction of nitrogen (N) in animal manure, as shown in the table in Figure 1.13. At the same time, veterinarians focus on the genetic selection of livestock to ensure consistent growth performance [31].

Another approach is to solidify manure using technologies that incorporate zeolite to improve nitrate retention in the soil [41], producing excellent soil conditioners for horticultural use. In [54] the authors demonstrate that an increase in plant cultivation density corresponds to an increase in nitrogen use efficiency and a reduction in the drainage of nitrates used as fertilizer. Other studies focus on integrated crop and animal farming and the decreased use of external inputs in food and agriculture [46] to limit the escape of nitrogen, which can also increase greenhouse gas emissions. They conclude that the global potential for nitrogen availability through recycling and nitrogen fixation is far greater than the current production of synthetic

Nitrogen derived from industrial production (by the Haber-Bosch process with fossil fuel combustion)	90 to 100 Mt N per year	Erisman, *et al.*, 2008, IFA, 2009
Potential nitrogen production by leguminous plants via intercropping and off-season cropping (without competing cash crops). This potential is not used by conventional farmers.	140 Mt N per year	Badgley, *et al.*, 2007
Nitrogen from livestock faeces of 18.3 billion farm animals (FAO, global figure). In specialized farming structure with strong segregation between crop and livestock production, nitrogen from manure and slurry is inefficiently used.	160 Mt N per year	Estimated by the authors

Figure 1.14: Global nitrogen input and nitrogen circuits in agriculture (Source [46]). The quantities involved are significant and have unavoidable and significant impacts.

nitrogen, as shown in the table in Figure 1.14.

Additionally, a set of practices known as "Precision Livestock Farming,", illustrated in Figure 1.15, has proven to be effective mitigation tools [72].

The use of planning tools can better align manure application with crop absorption, taking into account soil conditions, weather, storage, and fleet logistics [6]. IoT integration can further optimize and certify application processes, as demonstrated by the research I conducted in my second year of study [70, 69].

1.2 Research Objectives

The present doctoral research is grounded in, and has been motivated by, these identified environmental criticalities. This thesis presents the scientific contributions achieved within the scope of my expertise in data science, along with the underlying motivations and the specific research objectives pursued. The research topics investigated during my doctoral studies are outlined below

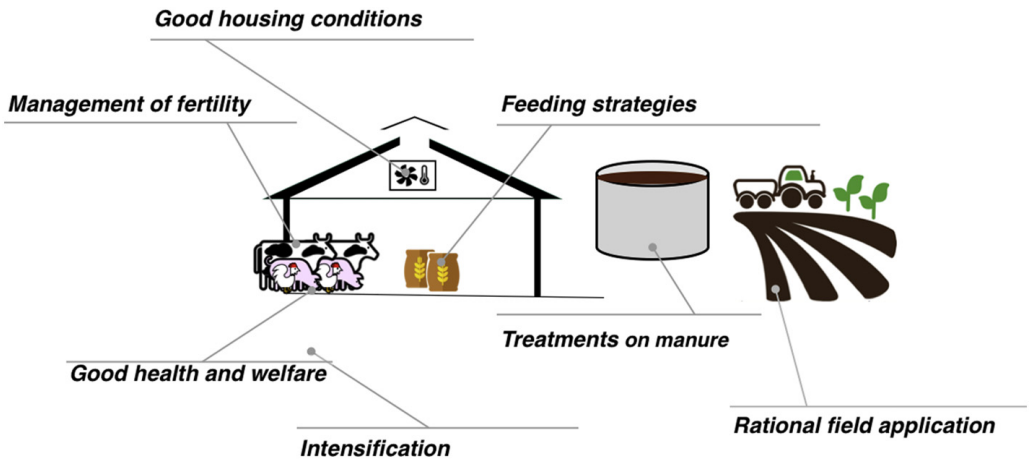

Figure 1.15: Current mitigation strategies adopted in Precision Livestock Farming (Source [72]). Proper feeding of livestock and effective waste disposal are the keys to a lower environmental impact.

and constitute the core subjects of the subsequent chapters.

The first objective pursued was to investigate the macroscopic episodes of vegetative colonization that occur regularly in Lake Superior (Mantua, Northern Italy). For this purpose, a feasibility study was initiated on a low-cost IoT (Internet of Things) sensor network for monitoring the six most important aquatic environmental parameters: turbidity, chlorophyll, pH, dissolved oxygen, water temperature, and electrical conductivity. This study highlighted obstacles that prevented the creation of a fully operational application, which has been postponed to a later time pending more favorable conditions. However, the study revealed the potential of the investigated technologies.

As the research progressed, the livestock industry emerged as a significant actor, jointly responsible for these issues. A reflection on how to reduce its impact led to the creation of a solution for the precise tracking of livestock waste spreading missions in the territory of Mantua and the surrounding

provinces, as well as optimized planning and guided support for tank truck drivers. The previously envisioned IoT technology proved crucial in completing this task, which aims to collect effective data to assess the impact of operations and minimize waste and harmful emissions while reducing operating times and costs in compliance with European and local regulations. The system was tested in pilot missions, demonstrating promising usability potential.

While awaiting and hoping that this "mission tracker" will be evaluated for adoption by the stakeholders of the agri-livestock supply chain, as well as by the authorities responsible for territorial control, a final research direction emerged that connects with the previous themes: the development of a procedure for acquiring remote sensing indices calculated from satellite images comprising the lake [71] and river waters for the years 2023 and 2024, and the presentation of the results in tabular and graphical form. The innovative aspects of this part of the presented research are listed in the 2.1 list.

In conclusion, IoT technology, both distributed and punctual, was initially employed to perform a fine-scale analysis of agri-livestock pollution phenomena through on-site environmental sensors and, subsequently, to act on the reduction of the pollutant load generated by productive activities. In the later works carried out on a broader territorial scale, remote sensing techniques were applied, enabling monitoring at a coarser spatial resolution characteristic of satellite imagery.

Chapter 2

State of the Art & Related Works

An extensive documentation activity was carried out regarding the geographical context under study and the environmental issues affecting the main water bodies of the provincial territory — the main river and the Mantua lakes. This involved reviewing the results of analyzes conducted by local agencies, consulting the scientific literature, contacting domain experts and well-established manufacturers of environmental analysis instruments, and attending conferences and trade fairs in the sector.

Both the state of the art and discussions with colleagues proved essential and indispensable for developing awareness and understanding of the topic, as well as the tools available to study these issues and design a pragmatic and sustainable research plan. The following tables report the bibliographic references of the papers found useful in the documentation phase. Table 2.1 lists papers that have raised awareness of the pressure exerted by agricultural and livestock activities on the environment and have provided a strong motivational push to direct research on this topic. The articles in Table 2.2 have allowed us to acquire knowledge of traditional techniques for managing livestock waste and the pollution resulting from it in order to understand how

to properly design the management and monitoring solutions subsequently developed in this thesis. In particular, the references cite the EU Nitrates Directive and regional regulations, the limitations of current monitoring systems, and scientific evidence of the challenges of their enforcement, as well as current research gaps. Table 2.3 contains articles describing numerous solutions implemented using IoT technologies for agri-food production. Most of them concern the monitoring and assessment of land health, revealing an unforgivable lack of solutions for the intelligent management of livestock waste spreading activities. The value of the research presented here stems from its originality in addressing this limitation. Since the legislation does not provide for continuous operational monitoring, and the scientific literature acknowledges the monitoring problem, the first outcome of this thesis presents a concrete and innovative solution for the distribution of livestock manure, described in Section 3.3.2:

- a low-cost IoT-based real-time navigator with a WEB interface;
- that guides drivers to their intended spreading destination;
- which monitors the activities and tracks the routes of the tankers;
- and reports the quantity and location of effluent spreading;
- an embryo of a supervisor designed to optimize operations and reduce their impact on the territory.

The articles in Table 2.4 describe the indices used in remote sensing activities and reveal which ones are traditionally used to study water bodies and aquatic vegetation, the two subjects on which the second part of this research focuses, because they directly reflect the impacts derived from the activities of the agri-food industry. Table 2.5 lists articles that showcase

numerous examples of how fellow researchers have used satellite remote sensing techniques to observe water and vegetation. This was crucial in identifying a poorly explored area of research: the spatiotemporal variation of turbidity in a river. The second outcome of this thesis addresses this neglected topic by proposing an original solution that accurately derives turbidity based on real data, thanks to five innovations:

- it uses a graphical technique to precisely follow the profile of a river (Section 4.2.3);
- it returns the data at the desired resolution (Figure 4.15);
- it includes an innovative set of plots that display the results in 3D and analyze the most significant fluctuations in detail (Section 4.3.4);
- it applies a specially tailored workflow: "the pipeline" (Section 4.2);
- it expresses a set of specifically designed metrics (Section 4.3.2).

Figure 2.1: Innovations of the turbidity extraction algorithm

Table 2.1: Anthropogenic nutrients and impacts on aquatic ecosystems

Ref	Summary
[5]	Analysis of irrigation systems and wastewater inputs affecting turbidity and sedimentation processes in the Mincio River.
[15]	Long-term study showing how anthropogenic pressure and eutrophication modify the coverage and community composition of submerged aquatic vegetation.
[22]	Review of agricultural contaminants and their downstream impacts on aquatic ecosystems; turbidity is proposed as a key transport indicator.
[38]	Investigates the influence of harvesting and eutrophication on macrophyte proliferation in shallow lakes.
[63]	Study linking excessive floating vegetation growth to agro-industrial nutrient inputs within the Oglio River watershed.

Table 2.2: Agricultural management, livestock waste, local authority regulations and ineffective monitoring, resulting soil pollution.

Ref	Summary
[6]	Describes soils as natural treatment systems for swine wastewater and the importance of proper manure application planning.
[11]	Comprehensive overview of management, reuse, and disposal techniques for livestock biological waste.
[42]	Highlights industrial livestock production as a major source of nutrient and microbial pollution in aquatic ecosystems.
[45]	Examines long-term impacts of swine wastewater and mineral fertilizers on soil microbial communities.
[57]	Farmers are required to submit formal documentation such as nutrient management plans and manure application reports.
[56]	The competent authorities carry out subsequent checks through administrative checks and occasional on-site inspections.
[16]	Control mechanisms rely mainly on declared information and periodic checks, not continuous monitoring of field operations.
[39]	The need to identify manure spreading on bare soil through multispectral RS indices.
[77]	Large-scale spatial analysis of environmental benefits from fertilizer closure periods enforcing Nitrates Directive restrictions.
[65]	Investigates chemical alterations in soils fertilized with swine wastewater and nitrogen volatilization dynamics.
[78]	Discusses nitrogen from manure and fertilizers as both essential nutrients and potential sources of water contamination.
[81]	Practical guidelines for safe agricultural use of sewage sludge and risk mitigation practices.

Table 2.3: IoT technologies and sensors for environmental monitoring**Ref**

Summary	
[7]	Autonomous Surface Vessel equipped with IoT sensors for flexible water quality monitoring across lake surfaces.
[13]	IoT system for monitoring urban river water quality using federated learning and machine learning classifiers.
[18]	IoT and machine learning framework for flash-flood prediction with fault-tolerant communication design.
[21]	IoT framework for managing and recycling agricultural waste in smart farming systems.
[28]	IoT network measuring water parameters such as pH, conductivity, turbidity, and temperature in rivers.
[30]	Floating IoT monitoring system with GPS for real-time lake water quality assessment.
[32]	IoT-based system supporting smart agricultural water management through remote monitoring.
[43]	Smart agriculture platform using IoT sensors to monitor environmental conditions affecting crop growth.
[44]	Evaluation of wireless IoT sensors for environmental monitoring and real-time data acquisition.
[48]	Overview of IoT architectures, protocols, and applications across multiple domains including environmental monitoring.
[49]	IoT-based monitoring system for water level and rainfall to support flood prevention in drainage systems.

Continued on next page

Ref	Summary
[52]	Wireless sensor network using ultrasonic sensors for continuous water level monitoring in flood-prone rivers.
[53]	Review of disaster management systems based on Wireless Sensor Networks and environmental sensing technologies.
[58]	IoT sensor system designed to monitor wastewater from agricultural and livestock activities.
[60]	Environmental monitoring system for smart cities using distributed IoT sensors.
[61]	Real-time monitoring of physicochemical parameters in the Ganges River using smart IoT sensors and big data analytics.

Table 2.4: Remote sensing and spectral indices (methods and review)

Ref	Summary
[66]	Evaluation of vegetation-index curve fitting models for accurate classification of salt marsh vegetation.
[74]	Comparison of NDWI, NDVI, and MNDWI indices for water body detection in satellite imagery.
[83]	Review of major vegetation indices used in remote sensing and their applications.
[84]	Study evaluating the suitability of different multisource remote sensing indices for product generation.
[85]	Development of an enhanced mangrove vegetation index (EMVI) using hyperspectral imagery.
[86]	Technical review on the use of deep learning for processing and analyzing remote sensing big data.

Table 2.5: Remote sensing applications for aquatic vegetation, turbidity, and water quality

Ref	Summary
[1]	Satellite-based turbidity analysis of a heavily impacted river using Sentinel imagery and GIS visualization.
[4]	Remote sensing approach to evaluate water quality and land cover change in the Lake Titicaca basin.
[8]	Seasonal turbidity classification in a reservoir using the NDTI spectral index.
[10]	Analysis of recent expansion of aquatic vegetation in Chinese lakes using satellite time series.
[19]	Sentinel-2 indices applied to detect duckweed infestations in small river systems.
[27]	Long-term study linking aquatic vegetation dynamics with fertilizer use and climate variability.
[34]	Spatiotemporal analysis of turbidity in reservoirs using Sentinel-2 imagery and Google Earth Engine.
[40]	Combines spectral indices and machine learning to derive urban quality-of-life indicators.
[55]	Mapping aquatic vegetation and algal blooms in shallow lakes using Landsat data and decision tree models.
[67]	Analysis of NDVI, NDWI, and land surface temperature to assess vegetation decline and urban heat effects.
[75]	Monitoring of aquatic vegetation expansion in Lake Fimon using NDVI from Copernicus satellites.
[80]	Uses spectral indices and phenological features to classify emergent, floating, and submerged aquatic vegetation.

2.1 Livestock & Environmental Issues in Mantua's Waterways

The environmental criticalities of the Mantuan water bodies are certified by the report prepared by ARPA Lombardia [1], concerning the "Ecological State of the Lakes of Mantua", summarized in Figure 2.2, which presents the values of the "Biological Quality Elements" (EQB) and the "Trophic Level of the Lakes for Ecological Status" (LTLeco). The high levels of eutrophication that characterize Lake Superior have led to the definition of a specific action plan called the Water Protection and Use Program (PTUA), making it an area worthy of study. The opportunity to study this phenomenon and its origins is emerging, presumably linked to the quality of the water that the lake receives from its main outlet, the Mincio River.

This intuition was confirmed and strengthened by data reported in a very detailed study that extended the analysis to the river basin, which was carried out recently in 2022. This concerning report was presented during the conference "Valli del Mincio – Delicato Equilibrio" held in Mantua in December 2022. Some of its findings are shown in Figure 2.3. Excessive fertilization in the municipalities crossed by the Mincio River is precisely documented in Figure 2.3c. The impact on the territory is severe and undeniable; the countryside is fully exploited, and the waters in the irrigation canals are very dense. Examples are shown in Figure 2.3a and 2.3b.

One trend highlighted in the report concerns the nature of the aquatic plant species found in the riverbed. A shift in prevalence from submerged to floating species at the surface has been observed, as shown in Figure 2.4.

[1] Stato delle acque superficiali in Lombardia - LAGHI DI MANTOVA - 2014-2019: `https://www.arpalombardia.it/media/rzdhhxjj/rapporto_2014_2019_mantova.pdf`

Mantua Lake	Three-year period	EQB status	LTLeco status	Status of supporting chemical elements	Ecological status	Elements that determine the classification
Superiore	2009-2011	poor	fair	high	POOR	phytoplankton
	2012-2014	poor	fair	good	POOR	macrophytes
	2014-2016	poor	fair	good	POOR	macrophytes
	2017-2019	fair	fair	fair	FAIR	phytoplankton, LTLeco, chemicals support
di mezzo	2009-2011	poor	fair	high	POOR	phytoplankton
	2012-2014	poor	fair	good	POOR	macrophytes
	2014-2016	poor	fair	good	POOR	macrophytes
	2017-2019	poor	fair	fair	POOR	macrophytes
Inferiore	2009-2011	poor	fair	high	POOR	phytoplankton
	2012-2014	fair	fair	good	FAIR	Macrophytes, LTLeco
	2014-2016	fair	fair	good	FAIR	Macrophytes, LTLeco
	2017-2019	poor	good	good	POOR	Fauna Fish

(a) Status of quality elements and ecological status for the four three-year monitoring periods.

Mantua Lake	Ecological objective	2009-2014 ecological status	2014-2019 ecological status
Superiore	Good by 2027	BAD	FAIR
di mezzo	Good by 2027	FAIR	POOR
Inferiore	Good by 2027	FAIR	POOR

(b) Lakes of Mantua: ecological objective and ecological status 2009-2014 (Programma di Tutela e Uso delle Acque - PTUA 2016); ecological status 2014-2019.

Figure 2.2: State of the lake and river waters, as reported by the local authorities.

(a) The countryside has been extensively exploited. Irrigation drains nutrients.

(b) Agricultural intensification has also led to a significant artificialization of the landscape.

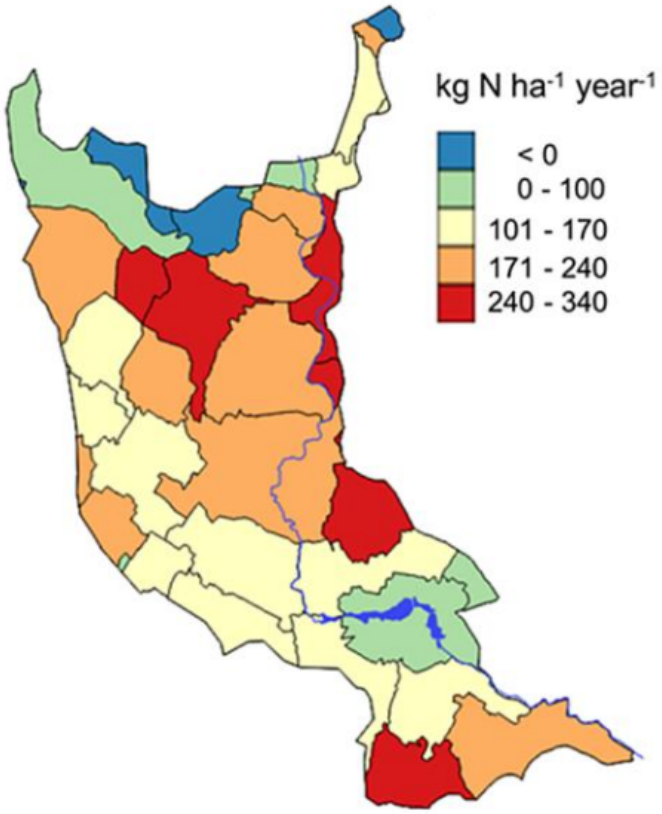

(c) Nitrate overload discharged into the municipalities of the Mincio basin.

Figure 2.3: Country exploitation.

(a) The abundant presence of nutrient-rich suspended solid particles has favored the development of floating aquatic vegetation to the detriment of submerged species.

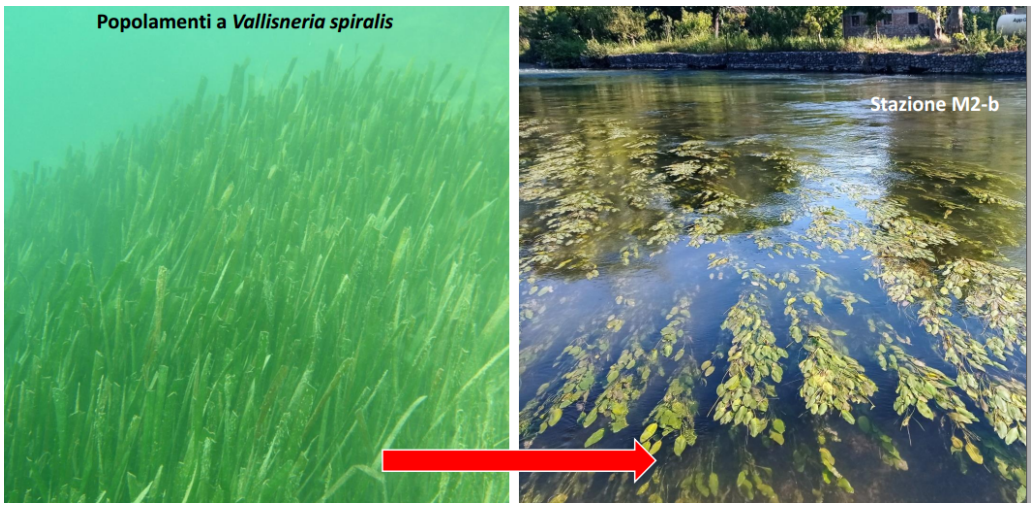

(b) a comparison between species in the two categories. Only the former produce oxygen available for aquatic fauna.

Figure 2.4: A shift in dominance has been observed in the last decade.

This is serious because it reduces photosynthetic production in the water, depriving aquatic fauna of oxygen. Additionally, the team in [15] studied how anthropogenic pressure changed the coverage and community composition of submerged aquatic vegetation in eutrophic lakes. Their findings are reported in Figure 2.5. [80, 38] presents other studies that analyze the presence of aquatic vegetation in lakes, considering plant development and classifying species into categories, namely emergent aquatic vegetation (EAV), floating leaf aquatic vegetation (FAV), and submerged aquatic vegetation (SAV). The former research computes the Enhanced Aquatic Vegetation Index (EAVI) for the year 2018, as shown in Figure 2.6. The latter study plots the phenological curves of the species over one year of observations in Figure 2.7, exploiting the Floating-leaved Vegetation Sensitive Index (FVSI) and Submerged Vegetation Sensitive Index (SVSI).

Substances transported through water are crucial for influencing vegetation and, consequently, animal species. When it comes to contaminants, whether biological or chemical in origin, they can have significant downstream impacts, as well described in [22], along with the resulting hazards and risks of altering biotic integrity and ecosystem function. Turbidity is an ideal indicator for studying the transport of substances in water, specifically those that move from a source zone (for example, a cultivated area) to a sink zone (often a lake, where the water flow slows down), through a transfer zone (a watercourse), as illustrated in figure 2.8 and again explained in the aforementioned study [22]. The Mincio River collects the waters of many drainage canals, which carry with them some of the substances distributed through chemical fertilization and fertigation of pig origin, as mentioned in the introduction. When a turbid canal, such as the Goldone, flows into the Mincio, the mixing effect of its water is visible to the naked eye, as shown in the photos in figures 2.9

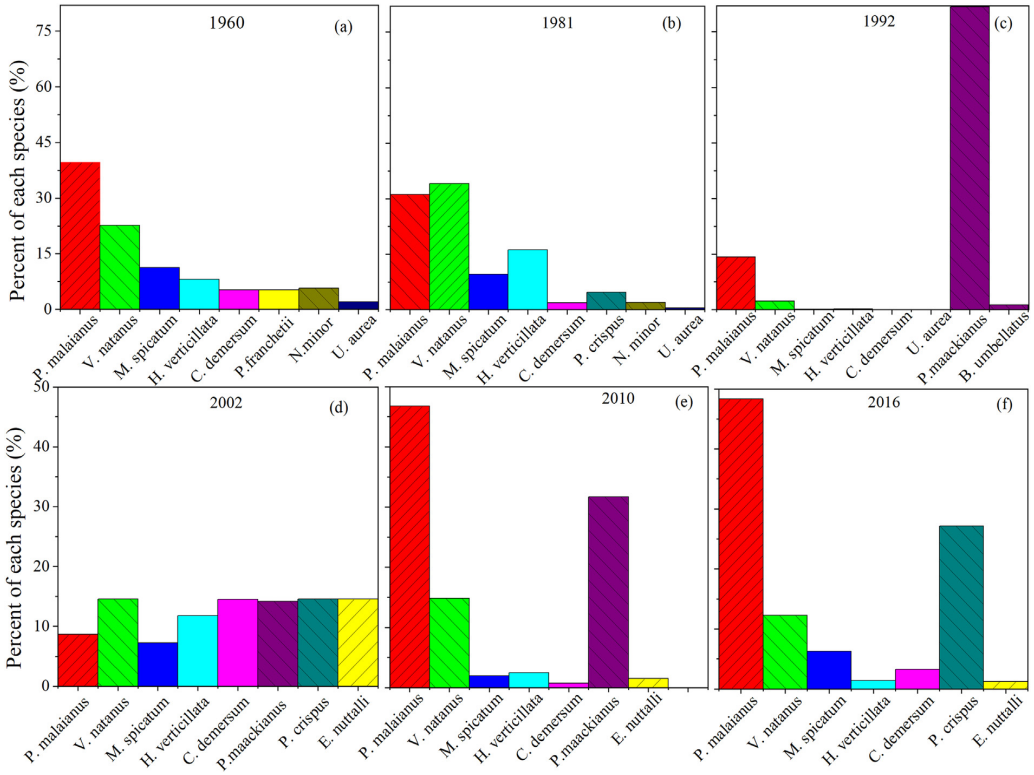

Figure 2.5: The main species composition of Submerged Aquatic Vegetation (SAV) in Lake Taihu (China) for the years 1960, 1981, 1992, 2002, 2010 and 2016. The species included Potamogeton malaianus, Vallisneria natans, Myriophyllum spicatum, Hydrilla verticillata, Ceratophyllum demersum, Najas minor, Utricularia aurea, Potamogeton maackianus, Potamogeton crispus, Elodea nuttallii and Potamogeton franchetti. (Source [15])

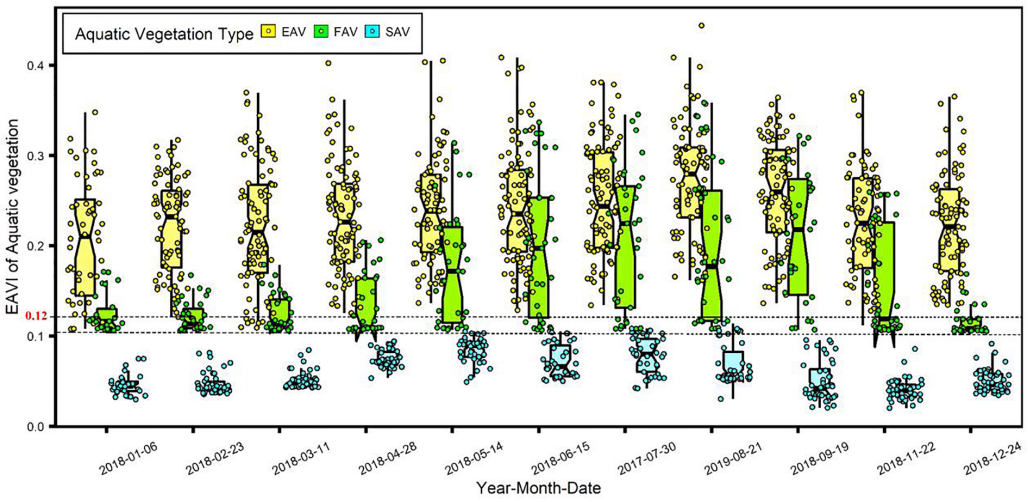

Figure 2.6: Enhanced Aquatic Vegetation Index (EAVI) values for Aquatic Vegetation categories (EAV, FAV, and SAV) in different months in Lake Taihu (China). (Source [80])

and 2.10. This circumstance prompted us to direct the third research topic toward an automated monitoring system for assessing turbidity in the river. To complement traditional sampling, which is indeed very demanding, as mentioned in the introduction.

Experts from local institutions and researchers who authored some of the cited studies have made themselves available to share their experiences. In meetings with them, they reported the considerable effort required to carry out measurements in the traditional manner. A need emerged for a system capable of overcoming these challenges — an innovative solution for the punctual and widespread detection and monitoring of the classic physical parameters indicative of the health of eutrophic watercourses in the Mantua area. An automated system with high autonomy and limited maintenance aims to reduce or eliminate manual measurements that require operators to reach sampling locations, which are often difficult to access. The domain

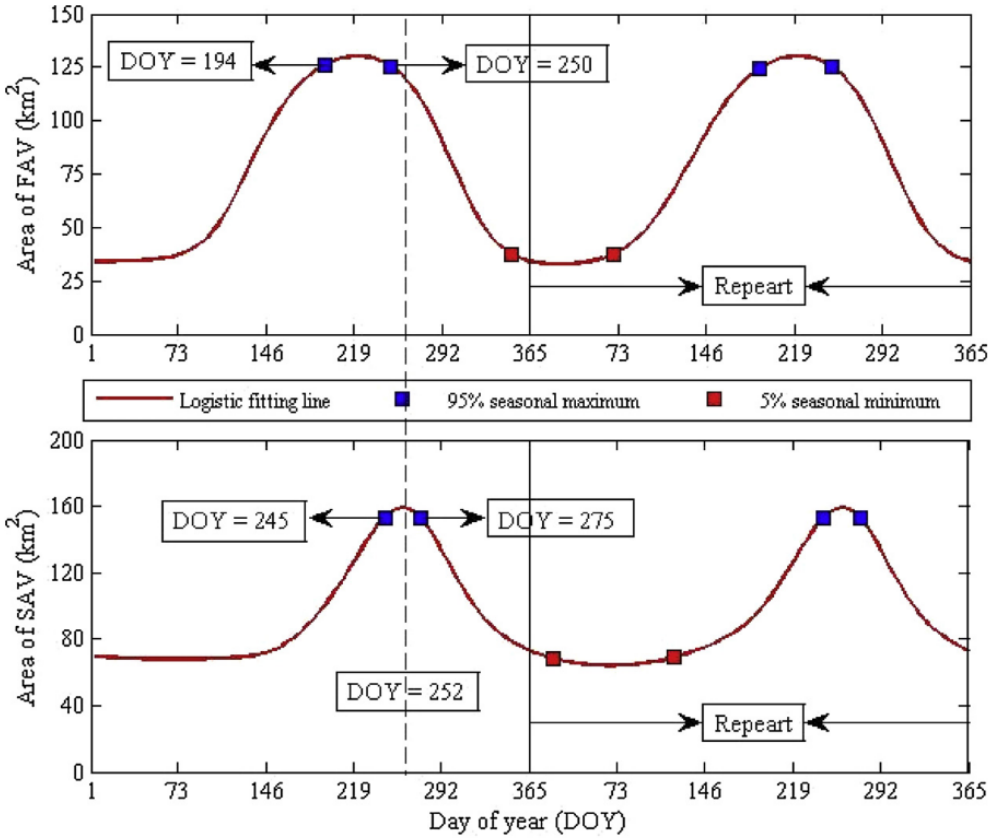

Figure 2.7: Phenological curves of Floating-leaved Aquatic Vegetation (FAV) and Submerged Aquatic Vegetation (SAV). Black dashed line represents the reference date (DOY = 252, late summer) when the aquatic vegetation (FAV + SAV) reaches a maximum area (Source [38]). Authors have explored spectral indices to map aquatic vegetation in Taihu Lake, China, such as the Floating-leaved Vegetation Sensitive Index (FVSI) and Submerged Vegetation Sensitive Index (SVSI).

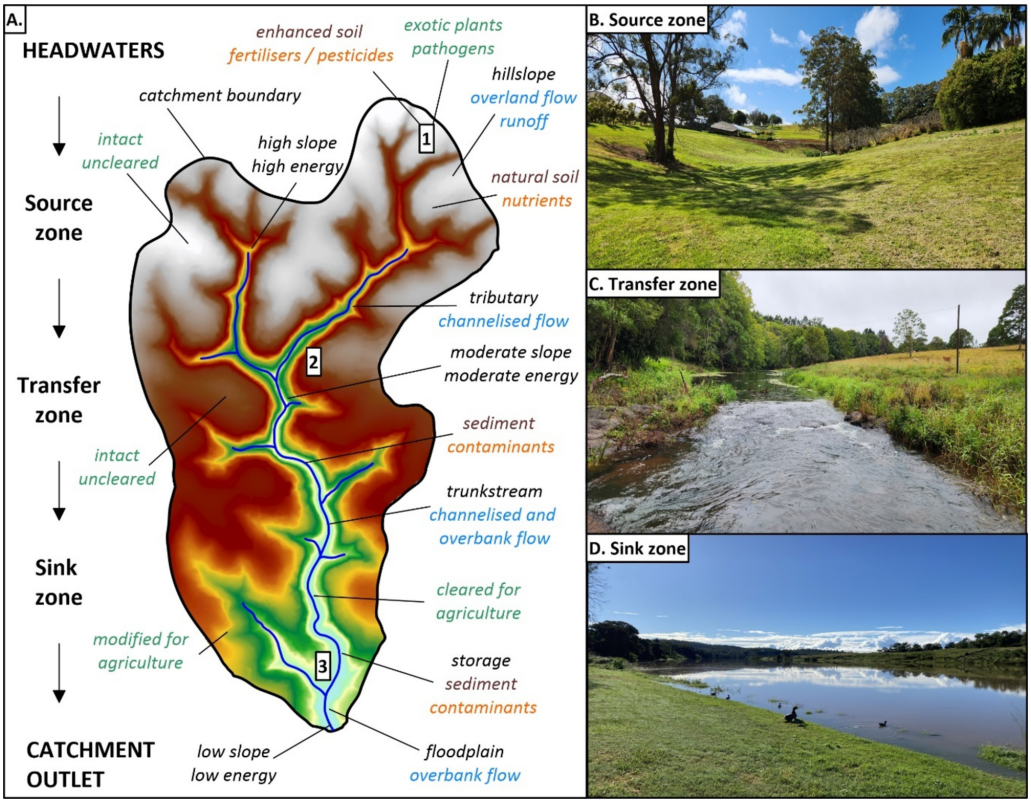

Figure 2.8: Schematic of (A) catchment location, characteristics and processes and how they may influence the transfer of contaminants. For example (B) a farm located near the catchment divide (source zone) is only exposed to rainfall, and generates run-off; (C) a farm located in the middle part of the catchment (transfer zone) is exposed to run-on from hillslopes, and rainfall and generates run-off into tributaries; and (D) a farm located towards the bottom of the catchment (sink zone) is exposed to run-on from hillslopes, flood waters from the river, and rainfall and generates run-off into the river. Colours represent physical features (black), soil/sediment processes (brown), water processes (blue), contaminant/nutrient processes (orange), and vegetation processes (green). (Source [22])

(a) Goldone canal, highly turbid.

(b) Rio Bisavola, highly turbid.

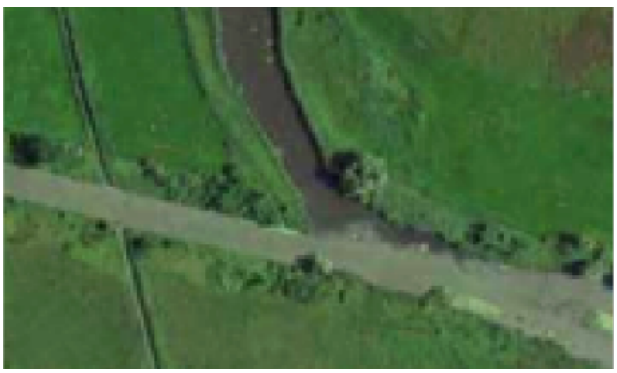

(c) A minor canal. Less turbid then the Mincio itself.

Figure 2.9: Several turbid canals flow into the Mincio. High levels of turbidity manifest themselves in lighter colored waters, so much so that their wake is visible in the receiving river.

Figure 2.10: Turbidity changes caused by the injection of the Goldone canal into the Mincio: before and after situations. (Source [5])

experts identified and recommended focusing on six aquatic variables that are worthwhile to measure: turbidity, chlorophyll, pH, dissolved oxygen, water temperature, and electrical conductivity.

2.2 IoT-based Field Sensing for Monitoring Surface Water Bodies

To follow the indications received from domain experts, a feasibility study was initiated for an environmental monitoring network to sample these parameters, covering the surface of Lake Superior up to the locality of Grazie, located seven kilometers upstream. The research began with a state-of-the-art assessment of this field. The Internet of Things (IoT) technology immediately seemed like an excellent choice to consider in addressing this challenge. From a technological point of view, the Internet of Things has revolutionized environmental monitoring by providing real-time data collection and analysis capabilities, leveraging robust wireless connectivity, a technology with high potential [44]. An IoT overview [48] illustrates the basic structure of a monitoring IoT network in Figure 2.11, reaffirming that it is "an umbrella covering many protocols, technologies, and concepts," providing "high scalability and interoperability features" and allowing applications in various domains such as agriculture, industry, and the military, while offering an easy integration path for sensors and small devices.

Another overview of IoT [53] focuses on disaster management systems that utilize Wireless Sensor Networks (WSNs). It describes the WSN architecture, its operation, the types of disasters, and the sensors used to assess their severity. A literature review is provided, explaining the problems, technologies, and protocols used, along with their solutions. IoT technology has already

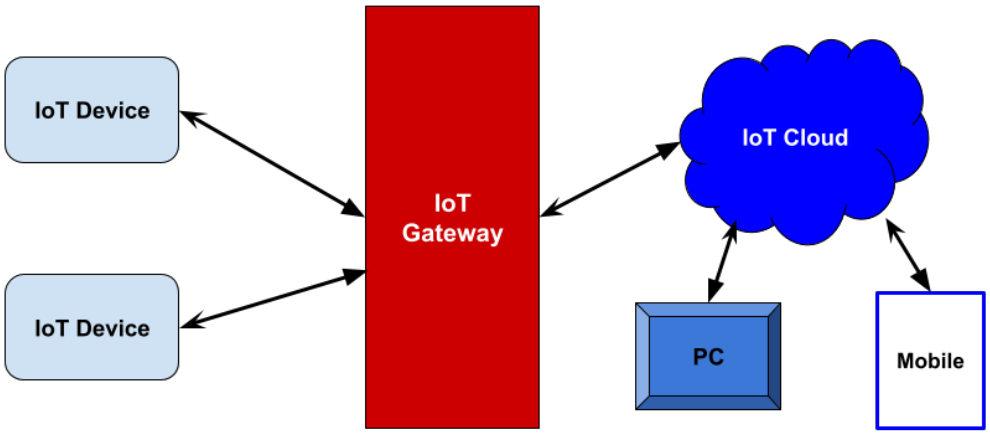

Figure 2.11: The basic structure of an IoT system (Source [48]).

been used for research in a specific aquatic field, such as in [13], where it has been possible to effectively evaluate the suitability of a river for human bathing as it flows through a large city, using machine learning classifiers. Study [61] is also an interesting use case; a large set of physical and chemical parameters is sampled with IoT smart sensors (collectively referred to as IoT gadgets but not further defined) in the waters of the Indian Ganga River, which suffers from pollution caused by the extensive use of fertilizers in agriculture that affects human health and river biota, to determine the Water Quality Index (WQI). [49] is another example of a Wireless Sensor Network that allows real-time monitoring of water levels and rainfall to facilitate the management of locks in residential areas, schools, and hospitals, thereby preventing flooding and unpleasant odors in open ditches during heavy rains, high tides, and pollution. The WSN developed in [52] was designed to use an ultrasonic sensor for continuous water level detection in flood-prone river areas in Indonesia. This example reiterates the advantages of IoT technologies: low power consumption, simple structure, low cost, and convenient installation. The studio [18] also uses an IoT-based WSN for data collection and machine

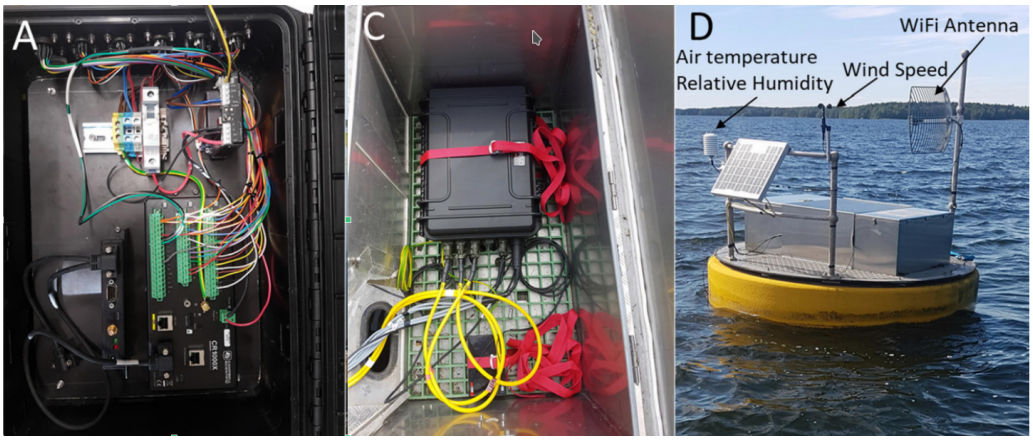

Figure 2.12: The highly modular components of the Smart Lagoon mission.

learning techniques to predict flash floods caused by rivers in the São Carlos area of Brazil. It is designed to ensure fault tolerance by anticipating the risks of communication disruptions and node destruction during disasters. It works by adding intelligence to the nodes to perform data distribution and forecasts, even in extreme situations. The authors of [28] also use IoT sensors in a wireless network to observe real-time pH, conductivity, turbidity, temperature, and water flow to predict future critical events, including impending floods in rivers in Bangladesh. [30] is another study that implements an intelligent, effective, accurate, real-time, reliable, and scalable water quality monitoring system in several Indian lakes. It is unique because, in addition to sensors for total dissolved solids (TDS), pH, turbidity, and temperature, the floating device includes a GPS module, demonstrating that these systems can provide georeferenced data. This feature will be useful in developing the second topic of my research.

IoT technologies, given the characteristics that emerged from the state-of-the-art study, appear promising for the case study in question due to their undeniable advantages: flexibility in integrating various types of sensors, high

wireless communication capabilities, the freedom to position measurement stations in an easily scalable number, small-sized, low-power hardware, and the existence of a mature ecosystem of manufacturers, libraries, and standard protocols for control software development.

Continuing the exploratory phase of the investigation, it was observed that a limited continuous monitoring network had already been deployed by the Parco del Mincio. This system, composed of four multiparametric stations positioned along the shores of the three lakes, was designed to measure chlorophyll and dissolved oxygen concentrations, as documented by local media sources[2], with the objective of assessing the risk of anoxic events that could threaten aquatic fauna. Implementing such a monitoring solution requires addressing significant challenges, primarily counteracting biofouling processes, which in this case quickly compromised the operational reliability and functionality of the probes. Aquatic environments are unexpectedly hostile, hosting numerous living species that quickly colonize the sensors and accumulate on them. This constitutes a real attack that renders measurements unreliable in a short amount of time. In addition, the water itself leaves residues and exhibits annual thermal variations that disturb the equipment. The sensors, therefore, require periodic calibration operations, which unsustainably increase operating costs and should be minimized. Not to mention the risks of vandalism, theft, and accidental damage faced by these sampling stations, which remain unattended for long periods in unmonitored locations. To address these problems, several countermeasures were conceived, drawing inspiration from the similar "Smart Lagoon" project (details are

[2]Gazzetta di Mantova (2018 - Studio europeo sul Mincio. Il Parco userà boe hi-tech): https://www.gazzettadimantova.it/territorio-mantovano/studio-europeo-sul-mincio-il-parco-usera-boe-hi-tech-1.11904465

(a) AtlasScientific EZO TRD Temperature kit.

(b) AtlasScientific EZO PH kit.

Figure 2.13: Some toy sensors found in the market survey. Very cheap but clearly inadequate for the specifications of the research work to be realized.

depicted in Figure 2.12), which is already operational in a Spanish lagoon and has been reported as successful by its developers.

To evaluate the adoption of suitable sensors for the project at stake, a market survey was conducted. The range of devices is highly varied, starting from models that are little more than educational — practically toys or Do-It-Yourself (DIY) devices — costing only tens of euros, such as those reported in Figure 2.13. For this case study, however, more sophisticated models were sought that were equipped with effective cleaning systems and required minimal maintenance.

These suitable models proved to be very expensive, such as the sensors in figures 2.14b and 2.14c. Subsequently, possible methods to prevent or reduce the need for cleaning were explored. One possible solution could be to keep the sensor package protected from water and immerse it only at the moment of measurement. However, such a movement system would

(a) Libelium ONE.

(b) YSI EXO2 7 ports Multiparameter Sonde.

(c) Seabird Scientific Inc.'s ECO FLNTU Dual Channel Fluorometer.

Figure 2.14: Professional sensors being evaluated for use in monitoring stations. Note the cleaning device, a rotating copper "wiper", in two models, which are quite expensive (about 20 k$ each).

Figure 2.15: Map of the path followed by a floating drone during a monitoring mission (Source [7]).

have been complex, and its power supply would have significantly increased energy consumption — a critical factor for off-grid stations like these. A final hypothesis was to avoid fixed stations altogether, replacing them with a sampling drone — a semi-autonomous, self-commanded watercraft hosting the sensor package that performs monitoring missions on demand and visits the locations to be monitored daily. A drone of this category is shown in figure 2.16. Another Autonomous Surface Vessel (ASV) is used in [7] to undertake a Water Quality Monitoring study based on a set of IoT based sensors similar to those reviewed in figure 2.14. Exploiting a floating drone would entail the loss of continuous measurements but offer valuable flexibility of movement across the entire lake surface, allowing significant freedom in planning routes. One example is shown in Figure 2.15. Alternatively, the use of a towing drone was hypothesized to retrieve and tow the monitoring stations as needed from the sampling points to the collection center, where operators could easily perform maintenance and replacement operations, thus

Figure 2.16: Details of a semi-autonomous floating drone, to be adapted for monitoring missions.

reducing costs.

The possibility of using the most sophisticated sensors determined the success of the aforementioned Smart Lagoon project, which was made possible by very substantial funding. For my research, the implementation of the environmental monitoring network using IoT technology was postponed until conditions became favorable and made it feasible.

At the end of this study, it is clear that by using IoT technologies and equipment, dedicated tools and solutions can be developed to effectively and economically manage and monitor activities and processes occurring in the territory, including investigating and reducing the impact of agricultural and livestock production on the Po Valley, which is the main focus of this research. As previously mentioned, eutrophication and hypoxia resulting from high nitrogen levels threaten biodiversity and the health of aquatic ecosystems, and

their effects periodically manifest in the Mantua area. This excess of nutrients present in the water bodies is a side effect of unfair practices carried out by the agricultural and livestock industries, with regulatory authorities failing to adequately monitor them. The aforementioned European Union regulation, set out in the document [36] in the area analyzed in this research, aims to regulate the disposal of these substances, recognizing their status as waste due to their hazardous nature and, therefore, requiring their distribution over large areas designated in proportion to the number of animals raised — a difficult requirement for large, intensive farms. However, gaps exist in the enforcement of these regulations, leading to cases of non-compliance and environmental risks resulting from inappropriate manure spills. At the regional level, compliance is generally ensured through administrative procedures requiring farmers to submit formal documentation such as nutrient management plans and manure application reports [57]. In the Italian context, for example, farmers must provide information through the so-called "Nitrates Communication" and related agronomic plans, which are subsequently verified by the competent authorities through administrative checks and occasional on-site inspections [56]. However, these control mechanisms are largely based on declared information and periodic verification rather than continuous monitoring of field operations [16]. Consequently, the actual spatial and temporal execution of manure spreading activities is rarely tracked in real time at the operational level.

From a scientific and technical perspective, the monitoring of manure spreading practices remains a complex task. The large spatial extent of agricultural areas and the episodic nature of spreading operations make it difficult for authorities to systematically observe all fields where manure application may occur. Previous studies have highlighted that verifying compliance

with fertilization restrictions is inherently challenging because monitoring every agricultural plot across large territories is practically infeasible [77]. For this reason, several research efforts have explored alternative monitoring approaches based on remote sensing and geospatial analysis to detect manure application events [39] and support environmental compliance assessment. The increasing interest in satellite-based detection and spatial analysis methods reflects the current lack of operational tools capable of continuously tracking manure spreading activities at field scale.

What is missing is a monitoring tool that provides accurate and timely information about the activities carried out to manage livestock waste. Such information would be crucial for both the companies themselves and for environmental protection agencies. To address these challenges, research could develop a comprehensive software solution designed to facilitate the real-time monitoring and management of manure distribution operations associated with intensive livestock farming. The system could rely on basic mobile technologies to ensure regulatory compliance without requiring dedicated hardware. The implementation would follow the Internet of Things (IoT) approach, as this technology is currently the primary enabler of building robust and cost-effective environmental monitoring solutions. The state of the art for IoT needs further investigation; it could provide additional insights in this direction.

In agriculture, IoT technologies are increasingly employed in precision farming — for effective soil monitoring, crop management, water management [32], and livestock tracking [44]. IoT sensors enable continuous monitoring of environmental parameters such as temperature, humidity, soil moisture, and air quality [43, 60]. These sensors provide farmers with valuable insights into the conditions affecting crop growth and livestock health, allowing for

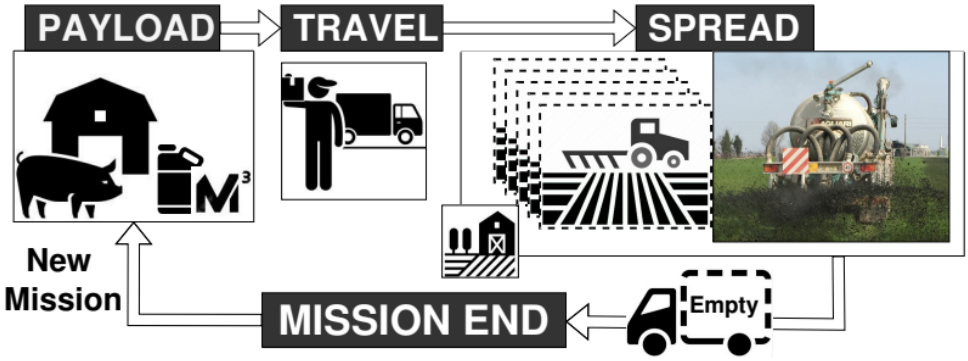

Figure 2.17: Schematic representation of the spreading procedure.

more precise and efficient management practices. In livestock management, IoT solutions have been deployed for tasks ranging from animal tracking and behavior monitoring to health management and waste control [21, 58]. Advanced tracking devices equipped with GPS and accelerometer sensors allow farmers to monitor the location and movement patterns of individual animals in real-time, facilitating efficient herd management and reducing the risk of loss. The integration of IoT technologies in livestock waste management is still under-explored, holding great promise for improving environmental sustainability and agricultural productivity. By leveraging real-time data collection and analysis capabilities, farmers can make more informed decisions and implement proactive measures to mitigate the impact of agricultural activities on the environment.

The research described in this thesis contributes to this field by studying how to develop tools and methodologies specifically adapted to the challenges of livestock waste management in the Po Valley region, where fertigation is widely used to dispose of swine manure. The figure 2.17 schematically shows the progress of a normal delivery mission, as hundreds of such missions take place in the Po Valley every day. The breeder assigns the transfer at the

pig farm, loading the effluent to be disposed of (the payload) onto a tanker truck. A driver then transports it to the field of a partner farmer to distribute it until the tank is emptied before proceeding to the next mission. This cycle is repeated daily according to a planned schedule. Optimizing livestock waste disposal activities is a complex and multifaceted objective that requires specific research into the state of the art. It is not enough to simply plan missions to reduce abnormal discharges, avoid regulatory violations, and lower journey and unloading times to decrease operating costs while respecting the agreements that breeders and farmers establish regarding designated areas and the times allocated for discharges. These are ordinary goals. Other objectives are equally important. The following sources were consulted to gain the knowledge necessary for developing an effective system for optimizing discharges. In [45], the researchers describe the environmental damage caused by the large quantities of slurry spread on the ground, which ultimately become pollutants that drain into the soil. The paper [42] contains data and examples of large farms and serious incidents of nitrate dispersion into the air and water that occurred in the USA in 2003, highlighting the regulatory limitations in force at that time. The editor of "Farmers Weekly" reports online [81] a long series of binding recommendations for operators in the United Kingdom who spread slurry to operate "risk-free" under the threat of sanctions. It highlights a matrix that matches the types of slurry to the crops for which they are most effective. It also includes tables showing the nutritional composition of the various types of slurry. The soil must be characterized through specific periodic tests conducted at a defined depth. Additionally, there are many other requirements to comply with regarding timing, odors, weather, prohibited areas, types of soil, and crops. The paper [6] reports the content of various types of slurry and wastewater, as well as a classification

of soil types into seven categories ranked from most to least suitable based on the risk of accidental dispersion of hazardous substances. The paper [65] reaches the same conclusions, providing examples of field experiments that involve inoculating wastewater samples at different concentrations and mixing them with chemical fertilizers. It validates the high volatility of nitrates, thus recommending coupling the spreading with crop growth. The paper [11] is a rich compendium on livestock wastewater and, in particular, illustrates in detail the numerous techniques for its management, use, and disposal. The final aim of the hypothesized "wastewater missions' optimizer" is to identify suitable discharge areas for maximum nitrogen absorption by crops, thereby achieving higher yields and lowering nutrient drainage while avoiding the dispersion of contaminants that would pollute the air, soil, and surface and groundwater.

2.3 Territorial Analysis via Remote Sensing Indices from Satellite

The third research topic shifts the point of observation far away in space; this is why this research methodology is called Remote Sensing (RS). The focus is on studying the evolution of some of the aforementioned environmental phenomena with the aid of an automated tool specifically designed and developed to analyze the vast repertoire of satellite images of the Mantua area from the past several decades, accessible via a dedicated platform, to extract the so-called remote sensing indices. These indices are numerous, as summarized in [83]. Table 2.6 reports the acronyms of the indices mentioned in this thesis and can be useful as a reference. The indices are useful for a wide range of environmental and monitoring applications, to the point of

meriting a specific search in the scientific literature to choose the most suitable ones for this study. For my research, three of the most popular indices have proven to be a good choice to accommodate two themes of research, which are introduced a little further on.

- The Normalized Difference Turbidity Index (NDTI) was selected to estimate the degree of river turbidity and its spatial and temporal variations. Transparency indirectly reflects the overall status of water quality; thus, significant reductions in transparency can serve as indicators of pollution events.

- The Normalized Difference Water Index (NDWI) was useful for identifying and monitoring the extent and depth of water bodies.

- The Normalized Difference Vegetation Index (NDVI) was processed to quantify vegetation presence, health status, and density—including, to some extent, aquatic vegetation.

According to the Scopus bibliographic database, these indices are among the most frequently used metrics in remote sensing research. By the end of 2025, NDVI is cited in approximately 40,000 publications, NDWI in more than 3,000, and both are co-cited in around 1,700 studies. Turbidity, by contrast, remains a comparatively less explored parameter. NDTI is a niche index, appearing in roughly 300 publications—about 60 in conjunction with NDVI, 30 with NDWI, and only 10 in which all three indices are discussed together.

The indices are obtained by processing images captured by numerous satellites crossing the planet, which have been launched into orbit over time by various missions implemented by different government agencies. The best-known and most cited missions in this research are the European Copernicus by ESA, the American Landsat by USGS, and the MODerate-resolution

Table 2.6: Remote Sensing indices mentioned or used in this thesis, related to vegetation or water or both

Name	Acronym	Reference
Normalized Difference Turbidity Index	NDTI	4.3.2
Normalized Difference Water Index	NDWI	4.3.2 [83]
Normalized Difference Vegetation Index	NDVI	4.3.2 [83]
Floating-leaved Vegetation Sensitive Index	FVSI	[38]
Submerged Vegetation Sensitive Index	SVSI	[38]
Enhanced Vegetation Index	EVI	[10, 80, 83]
Enhanced Aquatic Vegetation Index	EAVI	[80]
Automated Water Extraction Index	AWEI	[10]
Modified Normalized Difference Water Index	MNDWI	[10, 34, 74]
Green NDVI	GNDVI	[19, 66, 83]
Water Adjusted NDVI	WAVI	[66, 80]
Enhanced Mangrove Vegetation Index	EMVI	[85]
Soil Adjusted Vegetation Index	SAVI	[4, 80, 83]
Normalized Difference Aquatic Vegetation Index	NDAVI	[4, 19, 80]
Green Red Vegetation Index	GRVI	[19, 83]
Floating Algae Index	FAI	[80]
Macro Algae Index	MAI	[55, 80]
Mangrove Vegetation Index	MVI	[80]

Imaging Spectroradiometer (MODIS) by NASA. The images from these satellites have different technical characteristics and are collected in dedicated datasets accessible via dedicated platforms. To access the imagery, this research utilized the Google Earth Engine (GEE) platform.

The abundance of datasets and processing options made available to scholars by satellite platforms can be overwhelming for newcomers to this field, requiring careful attention, time, and a structured approach to master. Typically, the workflow for developing a Remote Sensing research project consists of four main phases: RS acquisition, RS processing, RS analysis, and RS application, as described in [86] and illustrated in Figure 2.18. For this research, an alternative pipeline has been conceived and implemented, tailored to the use cases of watercourses, which is explained in Chapter 4 and is based on 4 phases, namely Data Acquisition, Preprocessing, Feature Extraction, and Post-processing. The authors of [10] proposed a rather sophisticated preprocessing step for segmenting the area covered by lakes in China, as shown in Figure 2.19, involving numerous vegetation RS indices, namely AWEI (Automated Water Extraction Index), MNDWI (Modified Normalized Difference Water Index), EVI (Enhanced Vegetation Index), and the aforementioned NDVI. Another similar task is estimating the water spread area in tropical reservoirs, a study proposed in [34], whose workflow is illustrated in Figure 2.20. Another advanced implementation of the preprocessing step is illustrated in Figure 2.21, aimed at constructing a so called Pixel-Differential Time-Series for the classification of salt vegetation in marshes, where the authors of [10] identified and removed clouds, cloud shadows, and snow pixels for each image to minimize atmospheric effects. By removing only the noisy pixels instead of the entire images affected by clouds, the resulting observations allowed for a significant improvement in the RS

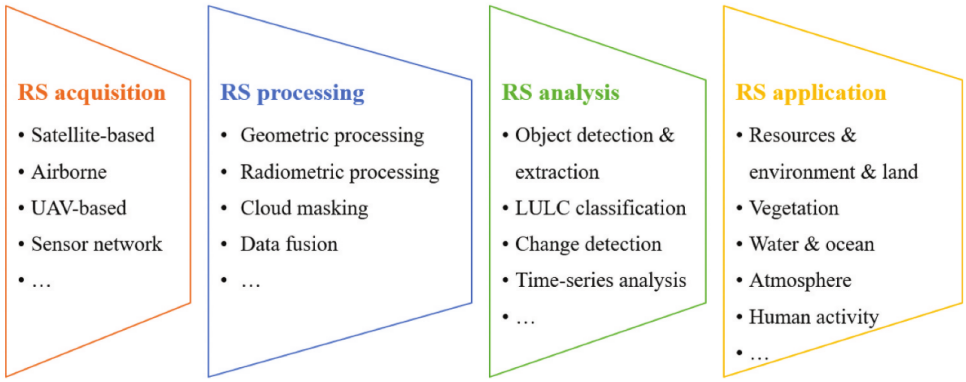

Figure 2.18: The general technical pipeline of processing and analysis for remote sensing big data (Source [86]).

Vegetation Index assessment.

The research described in this thesis follows two themes.

The first theme addressed was the impact of excessive quantities of fertilizers on aquatic vegetation, resulting from their runoff into the surface water network. Focusing in particular on the aforementioned abnormal growth of floating plants in Lake Superiore di Mantua, which, according to [63], is presumably linked to agro-industrial practices such as fertigation with manure and sludge. The challenge of this research was monitoring the evolution of the green carpet over the last seven years. An original technique was designed and implemented to segment the lake into two areas, covered respectively by vegetation and water. Some papers served as inspiration for determining the Green Island profile by finely calibrating observations obtained from the NDWI and NDVI differential indices derived from representative satellite images taken over various months. Indeed, several studies have applied these specific RS indices in real use cases and have provided useful insights into assessing their suitability under given conditions, such as in [84]. To obtain similar outcomes, additional indices derived from NDVI (Green GNDVI and

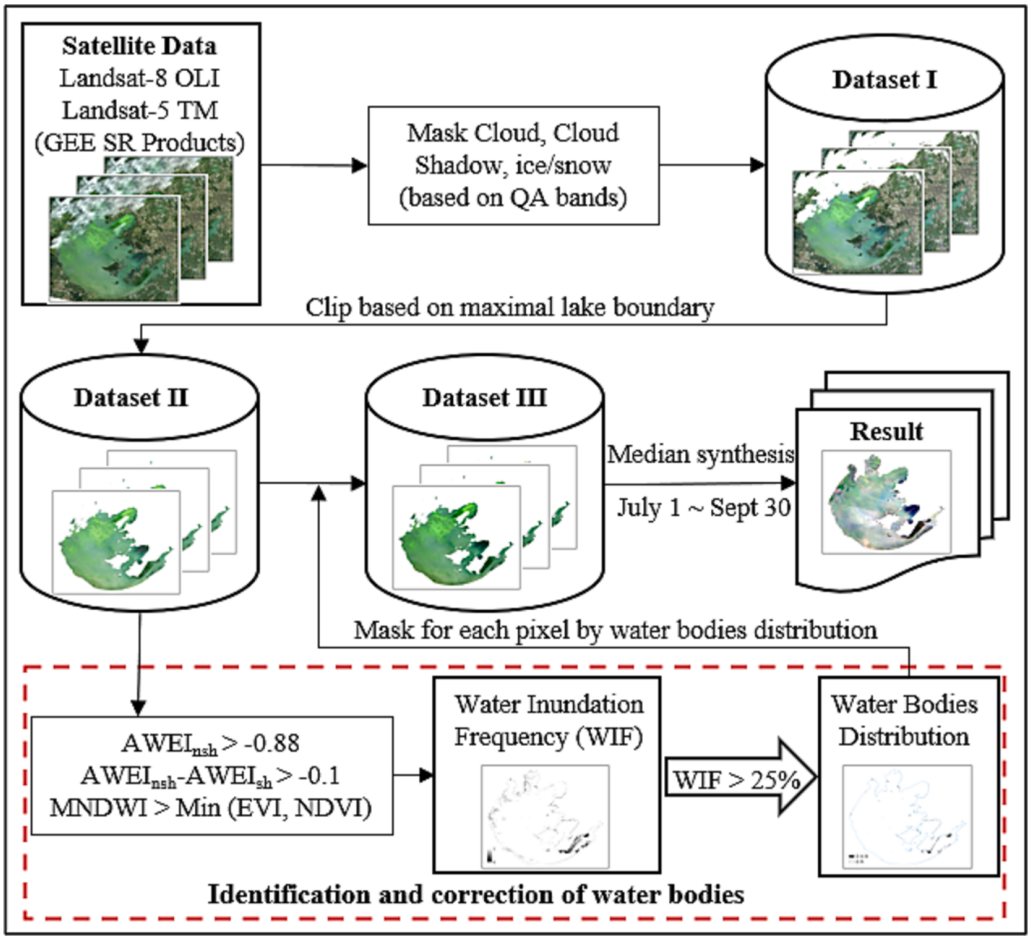

Figure 2.19: Flowchart of satellite images pre-processing based on the platform of Google Earth Engine. The picture takes Lake Taihu as an example to show how to obtain the data of one year. (Source [10]). GEE stands for Google Earth Engine, the same RS platform employed for this thesis analysis.

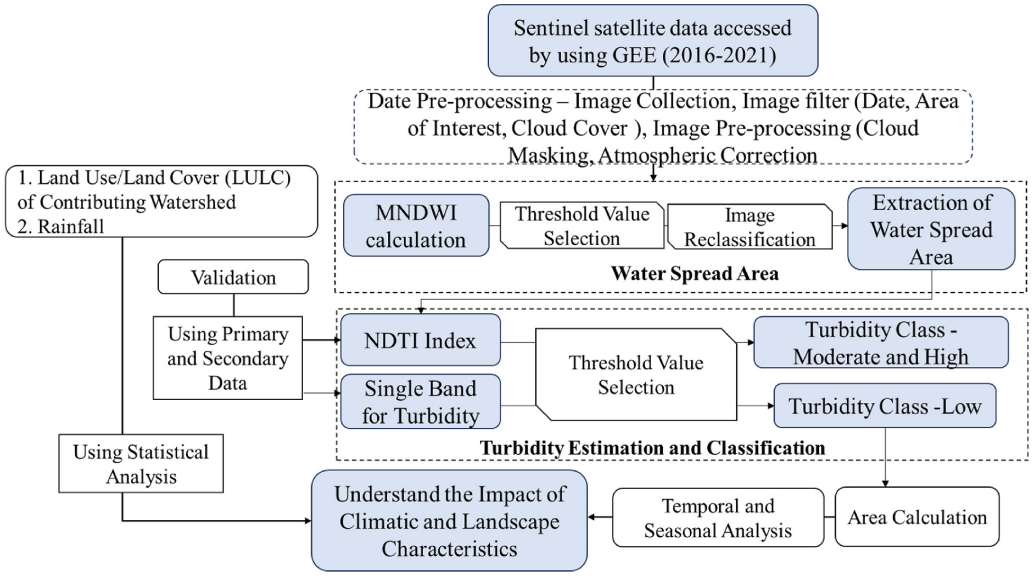

Figure 2.20: Workflow for estimating water spread area, using the Modified Normalized Difference Water Index (MNDWI), and turbidity zones using integration of single red band reflectance with NDTI derived from Sentinel-2 data in tropical reservoirs and assessment of catchment-related factors (Source [34]).

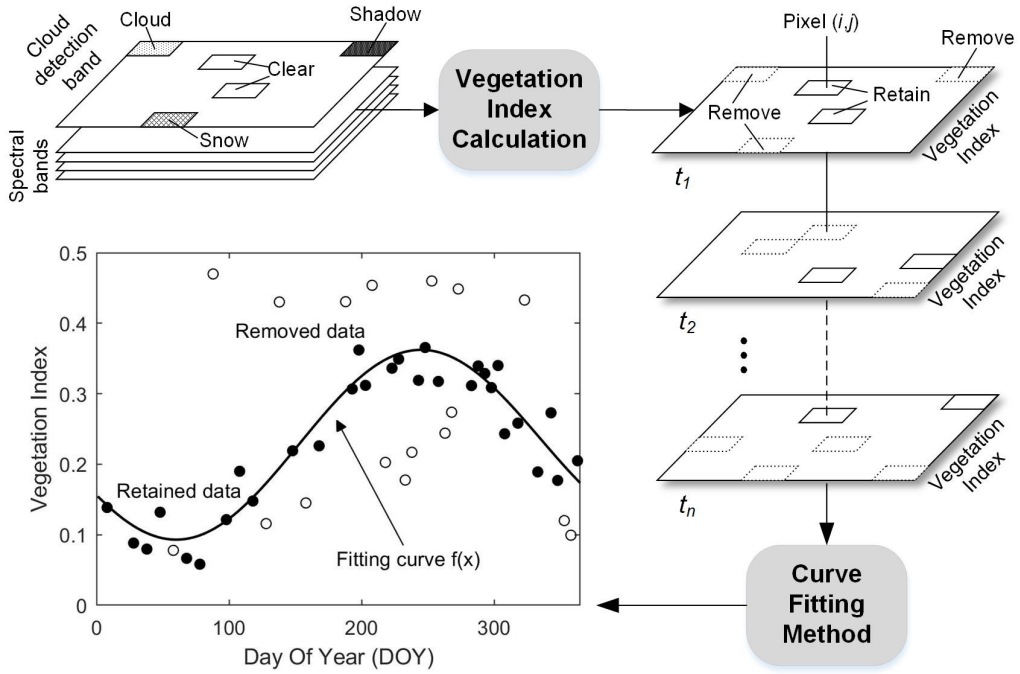

Figure 2.21: Summary of pre-processing methods used in the construction and application of pixel-differential time series analyses. (Source [10]).

Water Adjusted WAVI) have been used to detect salt marsh vegetation in [66] and [85] (Enhanced Mangrove EMVI) for mapping mangrove areas. Others have been obtained from NDWI. In [74], the authors employ the Modified Normalized Difference Water Index (MNDWI), which minimizes signal interference from built-up areas, making it superior for "Water Body Detection" studies in urban contexts.

The second topic developed using Remote Sensing technology investigates the turbidity behavior of the river that feeds the aforementioned lakes of Mantua. This is because the waters of the Mincio river are not clear, as they are contaminated by urban wastewater from the large population living in that province. Additionally, they receive effluents derived from high-impact industrial and agricultural activities. Despite being a key indicator of water quality and suspended solids content, river transparency remains a relatively unexplored aspect of this phenomenon, given the commitment required for its in-depth evaluation. Traditional in situ monitoring techniques require the work of a team of operators to cover the entire length of a long river for a significant period. So much so that LabTer Crea [3], an organization that deals with environmental research, has conceived an original way to address this objective difficulty. Since 1990, it has commissioned classes from local schools to carry out annual monitoring along the course of the Mincio.

The evident relevance of these data, along with the environmental insights they can provide and the difficulty of obtaining them, has stimulated this study. The challenge was to develop an automated, open-source tool that could be used at nearly zero cost to assess the turbidity values of the water in the river. This was made possible because of recent advances in remote

[3]Laboratorio Territoriale - Centro di Riferimento per l'Educazione Ambientale.: `https://www.labtercrea.it/`

sensing. Over time, assessments of water quality and turbidity dynamics in fluvial and lacustrine environments have become increasingly refined.

Numerous studies reviewed during the work—consistent with the research presented here—have applied comparative analyzes based on classical vegetation and water body RS indices while exploring distinct methodological frameworks for both lake and river use cases.

For instance, the author of [75] aims to quantify the presence of vegetation that periodically invades a lake in northern Italy, near Fimon (VI). He chose to rely exclusively on the NDVI index derived from Copernicus satellites and to overcome cloud cover disturbances by temporally aggregating only cloud-free observations. He reports obtaining at least five clean images per month, thus ensuring adequate data quality over the four years analyzed, with only two particularly cloudy months excluded. The GEE API was used to calculate the hectares covered by vegetation and to plot them monthly.

In [55], the authors describe the environmental criticalities that lakes in China suffer from and distinguish areas colonized by aquatic vegetation from areas inhabited by algae, open water, or land, using three spectral indices, namely the ubiquitous NDVI, the Emergent Vegetation Spectral Index (EVSI), and the proposed Macroalgae Index (MAI), correlating them with water temperature over the last three decades. The decision tree model they employ is reported in Figure 2.22.

The authors of [80] applied nine indices: Enhanced Aquatic Vegetation Index (EAVI), Soil Adjusted Vegetation Index (SAVI), NDVI, Floating Algae Index (FAI), Enhanced Vegetation Index (EVI), Macro Algae Index (MAI), Water Adjusted NDVI (WAVI), Normalized Difference Aquatic Vegetation Index (NDAVI), and Mangrove Vegetation Index (MVI) to evaluate the ability to distinguish between three categories of aquatic vegetation, depending on

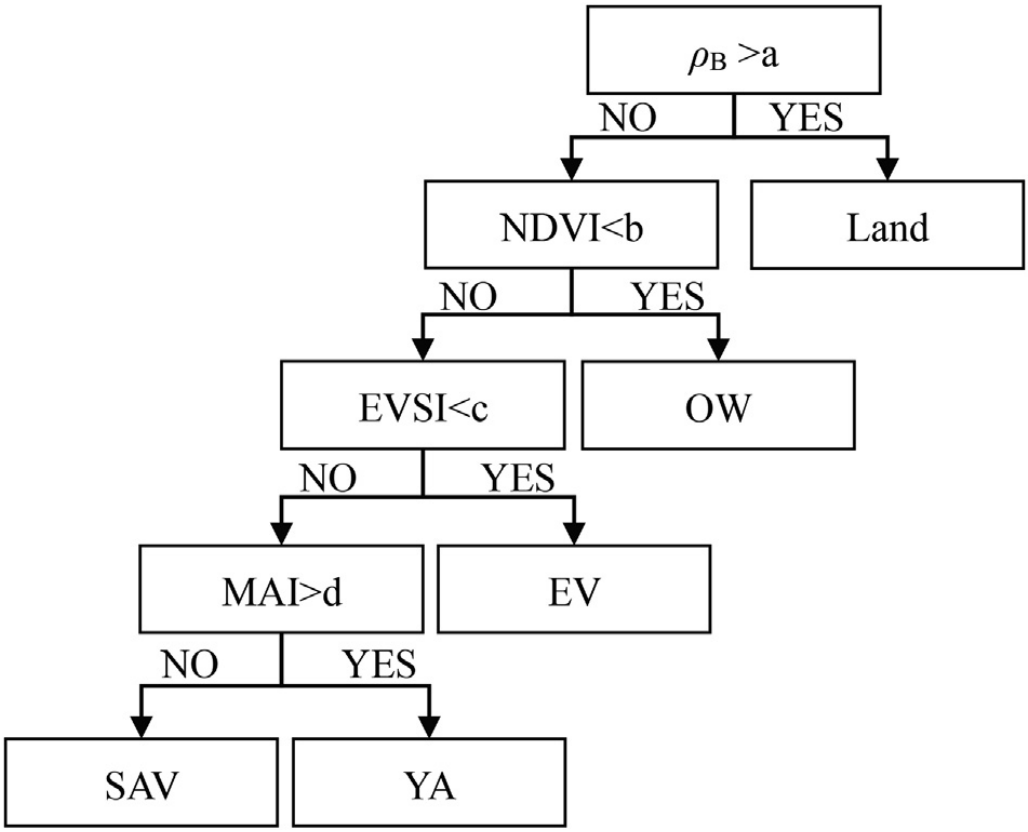

Figure 2.22: Decision tree model for distinguishing emergent vegetation, sub-merged aquatic vegetation, yellow algae, open water and Land. They exploited thresholds a, b, c and d. (Source [55]).

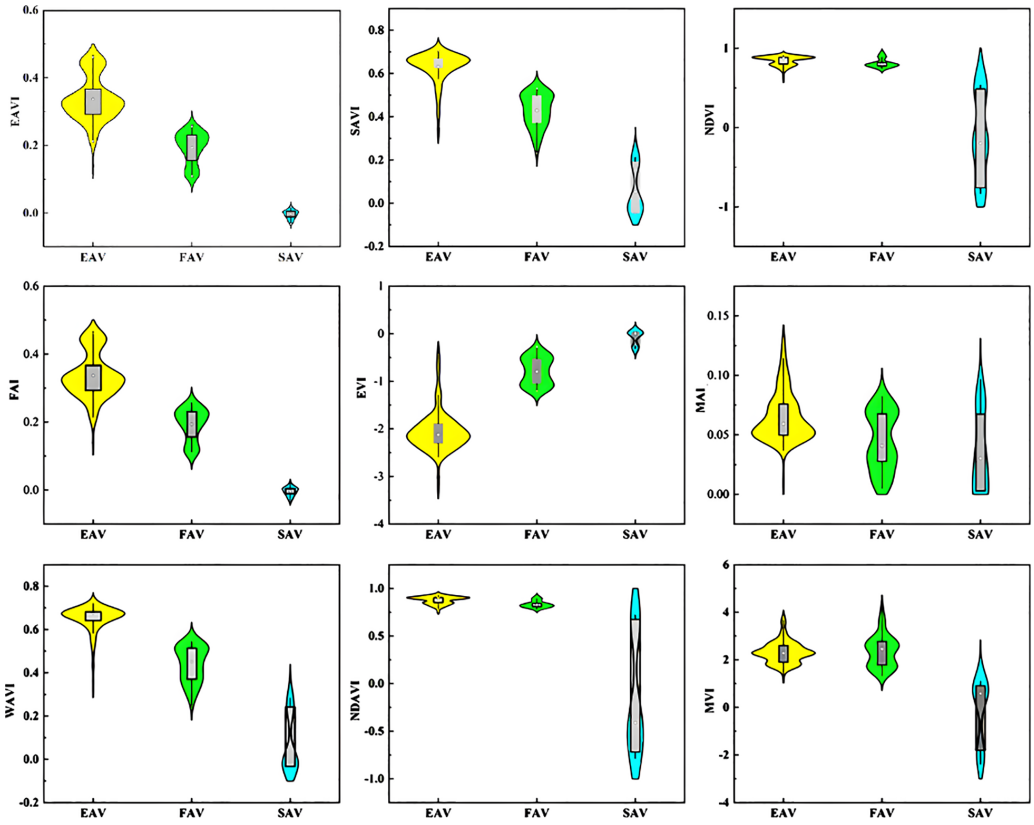

Figure 2.23: Comparison of nine remote sensing indices for distinguishing the three categories of Aquatic Vegetation (AV), namely EAV, FAV and SAV (Emergent, Floating-leave and Submerged AV). (Source [80]).

the prevailing development of the plants inside, outside, or on the surface of the water. They reported the results in a set of box-violin graphs shown in Figure 2.23, from which it is possible to identify the best performing indices for this specific objective.

The study [27] on the trend of aquatic vegetation observed over 15 years in 25 large Chinese lakes is particularly interesting because it correlates the results with fertilizer consumption and climate change. An analysis was performed using a multiple general linear model, which revealed that the amounts of chemical fertilizers used on agricultural land surrounding the lakes

played the most important role in regulating interannual changes in vegetation greenness. The authors used MODerate-resolution Imaging Spectroradiometer (MODIS) data. Their research proposes an advanced algorithm for processing NDVI data, as shown in 2.24b. Equally noteworthy is the 2.24a graph, which shows the uncertainty in using the index to interpret various types of aquatic vegetation.

A different objective is pursued in [67], which focuses on a major Indian city, Telangana. Through a comparative analysis of NDVI, NDWI, and LST (Land Surface Temperature) values obtained from Landsat satellites over the 2000–2020 period, the study seeks to demonstrate the proportional relationship between the decline of urban vegetation, changes in precipitation patterns, and a concurrent rise in surface temperatures. These temperatures consistently remain higher than those in the surrounding rural areas and often exceed 40°C during the summer. To mitigate this critical issue, the authors recommend increasing green areas and water surfaces within cities. Only images with less than 2% cloud cover were used—a frequent condition in the studied area, which has experienced a reduction in green spaces due to rapid urbanization driven by the growth of a major IT hub. In this context, the combined use of NDVI and NDWI improved the accuracy of vegetation assessments in built-up areas.

A distinct approach is presented in [40], where NDVI, NDWI, and ten additional indices are used in a novel way to train a machine learning model that produces a map of urban quality of life—an especially valuable output for the target city located in an arid region of the United Arab Emirates.

The study by [34] investigated turbidity variations in tropical reservoirs across India from 2016 to 2021, employing the Google Earth Engine (GEE) platform and Copernicus satellite data. Their approach relied on the Modified

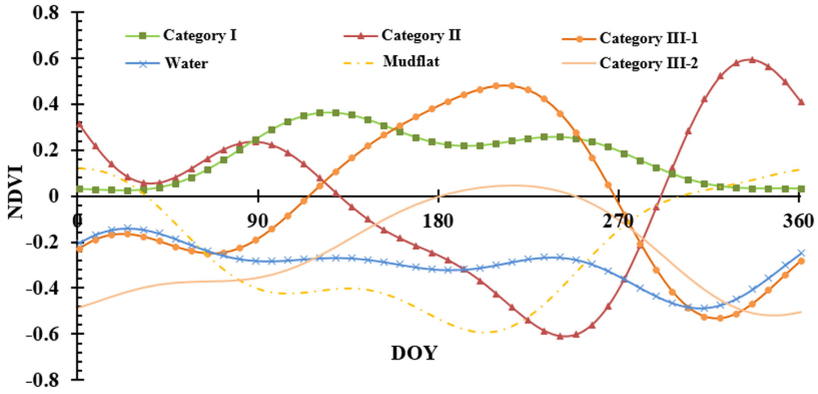

(a) Annual NDVI series (derived using MODIS 8-day composites) of different wetland cover types. Categories I to III represent vegetation with different growing conditions.

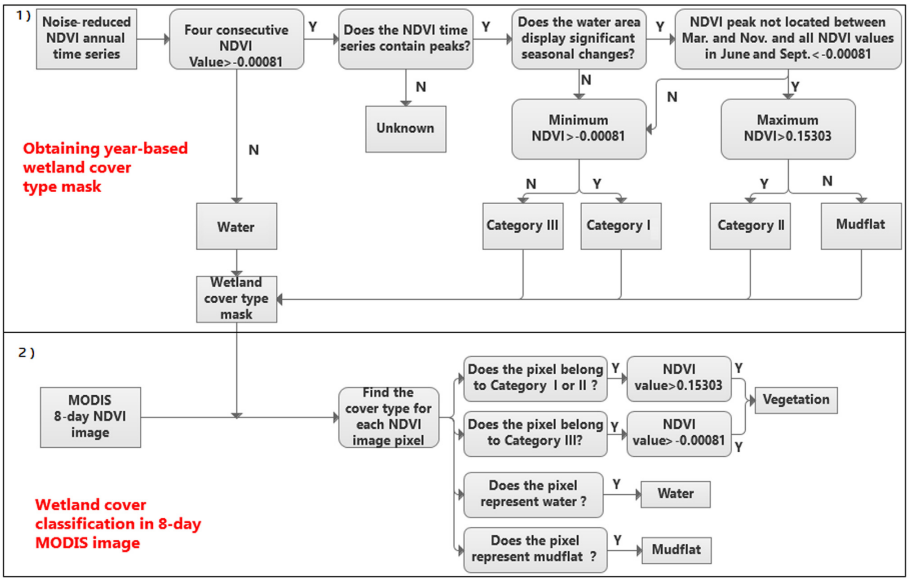

(b) Workflow used to generate the year-based possible vegetation occurrence mask using the NDVI series in each year. (2) Workflow of using the year-based possible vegetation occurrence mask to perform vegetation classification for each 8-day NDVI composite.

Figure 2.24: The classic RF index NDVI is used to classify water cover based on vegetation types (Source [76]).

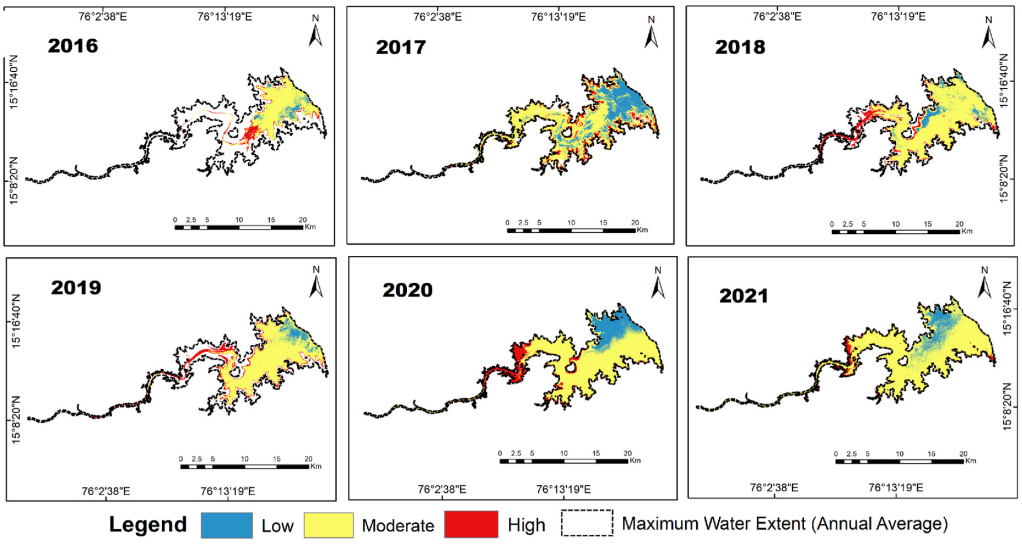

Figure 2.25: Mapping of temporal trend of low, moderate and high levels (average of turbidity levels) in Tungabhadra tropical reservoir (India) for 2016–2021. (Source [34]).

Normalized Difference Water Index (MNDWI) to evaluate water body profiles and incorporated in-situ validation using the Earth Observing and Mapping (EOMAP) water quality portal. Their classification of reservoirs by turbidity level provides an insightful benchmark for assessing the effectiveness of optical indices under different environmental conditions. The resulting map is shown in Figure 2.25.

Similarly, [1] analyzed an Indonesian river subjected to high anthropogenic pressure near its delta, which is characterized by mining, port, and industrial activities. Utilizing GEE and Sentinel data, the authors applied a GIS-based visualization method to delineate the river course, which was otherwise difficult to identify in post-processed NDTI imagery. Reported turbidity values ranged between 253.57 and 437.80 NDTI units across two temporal acquisitions. Although this metric differs from the standardized NDTI scale, the magnitude of variation reported aligns closely with the results observed in

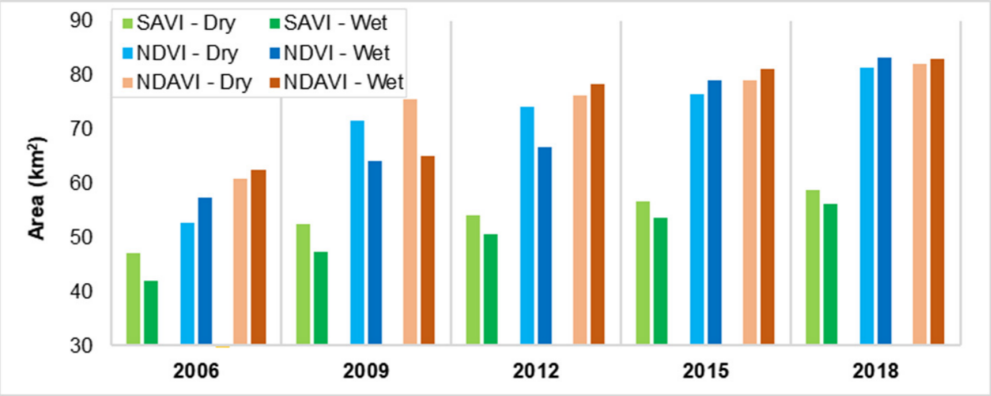

Figure 2.26: NDVI, SAVI, and NDAVI areas in Lake Titicaca for dry and wet periods. (Source [4]).

my research, underscoring the consistency of remote sensing–derived turbidity patterns across diverse contexts.

Remote sensing is also used in [4] to measure turbidity. It is calculated together with chlorophyll because both are considered effective indicators for investigating water quality and detecting changes in the nature of soil cover in a lake located in the Bolivian Andes. Authors have also assessed Land Use/Land Cover (LULC) changes by measuring other indices, namely the Soil Adjusted Vegetation Index (SAVI) and the Normalized Difference Aquatic Vegetation Index (NDAVI), together with the ubiquitous Normalized Difference Vegetation Index (NDVI). Their findings are reported in Figure 2.26.

In [8], the authors classify turbidity by relating it to its mean value in the reservoir created by the Panchet Hill Dam, India, obtaining three classes: low turbidity, medium turbidity, and high turbidity. The assessment is shown in Figure 2.27.

Another relevant contribution [19] explored the use of Sentinel imagery (for the year 2021) to assess the potential of several vegetation- and water-related

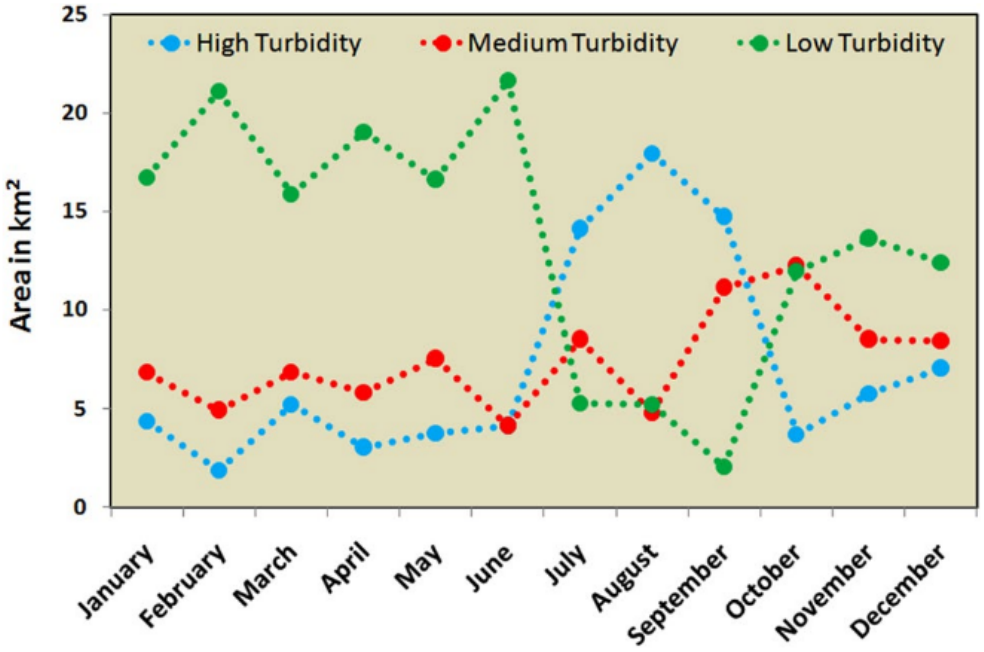

Figure 2.27: Superimposition of high turbidity, medium turbidity and low turbidity coverage of the Panchet Dam, 2015. (Source [8]).

indices—such as the Normalized Difference Vegetation Index (NDVI), Green Normalized Difference Vegetation Index (GNDVI), Normalized Difference Aquatic Vegetation Index (NDAVI), Green Red Vegetation Index (GRVI), and Normalized Difference Water Index (NDWI)—for detecting the extent of duckweed infestations in the Lis River (Portugal). This research is particularly pertinent given the morphological and environmental similarities between the Lis River and the Mincio, as well as the broader Po Valley region. The authors emphasized that field-based surveys remain constrained by limited accessibility to infested areas, reinforcing the value of remote sensing as a viable monitoring alternative.

When large-scale coverage is required, remote sensing emerges as an indispensable tool, offering extensive spatial reach and frequent temporal acquisition at a fraction of the logistical cost of conventional methods. By refining these detection capabilities, this study contributes to a deeper understanding of the spatiotemporal dynamics of turbidity, their potential anthropogenic drivers, and the impacts on riverine and lacustrine environments. The methodology provides a foundation for future investigations aimed at quantifying the environmental perturbations caused by agricultural and industrial discharges.

Chapter 3

IoT for Monitoring Livestock Wastewater

Following the operational context introduced in Chapter 2, the study presented in this thesis focuses on the management, tracking, and reporting of effluent transportation activities, specifically addressing the stakeholders involved in this particular supply chain, as clarified in this section.

3.1 Context and Objectives

Livestock companies are required to spread slurry over a sufficiently large area in proportion to the number of animals they farm. Suitable and adequately extensive land, however, is not easily available in sufficient quantities, which forces large companies to undertake long and costly deliveries while also increasing the resulting greenhouse gas emissions.

Despite the critical nature of manure spreading operations, local authorities in the Po Valley region do not conduct rigorous or timely inspections of such operations. In fact, wastewater spreading operations are subject only to

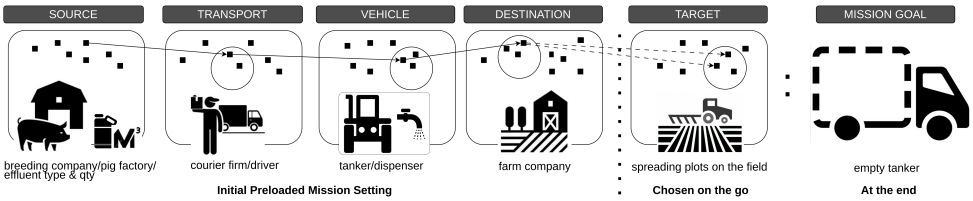

Figure 3.1: Main entities involved in the reference use case and operational phases within the application context.

prior notification and final reporting. Surprisingly, no automated procedure currently supports this high-risk activity. Consequently, tanker truck drivers may commit errors during their missions, while both the companies involved and the regulatory bodies responsible for these operations suffer from a lack of information and monitoring tools.

Figure 3.1 schematically illustrates the group of entities involved in the target use case, along with the essential operational phases across the entire supply chain, which includes waste producers, tanker truck drivers, farmers, regulatory bodies, and consulting firms. During each mission, a pig farm assigns the disposal of livestock effluents to a transport company, which then selects a tanker truck and an agricultural receiving company from among its partners. The tanker is loaded at the farm and transported to a designated field identified by the farmer for effluent discharge.

This research aims to address the considerable lack of information and awareness regarding how manure spreading missions are conducted, and to develop a prototype system capable of reducing failures resulting from inattentive driving while enabling accurate control and tracking of operations. To this end, the proposed solution employs the drivers' own mobile phones during effluent transport missions. Drivers are guided and monitored in real time through an intuitive mobile application, thus eliminating the need for

dedicated hardware.

Using their devices, drivers transmit their positions to headquarters, which are instantly reflected on an interactive map displaying the necessary information to correctly perform the assigned tasks. This navigation system allows drivers to traverse complex and unmarked target areas more easily, ensuring accurate effluent distribution. Moreover, drivers receive timely notifications when exiting designated zones, thereby preventing accidental waste discharge.

Supervisory authorities and participating companies can monitor operations by observing the progress of each mission, either in real time or retrospectively. The relevant telemetry data generated during these missions are stored and made accessible to stakeholders for a wide range of purposes, including data mining queries, analytical assessments, and decision-support activities—addressing the significant gap previously mentioned.

The ultimate goal is to provide this management system, at a prototypical stage, tested on several pilot missions involving approximately ten companies within the supply chain and utilizing their real operational data. The prototype aims to be ready for deployment in a broader, fully realistic scenario. The system is designed to facilitate the precise and efficient execution of transport and spreading missions, helping operators minimize maneuvers that may cause pollution events. Furthermore, it will begin to accumulate a substantial and accurate dataset concerning the locations and quantities of livestock effluents discharged, which will be made publicly available in anonymized form to researchers and regulatory agencies engaged in environmental studies on the impact of the livestock industry.

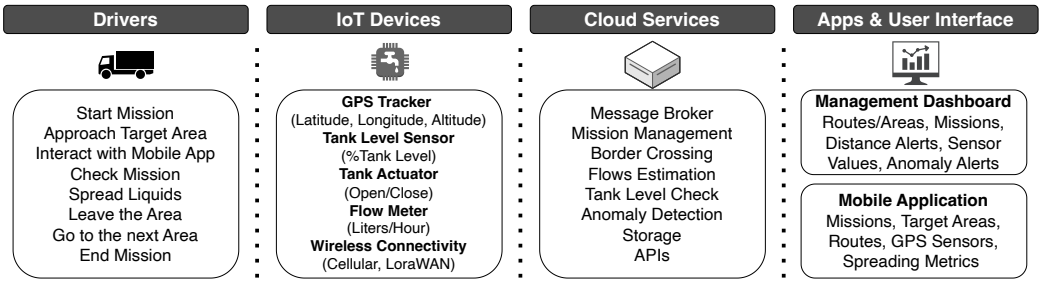

Figure 3.2: List of architectural entities with main functions, responsibilities, and interaction flows.

3.2 System Design & Architecture

Building upon the requirements and characteristics of the reference use case described above, this section outlines the design of an IoT-based architecture for monitoring wastewater distribution activities. The initial phase involved identifying the key architectural entities and defining their respective responsibilities and interaction models throughout the various operational stages.

Figure 3.2 enumerates these components along with their primary functions. In the proposed architecture, the system revolves around several core entities, each playing a crucial role in ensuring smooth mission execution and effective data management. At the forefront are the drivers who are responsible for executing missions from start to finish. Their tasks range from initiating the missions and navigating toward designated target areas to successfully completing the assigned activities. These drivers interact with the mobile application or IoT devices to determine their positions and perform distribution operations.

Essentially, IoT devices enrich the architecture by providing additional key telemetry data—such as tank level monitoring, discharge valve actuation,

and flow rate measurement of the spreading process—while the GPS device keeps these operations georeferenced. Interconnected through wireless communication channels such as cellular networks or LoRaWAN, these devices transmit real-time data to the headquarters, which is crucial for the mission's success. In scenarios where IoT devices are unavailable, their contributions are substituted by the mobile application, including the integrated GPS features of the phone.

Centralized data management is fundamental to the system's effectiveness, supported by a robust cloud-based infrastructure. These cloud services include message communication, mission management (such as boundary crossing detection and discharge flow estimation), and anomaly detection to trigger timely alerts. Furthermore, the cloud platform provides extensive data storage capabilities and offers APIs for seamless integration with external applications. From the user perspective, both user and application interfaces serve as essential tools for managers, stakeholders, and drivers. The management and reporting dashboards provide comprehensive visualizations of routes, missions, alerts, and sensor data, offering users valuable insights to support decision-making. At the same time, the mobile application provides drivers with detailed mission information, navigation guidance, and real-time sensor metrics, promoting efficient and well-informed field operations, whether through direct interaction or IoT-assisted communication.

The identified components are illustrated in the architectural diagram (Figure 3.3), which depicts their main functionalities and interrelations. At the periphery of the modeled scenario, drivers operate tanker trucks to transport effluents to the designated target areas while simultaneously emitting georeferenced telemetry packets. These data streams were mapped using the MQTT[1]

[1]MQTT Version 5.0 (2019) : `https://mqtt.org/mqtt-specification/`

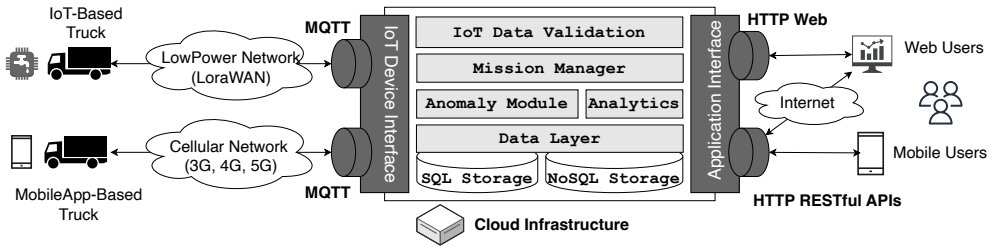

Figure 3.3: Schematic representation of the proposed IoT architecture with the involved modules and interaction with both IoT device and external applications and users.

protocol through dedicated topics, following a Publish/Subscribe (Pub/Sub) approach, enabling routing toward a standard broker that distributes the data to all internal applications within the architecture that require it.

The data are then made accessible to the Mission Manager, the core component and engine that initializes the system and executes the business logic. The Mission Manager stores the data in a central database and processes it for a range of critical purposes—the most important being geofencing (supervision of tankers approaching and crossing designated boundaries), estimation of the discharged waste flow (to compensate for the possible absence of dedicated hardware sensors), and monitoring of empty tank status (necessary to conclude missions normally).

The Mission Manager has another essential responsibility: maintaining a consistent mission state (represented by a series of internal attributes) over time and handling the various situations encountered by the driver during mission execution. To achieve this goal, the Manager exposes mission state information and receives feedback from mission agents—in other words, it interacts with both the field driver and the office personnel through a dedicated user interface composed of the aforementioned dashboards, accessible as a

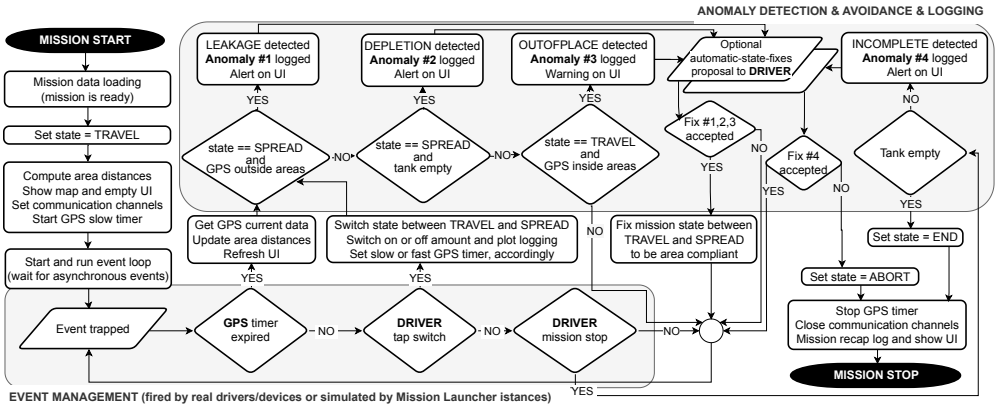

Figure 3.4: Flow chart of the designed mission management mapping the identified functionality requirements.

web or mobile application.

Finally, the Anomaly Module detects various operations that may represent anomalous behaviors, as described in the following paragraphs.

The algorithm governing the mission phases is illustrated with a flowchart in Figure 3.4 and by its pseudocode in Algorithm 1. It tracks the movement of a tanker truck across rural areas. Executed by the Mission Manager, which leverages the Anomaly module, the algorithm responds to driver interactions and listens for signals from IoT devices. Regardless of whether they originate from real or simulated entities, these events trigger state transitions, as illustrated in the gray box at the bottom of the figure.

Algorithm 1 Event–Driven Mission Control with Anomaly Detection

Input: Mission configuration, spreading areas, vehicle sensors

Output: Mission log and final mission state

```
1  Load mission data  state ← TRAVEL
2  ComputeAreaDistances()  InitializeUI()  OpenCommunicationChannels()  StartGPSTimer(slow)
3  while state ≠ END and state ≠ ABORT do
4      WaitForEvent()
5      if event == GPS_TIMER_EXPIRED then
6          gpsData ← GetGPSData()  UpdateAreaDistances(gpsData)  RefreshUI()
           // Anomaly detection tests
7          if state == SPREAD and GPSOutsideAreas(gpsData) then
8              LogAnomaly(LEAKAGE)  AlertUI()
9          if state == SPREAD and TankEmpty() then
10             LogAnomaly(DEPLETION)  AlertUI()
11         if state == TRAVEL and GPSInsideAreas(gpsData) then
12             LogAnomaly(OUT-OF-PLACE)  WarningUI()
13     else
14         if event == DRIVER_SWITCH then
15             ToggleState(TRAVEL, SPREAD)  ToggleLogging(AMOUNT,PLOTS)
16             if state == SPREAD then
17                 StartGPSTimer(fast)
18             else
19                 StartGPSTimer(slow)
20         else
21             if event == DRIVER_MISSION_STOP then
22                 if TankEmpty() then
23                     state ← END
24                 else
25                     LogAnomaly(INCOMPLETE)  AlertUI()
       // Optional automatic anomaly fixes offered to the driver
26     if AutomaticFixProposed() then
27         if DriverAcceptsFix(LEAKAGE,DEPLETION,OUT-OF-PLACE,INCOMPLETE) then
28             FixMissionStateAreaCompliant()
29     if state == INCOMPLETE) then
30         state ← ABORT
31 StopGPSTimer()  CloseCommunicationChannels()  GenerateMissionRecap()  ShowUI()
```

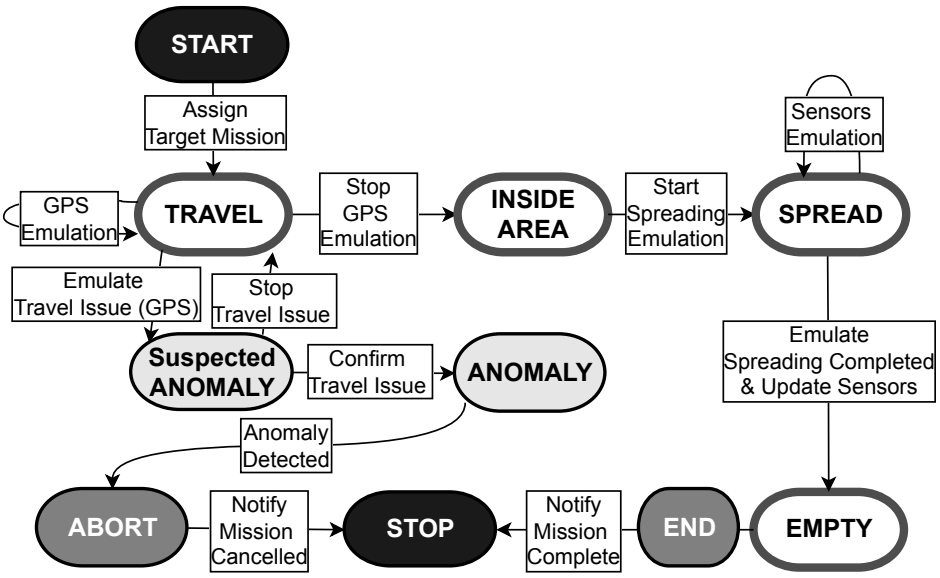

Figure 3.5: Mission main phases and transitions.

The vehicle position is continuously monitored, prompting the driver to select the intended spreading targets when in proximity. The driver confirms the start of the spreading process, which continues until specific termination conditions occur, such as reaching the boundary of the target area, emptying the tank, or manually interrupting the operation. These actions may be repeated in multiple areas until the tanker is emptied, with the mission's fundamental states transitioning from TRAVEL (toward the destination site) and SPREAD (effluent distribution) to ABORT (incomplete mission) or END (successful conclusion).

The evolution of a typical mission is reiterated in Figure 3.5, which presents the state diagram. The INSIDE AREA state occurs when the tanker moves within a target area without performing spreading—likely a temporary situation. When the effluent in the tank is depleted, the EMPTY state leads to the terminal END of mission state, representing a successful outcome. The

Suspected ANOMALY and ANOMALY states may either be confirmed as fatal errors causing mission cancelation or dismissed as recoverable warnings.

The system collects a limited set of data, including GPS coordinates, reference timestamps, and driver inputs/selections, continuously updating mission status, visited target areas, and calculating the quantities of waste discharged based on distributor performance and spreading duration. All relevant mission data is logged, enabling stakeholders to reconstruct missions and query datasets as needed.

Supporting the driver, the algorithm promptly detects and reports some anomalous spreading situations—collectively referred to as anomalies—likely the result of driver inattention and, in any case, considered undesirable. The system also tracks these events and, where possible, suggests automatic corrective actions. These situations occur when: 1. spreading is detected as ongoing, but the tank is empty; 2. spreading occurs outside designated areas; 3. the tanker moves within dedicated areas without performing spreading; 4. the tanker continues moving with an empty tank instead of declaring mission completion; or 5. the mission is declared complete without having fully emptied the tank.

3.3 Use Case and Developments

This section delves into the specific characteristics of the target application scenario, along with the implemented architectural prototype and the partial integration of its components. Preliminary results are presented, demonstrating the capabilities of the proposed approach in collecting target data, monitoring component behavior, and presenting data through dedicated views and dashboard modules.

3.3.1 The Po Valley

As previously anticipated, this study focuses on the dissemination of livestock effluents across the rural areas of the Po Valley through specific and configurable missions. The system was initially developed to serve a pilot group of stakeholders composed of several companies based in the provinces of Mantua and Cremona, whose cadastral plots are represented by the blue polygons on the map in Figure 3.6.

Figure 3.7 schematically summarizes the mission phases, which involve multiple parties with whom collaboration agreements have been established. A pig farmer assigns the disposal of livestock effluent. A tanker is loaded at the farm, transported to a receiving agricultural company, and discharged at a designated field identified by the farmer.

Due to the high volume of waste produced and the limited capacity of the tankers, numerous missions are carried out daily, with hundreds of trucks operating across the Po Valley. Effluent spreading must be carefully managed to prevent localized pollution, making it essential to identify sufficiently large and suitable spreading areas. However, this task is demanding and often requires long-distance travel, resulting in increased mission duration, fuel and personnel costs, vehicle wear, and environmental impacts.

3.3.2 Mission Management System Simulator and Prototype

With the objective of developing a functional and robust prototype of the Mission Manager, an opportunity arose to begin by creating an accurate software-only simulation environment. Given the complexity of this supply chain, a simulation environment specifically designed with simulated entities

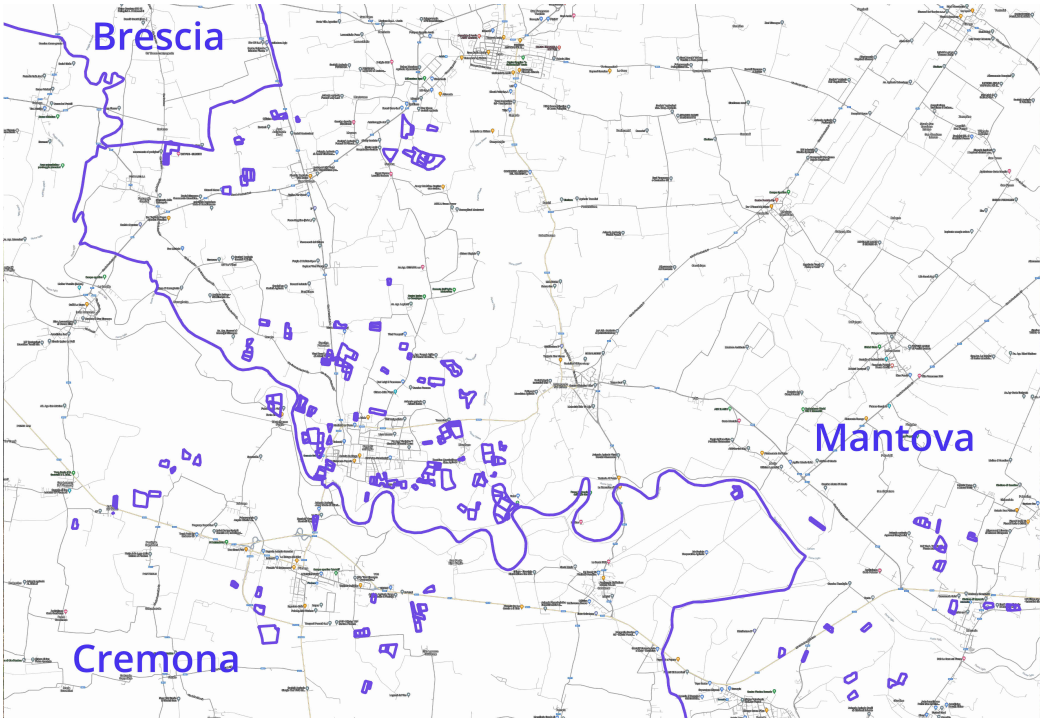

Figure 3.6: The map of target areas in the geographic Region Of Interest to be used for prototype testing.

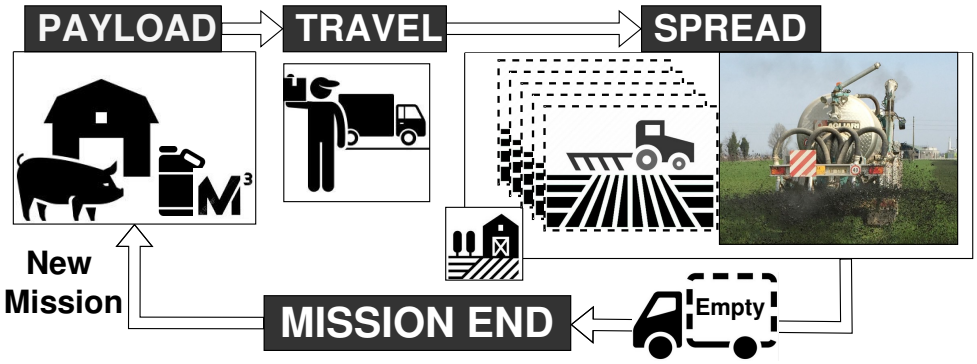

Figure 3.7: Schematic representation of the spreading procedure.

corresponding to real system counterparts represents a strategic resource to support the development of production infrastructures and services, as well as to identify limitations and anticipate challenges, thereby facilitating the implementation of a real-world monitoring solution—starting with the essential GPS tracker that records the routes followed by tanker trucks distributing effluents from intensive livestock farms. During the implementation of the real system, as actual devices become available, they will replace the simulated modules. According to the substantial goals defined for the stakeholders (mentioned later), the simulator reproduces the significant behaviors of drivers conducting spreading activities while engaging stakeholders under established agreements and responsibilities.

The simulator enables the design of all operations, as well as the testing and implementation of a future IoT solution for livestock waste spreading, effectively supporting all stakeholders. This model provides several services:

- *Assistance:* guiding drivers to carry out missions effectively and allowing office personnel to monitor activities in real time;
- *Anomaly detection:* helping drivers avoid mission anomalies by detecting, storing, and reporting them;
- *Accounting:* recording and reporting activities to improve transparency and ensure compliance with policies;
- *Optimization:* identifying the most relevant data to improve future missions

The simulator was developed first, with the specific aim of pre-testing as many functions as possible and then deriving the prototype's main functions from it. Therefore, the simulator and the prototype share a significant portion

<table>
<tr><td></td><td colspan="3">MANAGER VERSIONS</td></tr>
<tr><td>Features</td><td>MISSION
SIMULATOR</td><td>PROTOTYPE</td><td>FULL IoT
DEVICEs</td></tr>
<tr><td colspan="4">CONTROL</td></tr>
<tr><td>Vehicle control
Plot choices
Spread timing</td><td>from GPX</td><td colspan="2">Real driver</td></tr>
<tr><td colspan="4">MEASUREMENTS</td></tr>
<tr><td rowspan="2">Vehicle position/speed</td><td>from GPX</td><td colspan="2">cell phone GPS</td></tr>
<tr><td rowspan="2">Effluent quantity left
Effluent discharge rate</td><td colspan="2">Estimation</td></tr>
<tr><td>IoT gauge</td><td>IoT flowmeter</td></tr>
<tr><td colspan="4">NOTIFICATIONS</td></tr>
<tr><td rowspan="2">Alerts to
Reporting to</td><td>Logs</td><td colspan="2">Driver & logs</td></tr>
<tr><td colspan="3">Database</td></tr>
<tr><td colspan="4">USER INTERFACE</td></tr>
<tr><td>Map Widget
Plots Grid
Spreading Dashboard
Mobile custom APP</td><td>Read only</td><td colspan="2">Active</td></tr>
<tr><td>Completion</td><td>Completed</td><td>Test & deployment</td><td>Future plans</td></tr>
</table>

Figure 3.8: Mission Manager feature comparison matrix.

of the code set. So much so that both the state diagram of the spreading missions shown in Figure 3.5, the flow chart depicted in Figure 3.4 and the pseudocode reported in 1 apply to both; we refer to these for a better understanding of the description below. The fundamental difference between the system prototype and its simulator lies in the management of the events affecting the behavior of missions (enclosed in an inset in Figure 3.4), i.e., the signals arising from the system's hardware components (GPS detector and IoT devices) and the choices made by the human operator (the tanker driver), compared to their software-simulated counterparts. This distinction, which represents a well-defined portion of the work, is highlighted where relevant and summarized in the table in Figure 3.8. Aside from these differences, the description that follows applies to both the simulator and the prototype. It is emphasized that the implemented prototype does not yet include the full set of hardware devices; however, it has been designed to accommodate the development of the complete version, as conceptually illustrated in the table. Among the differentiated components that the 3.8 table reports, the "MEASUREMENTS" section shows that four data values are detected by real sensors : the speed and position of the vehicle (acquired via a GPS device), the level of the waste tank (monitored by a meter), and its dispensing device operating at a specific flow rate (detected by a flow meter). In the simulator, these same data are prepared in advance and stored in a customized GPX file, randomized by carefully designed procedures to ensure their validity. The "CONTROL" section of the 3.4 table lists other events that determine the mission's progress, specifically those not deriving from hardware components. These include the vehicle's route, the choice of fields where the spreading occurs, and the timing of the spreading. In real missions, these are controlled by the driver; in simulated missions, they are pre-set to complete the tasks or

lead to one of the anomalies tracked by the system. All this demonstrates the complete equivalence between the behavior of the mission simulator and the prototype manager of real missions. And it allows for a common description of them while highlighting any appropriate differences in the text.

The missions are fully configurable, allowing for complete testing of all components before deploying field implementations. The simulated missions replicate real-world scenarios—thus avoiding costly on-site operations—and encompass all stages of standard missions, following the mission flow previously described and illustrated in Figures 3.4 and 3.5.

The system is designed to manage multiple tankers simultaneously. The prototype is fully functional, but it's an early version that hasn't been optimized. In particular, the code that updates the distances between the tanker's position and the potential fields for spreading should be addressed, as it consumes two-thirds of the processing time. In the current version, the system can support around ten simultaneous missions if run on a medium-powered PC. Without much effort, a rewrite to avoid unnecessary recalculations or the use of a GPU's API could reduce the load by a third and scale the solution to several dozen concurrent missions. Real-world scenarios, with hundreds of missions, may require adequately powerful servers. The system supports hybrid operation, combining both simulated and real vehicles, with the latter being managed by the prototype. Each mission is characterized by numerous operational parameters. These parameters—typically set by the driver during real missions—are configured in advance in simulated missions via a Mission Launcher module and can either be stored in a database or generated dynamically as needed.

Parameters include participating companies, driver assignment, tanker travel speed, traversal of discharge areas, spreading flow intensity, and the

route to follow. In simulated missions, the vehicle follows a preloaded route in GPX format, with waypoints retrieved via Google Maps. The portions of the route where spreading occurs within designated areas are simulated using a specific algorithm that ensures the tanker empties its contents before mission completion.

In all cases, telemetry data and sensor readings—including vehicle movements—are continuously published via MQTT topics on the underlying network, ensuring reliable communication with MQTT subscribers and the timely availability of data in the central collection hub.

Furthermore, mission settings such as distance reporting, log verbosity, and output formats are configurable for both real and simulated missions. All mission-related and telemetry data are stored in a centralized database for analysis and monitoring.

In implementing the envisioned architectural design, the system leveraged the capabilities of the ThingsBoard[2] platform, which is specifically dedicated to the IoT domain. This platform was utilized to develop key components and configure the foundational infrastructure, thanks to its flexibility and modular architecture, which facilitates data acquisition, processing, and visualization through a suite of dedicated dashboards and a customizable mobile application.

The ThingsBoard services employed include MQTT-based communication (and potentially other protocols such as HTTP or WebSocket), consistent for both physical and emulated devices; a digital interface exposing data via RESTful APIs; and flexible, customizable web dashboards for mission and activity monitoring, data presentation, and system interaction—benefiting both drivers and office operators.

[2]Thingsboard Platform (2016) : `https://thingsboard.io/`

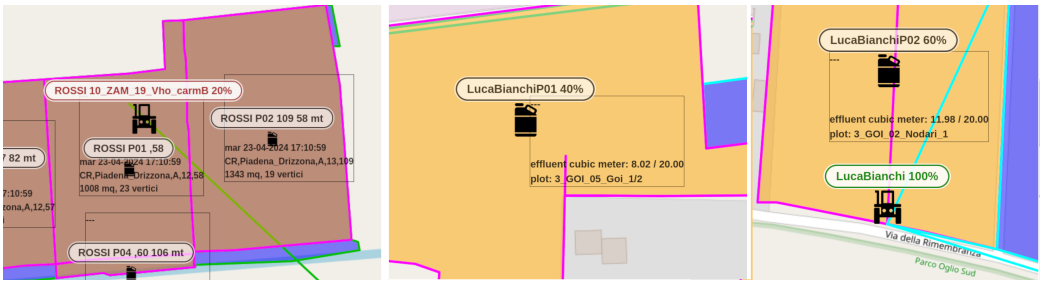

Figure 3.9: The developed dashboard with the tracked vehicles during their activities with live updates and data synchronization from the field.

Of particular importance, the platform provides a native mobile application that makes these dashboards accessible on smartphones, enabling drivers to use them directly during field operations. This ubiquitous accessibility makes ThingsBoard the ideal integration layer, connecting all components and enabling the practical realization of the proposed architecture—facilitating communication between the centralized server that collects traceable events and the peripheral devices accompanying operators in the field.

3.3.3 Architecture Implementation

At the headquarters, the core of the architecture is the Mission Manager, responsible for MQTT telemetry subscriptions, activity logging, and data collection from tanker trucks, supported by the Data Validation Module. This component processes incoming events, validating data against general spatio-temporal constraints and interfacing with an internal SQL database for subsequent physical storage.

An Anomaly Module was also implemented to verify driver operations during missions, ensuring their logical consistency with the current state of the mission and detecting potential anomalies in trajectory and movement data.

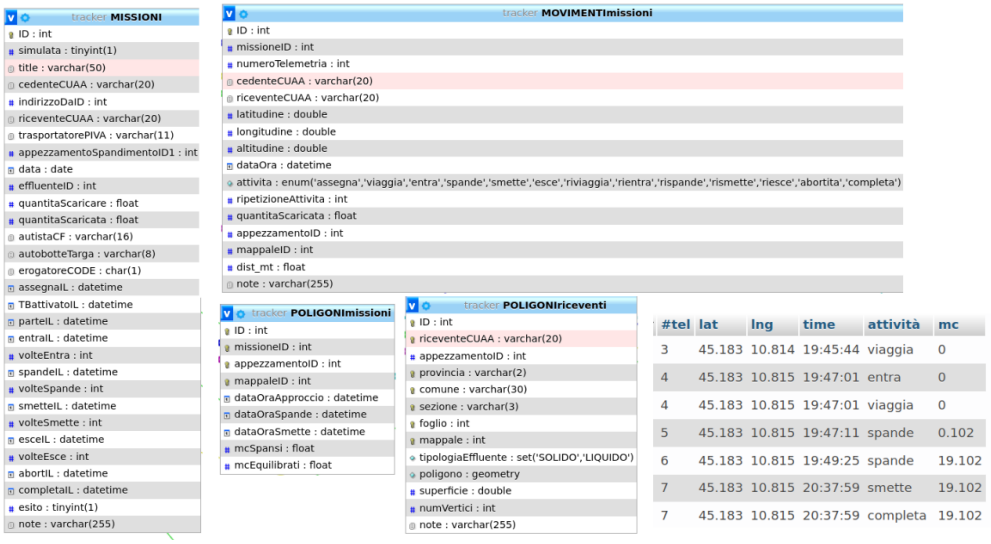

Figure 3.10: Essential data is stored in the database.

At the field level, activity capture, visualization, transmission to headquarters, and real-time monitoring are made possible through the map dashboard illustrated in Figure 3.9. Drivers are represented by pseudonymous identifiers. The map on the left shows potential discharge target areas highlighted in brown, marked with small canister icons and accompanied by detailed labels. The driver—identified by a tractor icon—can easily assess distances and area sizes to decide where to operate, confirming his selections directly via the dashboard.

Drivers also report the start and end of spreading activities, allowing the system to record the areas involved, the timing, and the quantities discharged on the central server for accurate monitoring, as illustrated in Figure 3.10. On the other dashboards, a typical end-of-mission scenario is displayed, where enlarged canister icons mark the actual discharge areas (highlighted in ochre), with labels showing both absolute and percentage quantities discharged.

In the dashboard shown in Figure 3.11, two missions are tracked; the

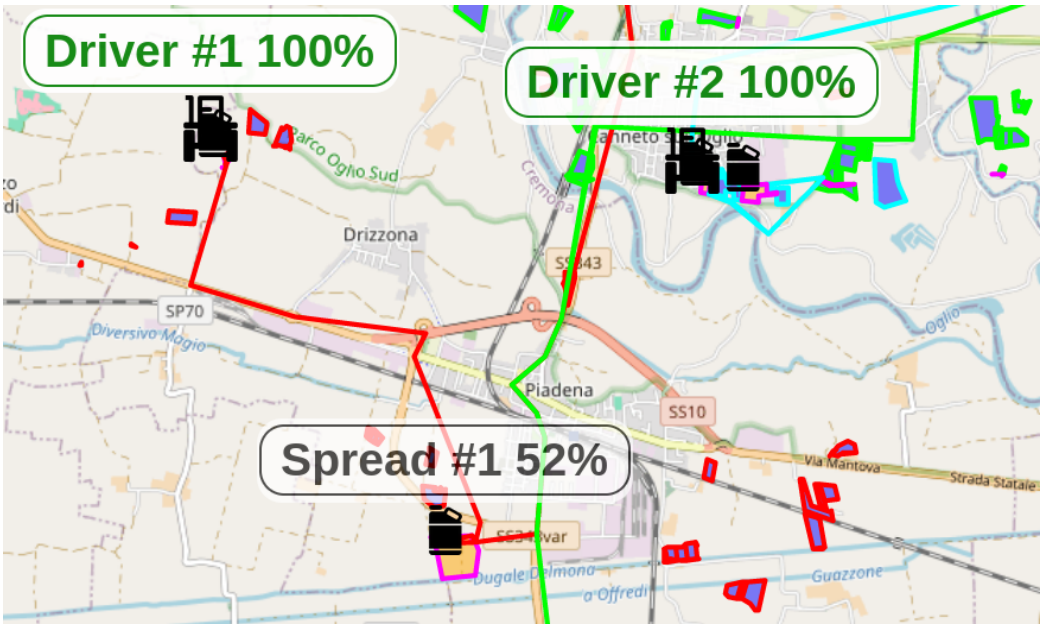

Figure 3.11: Simulation monitoring dashboard with core elements.

green labels indicate successful completion. The paths followed by the two vehicles are distinguished by color, with each driver assigned an individual color—red for one and green for the other in this case. Figure 3.12 completes the description of the implemented system, illustrating the key steps that guide drivers through mission execution.

By running multiple instances of the Mission Launcher module, several missions can be executed simultaneously, as in real scenarios. Each instance loads the planned configuration for a specific mission and virtually moves the tanker along the intended route, executing the mission as faithfully as a real one and reporting the results via MQTT.

These dashboards can be customized for personnel from regulatory bodies, companies, and consulting firms—or developed ad hoc—to provide them with the necessary data for informed decision-making.

Figure 3.12: Central diagram of the real mission, surrounded by key events as modeled by the simulator and prototype through a set of dashboards. On the left, the mission is configured and launched through the dedicated module (shown on a black background).

3.4 Conclusion

The proposed approach benefits stakeholders throughout the entire livestock supply chain — including waste producers, farmers, tanker drivers, regulatory agencies, and consulting companies — who will have access to a rich information base composed of telemetry data collected via drivers' mobile phones during delivery missions. This enables the recording of accurate datasets that would otherwise be impossible to obtain, including timely GPS positions (i.e., the entire mission path), the exact set of visited parcels, the timing and quantities of manure spreading, and any unexpected activities occurring along the route. By providing a platform for data collection, analysis, and decision support, the proposed solution aims to improve transparency, efficiency, and compliance within the livestock sector. Furthermore, the collected datasets hold promise for guiding future research and policy interventions, contributing to sustainable livestock production and environmental conservation efforts in the Po Valley and beyond.

Chapter 4

Satellite Data Analysis & Research

The research theme that concludes my work stems from the environmental challenges outlined in the introductory chapter, investigating the marks they leave on satellite imagery of the rivers and lakes surrounding the city of Mantua. We are discussing the Po Valley, a region characterized by industrial activities, including livestock farming and intensive, high-impact agriculture. It is a highly fertile territory, partly because the cultivated fields are intensively fertilized. However, irrigation and rainfall remove part of these nutrients, which are collected by the highly capillary surface water network. These suspended solids flow into the Mincio River and follow a long path, reaching the city's famous lakes, where their abundance produces effects that are clearly visible. The research investigated the turbidity behavior of the water of the Mincio River, the waterway that feeds the aforementioned Mantuan lakes. River water clarity is a key indicator of water quality and the suspended solids content; yet, it remains a relatively underexplored aspect of this phenomenon, given the effort required for a thorough assessment covering the entire course

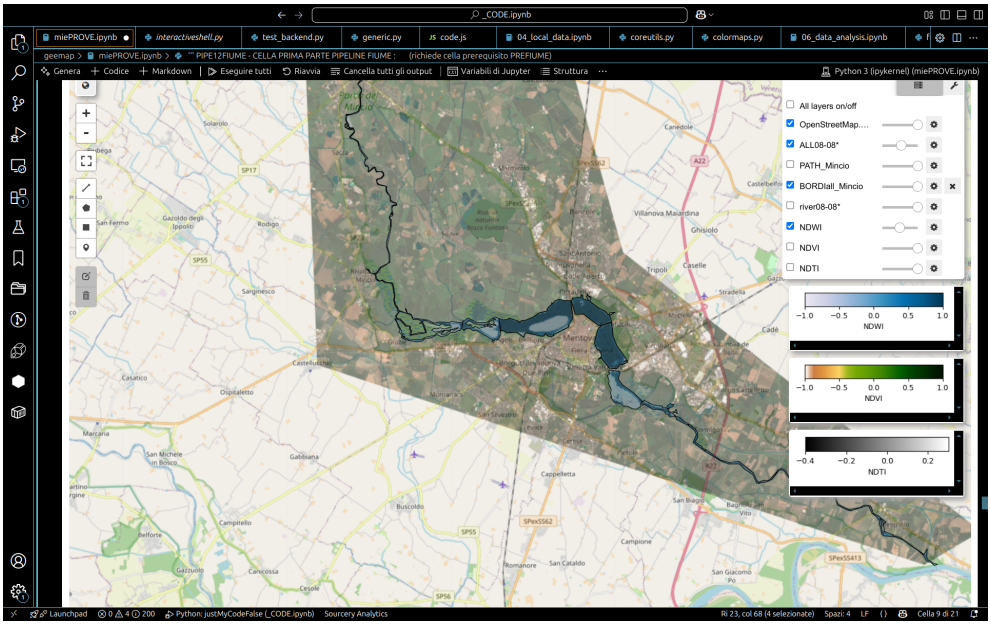

Figure 4.1: The region of interest shown via the satellite RS platform.

of a long river over a significant period of time. Satellite data allow for less expensive and highly precise analyzes, capable of revealing how the river's turbidity changes as it receives dense water from drainage channels.

These data have also enabled studies of Lake Superior, particularly regarding the intense growth of aquatic vegetation, especially invasive macrophyte species—floating broadleaf plants—that disrupt photosynthesis and threaten aquatic fauna, resulting in hypoxia and anoxia episodes. Access to a rich set of satellite data for the lake, virtually one every week over many years, has enabled the temporal monitoring of the extent of plant islands in the lake. Indeed, the research developed here uses relevant satellite imagery centered on the target Regions of Interest (ROI), as shown in Figure 4.1, to analyze the seasonal dynamics that have occurred in recent years. The system filters cloud-covered images through a dedicated spectral band for cloud detection, ensuring high-quality data. This is also because the measurement detail can

be extended down to tiny particles as small as 10 square meters [1]. The analyzes were conducted by calculating the aforementioned consolidated remote sensing indices, such as NDWI, NDVI, and NDTI, even in combination.

4.1 Aims & Objectives

This study enables the analysis of water quality in surface water bodies, including vegetation presence, turbidity, and their dynamics, through remote sensing techniques by developing a dedicated tool that can be further refined to achieve improved results. The main objectives of this research—some of which are currently in progress—include the following:

- *Tool flexibility regarding calculated remote sensing indices:* The original algorithms developed exploit the classical NDWI, NDVI, and NDTI remote sensing indices. However, they can integrate additional indices, provided that these are compatible with the spectral bands of the satellite dataset.

- *Optimizing the precision of Water-Vegetation segmentation:* When applied to the lake environment, the accurate identification of the profiles of the vegetation islands requires fine-tuning of the model settings, including the calibration of the thresholds applied to the processed indices.

- *Optimizing the precision of Water-Land segmentation and the selection of areas of application:* With reference to the river study, the original algorithms developed allow for the estimation of turbidity values exclusively at the surface of the target river. This result was achieved

[1] GEE Data Catalog - Harmonized Sentinel-2 MSI: `https://developers.google.com/earth-engine/datasets/catalog/COPERNICUS_S2_SR_HARMONIZED?hl=it#bands`

through the meticulous use of popular cartographic datasets combined with satellite rasters. A refinement was proposed to eliminate the small overlap that remained between the analyzed river zones in the current version of the algorithm that separates them. The tool also allows for precise specification of the river segments to be analyzed through a diverse set of configurable parameters.

- *Richness of result outputs:* The system produces results in multiple formats, including raw tabular data, maps, composite and hybrid mosaics, and graphical visualizations. This diversity enhances the interpretability and analytical potential of the generated outputs.

- *Accessibility of the tool to the research community:* Achieving this ambitious objective will require substantial engineering of the currently prototype-level code. In the future, the tool will be made available to researchers for evaluation and application, offering a user-friendly experience while abstracting the inherent complexities of the underlying GEE platform.

4.2 Satellite Processing Pipeline

For several decades, multiple satellite missions have generated vast amounts of georeferenced imagery, covering nearly the entire surface of the Earth. These data are made available to the scientific community through dedicated platforms, thereby enabling the development of an ever-growing number of significant research studies across diverse disciplines. Such platforms typically provide both raw and pre-processed datasets, as well as the computational resources required for their management through comprehensive programming interfaces. Some of these platforms are freely accessible to accredited

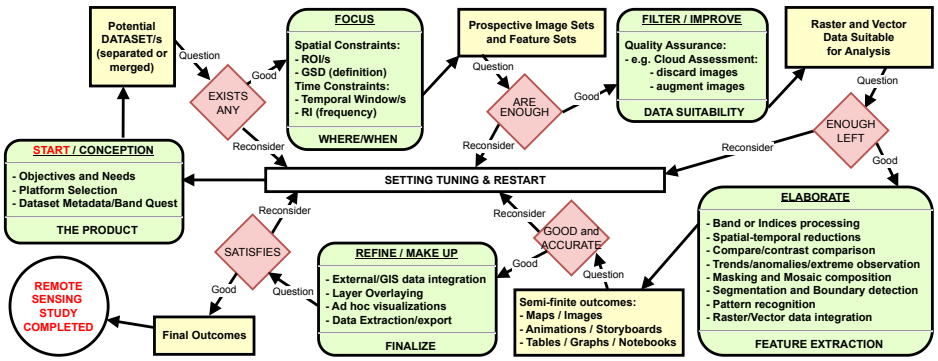

Figure 4.2: **Tasks** and **outcomes** : schematic representation of the processing activities and ensuing results involved in the workflow of a remote sensing study. ROI:Region Of Interest. GSD:Ground Sample Distance. RI:Revisit Interval. GIS:Geographical Information System.

researchers.

While this abundance of datasets and processing options represents a valuable resource, it requires careful analysis, a substantial time investment, and a structured approach to master effectively. The complexity of the tasks faced when approaching an RS project is illustrated in Figure 4.2. It can be overwhelming for newcomers to the field. As a general aid, the suggested workflow of a remote sensing project consists of many stages. The development of this study has led to the definition of a detailed pipeline comprising the four steps illustrated in Figure 4.3 and discussed sequentially in this chapter : **Data Acquisition, Pre-processing, Feature Extraction**, and **Postprocessing**. These stages encompass the retrieval of relevant satellite imagery, its refinement and enhancement, the extraction of the desired information, and, finally, the preparation and dissemination of the results to the intended audience.

In the following description, some aspects of the two themes concerning the Mantua area developed in this research will gradually emerge: one dedicated

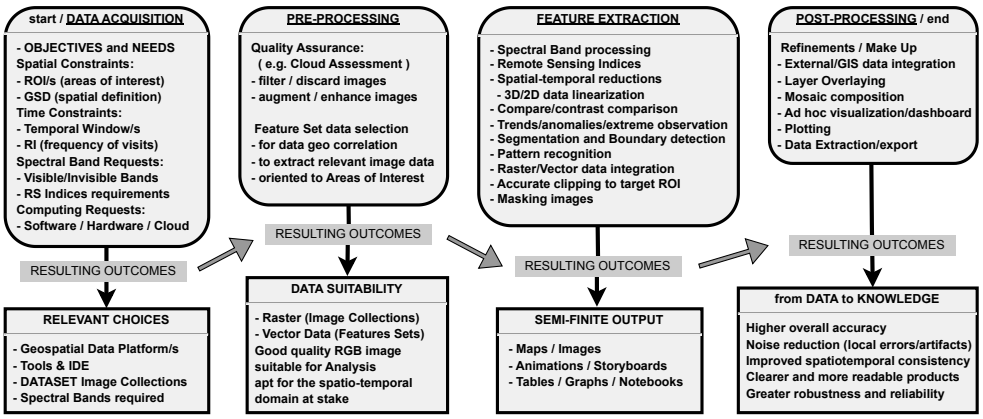

Figure 4.3: The **pipeline** : workflow of a Remote Sensing research study - the processing steps, needs, output, and common outcomes.

to the lakes and the other focused on the river. The algorithm resulting from the implementation of the adapted pipeline to extract the turbidity data of the river water is schematized in a flowchart in Figure 4.4. The highlights of the lake workflow are shown in figure 4.5

The processing pipeline developed here to undertake these tasks is designed with accessibility in mind, simplifying technical complexity for users. It displays raw and processed images side by side for easier validation and interpretation. The post-processing phase further refines and integrates the results, improving their overall quality. In particular, the analysis of river surfaces introduces an original approach, effectively segmenting the river course and reporting average turbidity values for river reaches of the required length. While current results are preliminary, future developments will include a simplified user interface and extended applications, making the tool increasingly suitable for large-scale environmental monitoring activities.

The specific implementation of this workflow varies considerably depending on the application domain and the type of information to be extracted. The two research topics I addressed demonstrate a significant affinity, sharing

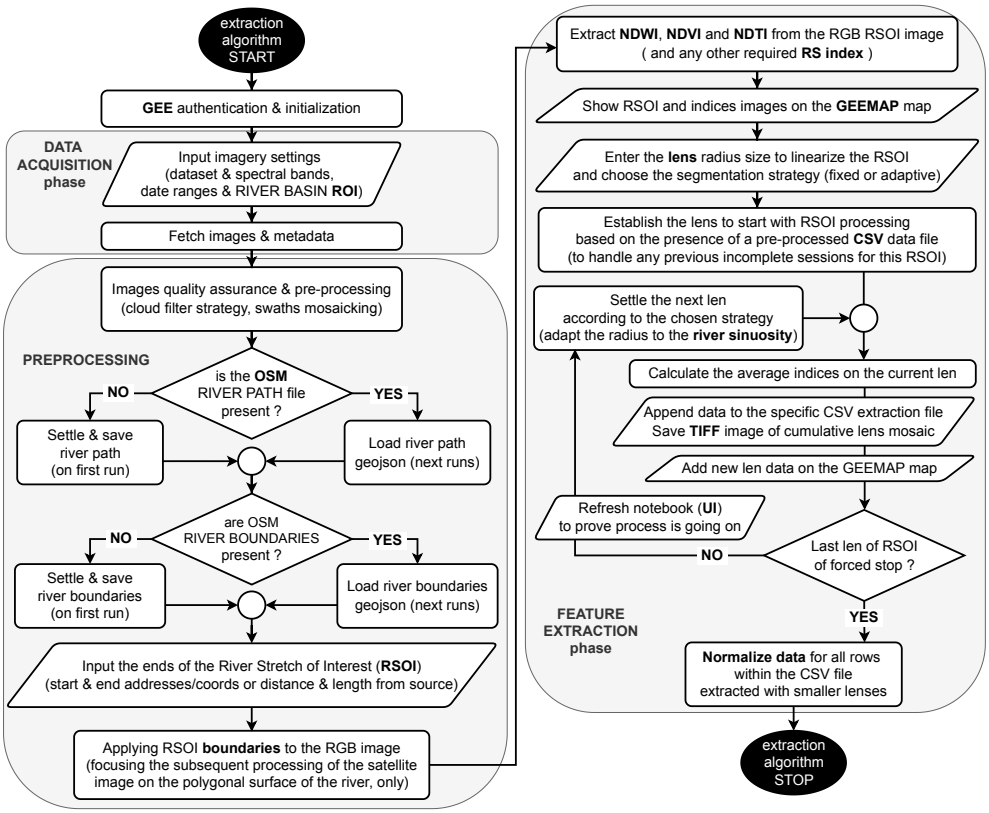

Figure 4.4: Flowchart of the **pipeline** applied to the river use case, leading to the implementation of the custom **RS index extraction algorithm for river waters**, developed in Python, comprising the classic steps: acquisition, i.e. retrieval of raw images covering the river basin area (ROI). The corresponding quality control with the preprocessing phase, focusing on the specific polygonal surface covered by the river (RSOI). And the actual extraction, that is the calculation of the indices in the RSOI area, followed by linearization of the river's meandering path and its subdivision into 500-meter-long stretches using observation lenses optimized as explained in the text. The average indices are then computed from the polygons obtained by intersecting the lenses with the riverbed and saved in tabular format.

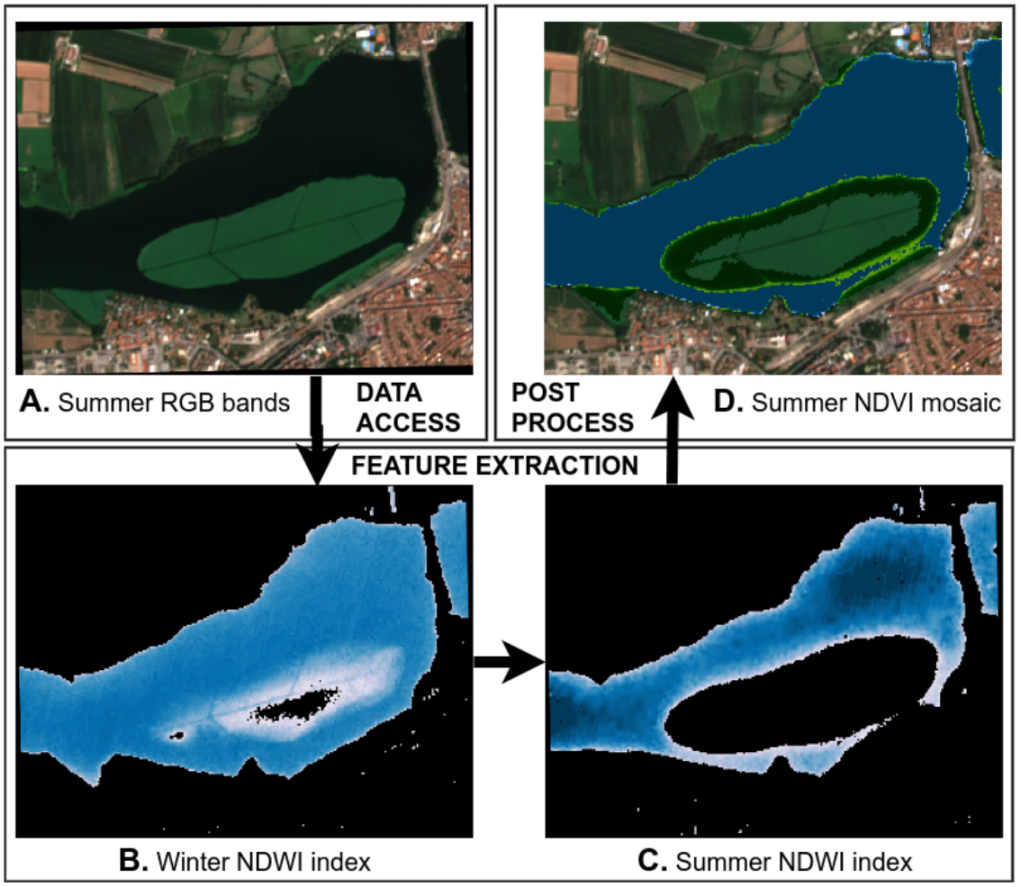

Figure 4.5: An application of the workflow for the lake use case: the processing steps and a result.

many of the points covered in the pipeline. In the following explanation, I will highlight the steps where the lake and river required different processing.

4.2.1 Data Acquisition Phase

This chapter describes data access, corroborated by Figure 4.6, which highlights the three fundamental aspects of an effective integrated analysis. The images to be processed are contained within so-called satellite datasets, which comprise a large number of images acquired over decades of observations. Through their orbital coverage, these datasets span vast portions of the Earth's surface, often encompassing the entire planet, as schematically represented in the figure. Exploring such data to identify the most relevant images (sometimes only hundreds or even a few dozen are sufficient) is crucial, as it allows subsequent processing efforts to focus exclusively on what is strictly necessary, thereby optimizing platform resources while minimizing both processing time and potential costs.

These datasets are highly diverse, and selecting the most appropriate ones for a specific research study requires an initial analysis of the metadata that describes their spatial, temporal, and spectral characteristics. Access to this metadata is typically enabled through queries executed via specific APIs provided by the remote sensing platforms themselves.

The temporal availability of a dataset depends on the satellite's operational period and its orbital path, which determine the frequency with which it revisits a given location—a critical factor known as the Revisit Interval (RI). This interval is also influenced by the extent and positioning of the ubiquitous overlap areas. Typically spanning a few days, the Revisit Interval varies according to the region under investigation and is further conditioned by the collective functioning of satellite constellations, which makes its determination

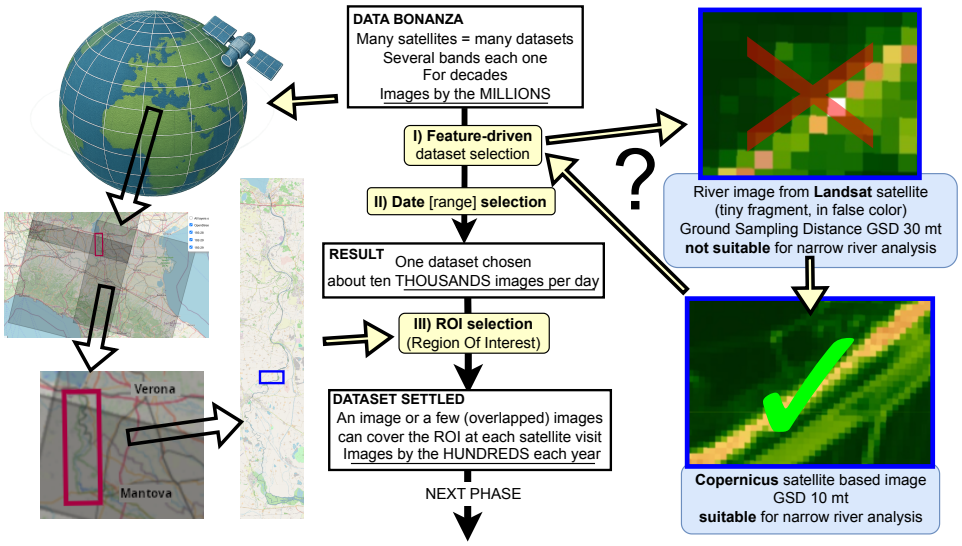

Figure 4.6: Schematic illustration of the data acquisition phase: three main aspects that the selected dataset must address to meet project requirements. The most common constraints comprise spatial, temporal, and other specific qualitative characteristics, which, in turn, lead to a significant reduction in the number of identified images, sufficient to allow for sustainable processing. The river research requires a more precise spatial definition, while the lake research could benefit from a dataset with greater temporal coverage. The pseudo code for the data acquisition phase is illustrated in Algorithm 2.

complex. To be suitable, a dataset must necessarily align with the required temporal span—ranging from decades in the case of long-term trend analysis to just a few selected days for the study of specific one-time events.

These datasets are defined as multispectral since they contain multiple measurement bands that correspond to different frequency ranges of the electromagnetic spectrum detected by onboard sensors. For instance, the widely used MultiSpectral Harmonized Sentinel-2 dataset includes 26 bands, each individually accessible but also readily exploitable in combination, typically for the calculation of composite indices, as they are already harmonized with specific spatial resolutions.

Algorithm 2 Data acquisition step III, as mentioned in Figure 4.6, involves extracting a single image of the studied ROI for the selected month.

// — **DATE SELECTION** —
dateList ← LoadPrecomputedMonthlyDates()
  // List of representative acquisition dates for each month of the selected year
desiredMonthIndex ← 1
  // Example: January
selectedDate ← GetDateFromList(*dateList*, *desiredMonthIndex*)
endDate ← AddDays(*selectedDate*, 1)
  // Define the end of the temporal window (exclusive)
ConfigureTemporalFilter(*selectedDate*, *endDate*)
  // Restrict the dataset to images acquired on the selected date
ConfigureSorting(criteria = AcquisitionDate)
  // Sort images so the closest acquisition appears first
// — **REGION OF INTEREST SELECTION** —
ROI ← RetrievePolygonRegion("Mincio River Corridor")
  // Polygon surrounding the study area along the Mincio river
ApplySpatialClipping(*ROI*)
  // Limit the analysis to the specified geographic region
// — **IMAGE COLLECTION RETRIEVAL** —
useSentinel ← TRUE
  // Select the satellite mission to be used
if *useSentinel* **then**
    datasetName ← `Sentinel-2_SR_Harmonized`
else
    datasetName ← `Landsat_8_TOA`
end if
imageCollection ← FetchSatelliteImages(*datasetName*)
  // Retrieve images satisfying the temporal and spatial constraints
numImages ← GetCollectionSize(*imageCollection*)
DisplayMessage(*numImages*, "images retrieved from the dataset")
if *numImages* = 0 **then**
    DisplayWarning("No images available for the selected date")
    TerminateProcedure()
end if
// — **IMAGE SELECTION OR MOSAICKING** —
imageSeason ← GetFirstImage(*imageCollection*)
  // Use the first image when only one acquisition is available
if *numImages* > 1 **then**
    DisplayMessage("Multiple images detected; performing mosaicking")
    imageSeason ← MosaicImages(*imageCollection*)
    // Merge overlapping satellite tiles into a single image
end if
return *imageSeason*
  // Single satellite image covering the region of interest

Each pixel—the atomic element of a raster image grid—represents a square area of the Earth's surface, with a Ground Sampling Distance (GSD) ranging from 10 to 500 meters, significantly influencing potential applications. In some cases, it suffices to verify that the collection of images covers the entire geographical area of interest, such as an administrative region. However, certain investigations can be much more sophisticated—for example, tracking a complex polygon delineating a river course, as in my study. In such cases, particular care must be taken to ensure that the spatial resolution of the images, determined by the sensitivity of the measuring instrument, is adequate to produce the desired conclusions. The figure refers to the two satellites considered in this study. Only one dataset was deemed suitable: that provided by the Copernicus mission, which offers a resolution fine enough to follow even a narrow river, such as the one under observation. The lake study, on the other hand, does not require such a detailed GSD; therefore, in this case, the Landsat dataset proves adequate and could be preferred due to its greater temporal coverage, which extends back a few decades.

The data acquisition phase defines potentially suitable datasets and identifies useful image subsets within them. Once an appropriate image is identified, it is typically subjected to a cropping operation to precisely match the Region of Interest (ROI), outlined in red in the illustrative figure (bottom left), which encompasses the area crossed by the river under study. The actual ROI analyzed in the river study is reported in Figure 4.30, whereas the ROI for the lake is shown in Figure 4.1.

4.2.2 Preprocessing Phase

The pre-processing phase ensures the quality of the dataset selected for the spatio-temporal window of the study. This involves verifying that the

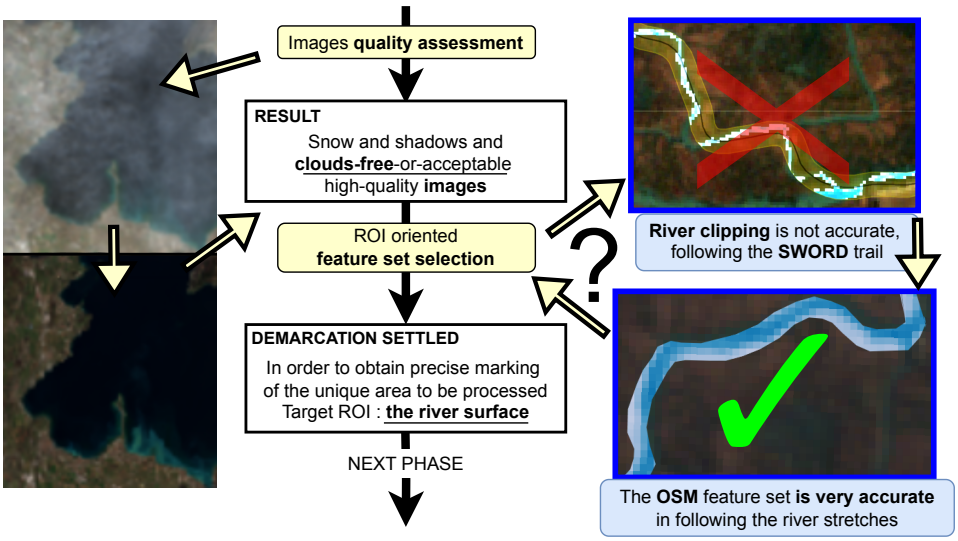

Figure 4.7: A representation of the Preprocessing Phase: two elements that are particularly critical for the study described here are highlighted, with examples for the ROIs of the lake and the river.

satellite-derived images meet acceptable quality standards and discarding, correcting, or supplementing them as necessary. Cloud cover, indicated by specific metadata, represents a common issue and affects multiple spectral bands in both the visible and non-visible spectra. Its management deserves particular attention here, as it is virtually unavoidable. When large image sets are available, only those acquired on cloud-free days may be retained. If the number of usable images proves to be insufficient, images from different datasets with compatible bands can be combined. Images that are only partially clouded can be processed using filtering techniques to reconstruct the compromised areas.

In some datasets, metadata indicating cloud intensity provides only an average value for the entire image, making it difficult to determine whether the image should be retained or discarded. A more effective approach is available

when a dataset includes (either internally or through auxiliary datasets) a dedicated cloud mask band, offering per-pixel or cluster-based measurements of cloud intensity. For instance, in the "QA60" band of the previously mentioned dataset, cloud coverage is recorded at a resolution of 60 meters, meaning that each cloud cover value represents an average over a 6×6 pixel region of a spectral band with a 10-meter resolution. Such dedicated cloud bands enable precise calculations of cloud coverage over specific regions of interest (ROI), allowing for more accurate decisions regarding data retention. This is particularly relevant since satellite imagery typically covers very large areas; for example, Copernicus mission satellites capture images of approximately 110 km on each side, as shown in Figure 4.8a. Use cases focused on short river stretches or small lakes, such as in this study, involve ROIs that are two orders of magnitude smaller. When the ratio between areas is so disproportionate, local cloud intensity should be evaluated to select the most suitable images for the desired time window, as it may differ significantly from the average of the entire image, as illustrated in the examples shown in Figure 4.8.

Beyond increasing with image size, cloud distribution within a single image may vary considerably due to territorial factors—for instance, the presence of high mountains in only part of the image—or due to climatic conditions. In this regard, Figure 4.9 presents a comparison between the cloud footprint of two very different areas: the river section analyzed here in Mantua and the city of London.

These RS studies derive data by analyzing the waters of small lakes and rivers. To extract the required indices, it was necessary to limit the calculations precisely to the portions of the water bodies represented in the satellite images. For such a specific use case, dedicated datasets were employed. These datasets have a different nature. Unlike satellite imagery, they do not

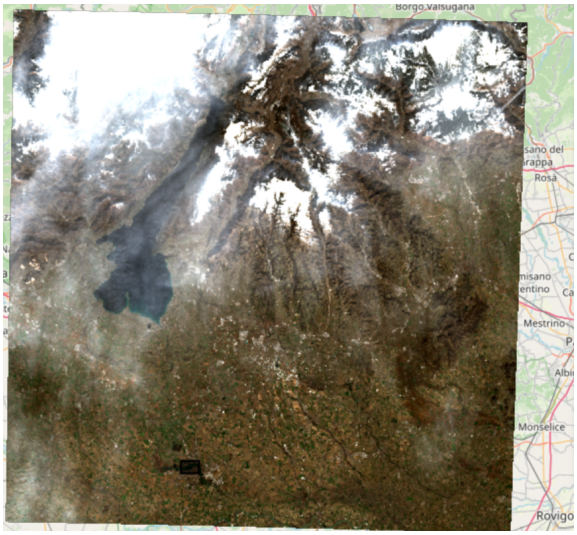

(a) A full image with a tiny ROI

(b) The small Mantuan ROI

Figure 4.8: Clouds considerations. a) The full image Copernicus shot on 13-02-2019. Overall cloud intensity at 70%. Despite this, the ROI is clear, the small, barely perceptible black box. b) On the contrary, on 04-03-2020, a slightly cloudy day (20% overall), the lake in the ROI area is quite noisy.

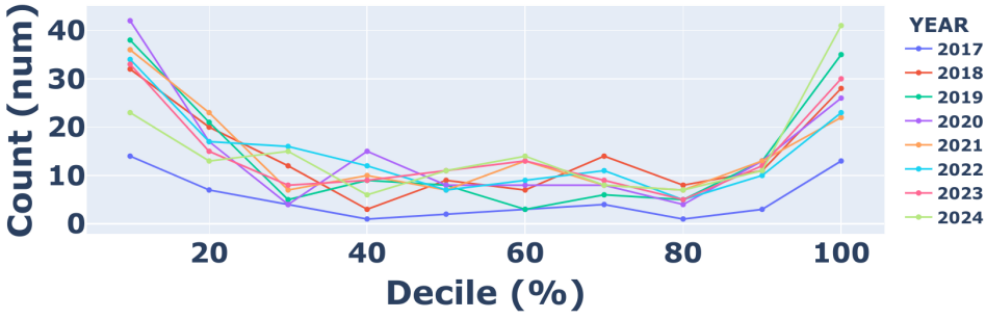

(a) Annual distribution of cloudy days, for the small Mantua ROI. Clear days (on the left of the graph) are the majority

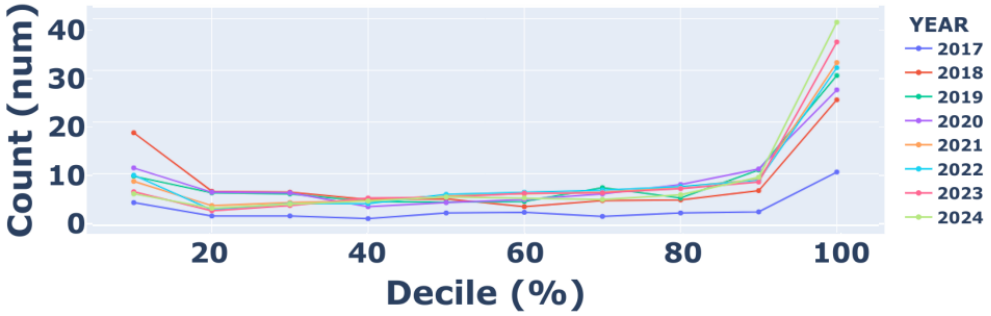

(b) Cloudy days distribution, in London

Figure 4.9: Cloud cover comparison - Most images of Mantua are processable. Much more challenging weather conditions characterize the London area.

Figure 4.10: Lake Superiore of Mantua represented by the SWORD vector dataset, one of the so-called Feature Collections available in the GEE platform. Nodes are depicted with red circles, reaches are the blue segments.

contain raster images; instead, they provide extensive vector datasets in which the data are linked to geographic polygons, such as administrative regions, physical areas (e.g., watersheds, ecoregions), or artificial structures. These vector datasets, known as **Feature Collections** in Google Earth Engine jargon, are intended to be used in conjunction with raster data. They cover a wide range of topics, from ecological footprints to the locations of dams and socio-economic information, serving as a fundamental resource for the extraction of georeferenced features. For instance, the Surface Water and Ocean Topography (SWOT) database, and in particular one of its derivations, the SWOT River Database (SWORD), was initially considered.

SWORD helped to define the lake surface as needed for this study, thanks to the fact that, for each node (illustrated in Figure 4.10), this dataset reports the approximate width of the lake at that point. The precise profile of the body of water required further masking using the NDWI index, as shown in figure 4.11b, when the water reclaims all its space in winter.

(a) Summer true color view (RGB bands).

(b) NDWI index calculated in Winter.

Figure 4.11: Lake Superior of Mantua, according to Copernicus's images. NDWI is crucial for delineating the exact extent of the lake.

However, SWORD proved too imprecise in following the winding course of the river. For that task, the study relied on the more widely used OpenStreetMap (OSM) database, even though it is not directly integrated into the satellite platform employed, Google Earth Engine (GEE). As can be seen from the comparison between these two cartographic datasets in figure 4.7.

While the pre-processing phase is designed to improve the quality of images identified during data acquisition, it can drastically reduce the dataset size to unacceptable levels, especially when strict cloud intensity thresholds are applied. Following this phase, a temporal summary of the remaining available images is useful for assessing whether it is advisable to consider an alternative dataset.

4.2.3 Feature Extraction Phase

Once sufficient high-quality data has been acquired, the Feature Extraction phase begins, transforming raw data into meaningful and relevant information through a variety of operations. In addition to using the native bands of the dataset, customized extractions can be performed by combining bands through tailored formulas. Hundreds of such indices are described in the literature (e.g., [83]), and new ones are continuously being explored, reflecting the ingenuity of researchers. During the Feature Extraction phase, the most effective index to achieve the research objective is determined, as different domains require different approaches. Water-related indices are particularly numerous and widely used. In the lake study, the most popular indices—the Normalized Difference Water Index (NDWI) and the Normalized Difference Vegetation Index (NDVI)—were computed due to their efficacy in detecting plants growing in water bodies. For the river topic, great emphasis was placed on a gregarious index, the Normalized Difference Turbidity Index (NDTI),

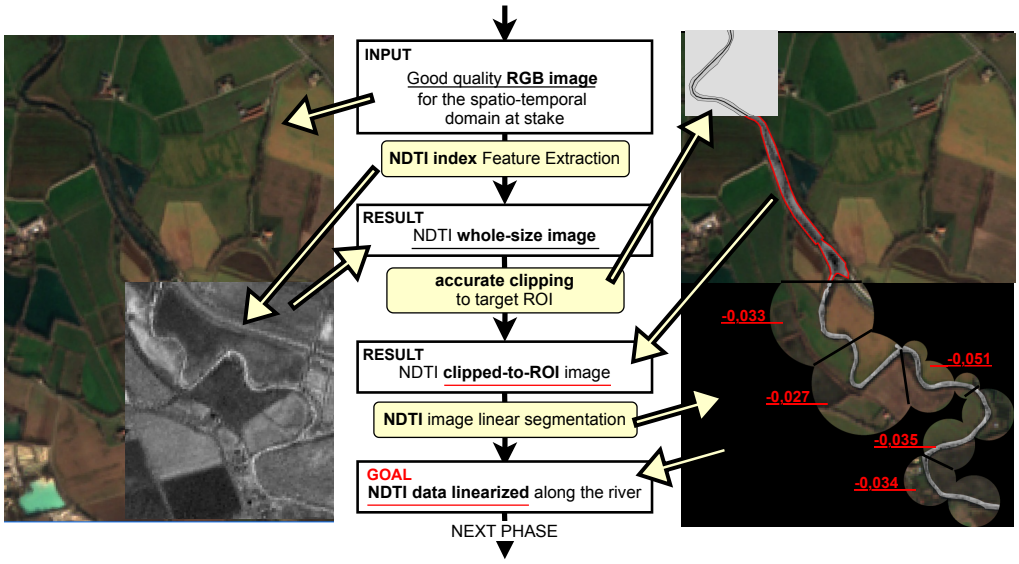

Figure 4.12: Schematic drawing of the Feature Extraction Phase for the river research topic: the steps to transform high-quality raster images into relevant, standardized information. Data from the smaller lenses (in the image on the right) are normalized before being returned.

which is particularly suitable for estimating the concentration of silt and other suspended particles in water bodies. These particles are often linked to anthropogenic activities, making the index highly relevant for water quality monitoring. It exploits the red and near-infrared satellite spectral bands.

At this point, the pipelines of the two case studies begin to diverge significantly. First, we describe how the data extraction phase was applied to the river. The lake will be discussed immediately afterward.

Feature Extraction for the river use case

Figure 4.12 illustrates the steps carried out in the Feature Extraction phase for the river use case. First, an index image is generated from the RGB pixels of the satellite data, as shown on the left side of the figure, where the NDTI index

values are displayed in grayscale for a portion of the image. Subsequently, spatio-temporal reductions are applied—such as the computation of mean values—enabling comparisons across different areas or time intervals, thereby facilitating the identification of trends, anomalies, or extreme values in the subsequent post-processing phase (described in the following section). For example, it was possible to identify locations within the river where turbidity showed maximum variation and to correlate these with tributary inflows, discharges, or nearby settlements. Achieving this objective required addressing and overcoming two main challenges.

The first challenge was isolating only the river pixels within the full image to avoid incorporating unwanted contributions (typically from soil) into the mean NDTI values. To address this, the vector profile of the river, obtained from the previously mentioned OSM vector database, was employed. Using Google Earth Engine (GEE) functions, the set of GPS coordinates was converted into a polygon, which was then applied as a clipping mask to the NDTI image. In the upper-right section of Figure 4.12, the river profile is displayed for a short stretch within a small gray inset. The river course is then traced in red on the full-color satellite image, with the interior overlaid in grayscale, representing the NDTI values. This integration of multiple information layers within the same image is referred to as mosaicking. The intermediate result is a clipped NDTI image, consisting of a grid of gray pixels corresponding to the river and black pixels for the background.

The second challenge was transforming the pixels of the clipped NDTI image into a linear set of numerical values representing the mean NDTI at the desired scale, effectively producing a tabular dataset. To achieve this, the river profile was linearized along its vector path, which was extracted from the OSM dataset again. The task then was to partition this “unrolled” river

into segments of a chosen length, typically 500 m. This was accomplished by defining a sequence of contiguous and nearly tangent circles, with each center placed along the river path at the specified distance from the previous one. As a result, the straight-line distance between circle centers does not necessarily match the segmentation step; in fact, it tends to be shorter in highly sinuous stretches. This is clearly illustrated in the lower-right portion of the figure. 4.12, where five newly calculated NDTI values are also highlighted in red. The river profile was thus segmented using these consecutive circles as clipping masks, and for each intersected area, the mean NDTI values were computed and stored in a table. The river's course and the two river margins on either side required to complete this task are derived from the OSM database and are shown in an inset within Figure 4.30 at the confluence of a major tributary. Another demonstration of the segmentation task is provided in Figure 4.13, which allows for the assessment of turbidity and other RF indices relevant to the present study.

The circular shape was chosen for the segmentation task because of its adirectional nature, which made it possible to disregard flow direction. It is as if the circles were lenses through which to observe the river course. While not a perfect solution, it provides a robust approximation for linearizing the inherently irregular two-dimensional river profile. A limitation arises in narrow bends, where circles tend to overlap; the same occurs for the relative calculation areas. The algorithm mitigates this by adaptively reducing circle radii—by one-half or one-quarter of the predefined size—thus lowering overlap. However, this adjustment is applied cautiously, as the GEE processing time per circle (on the order of 1–2 minutes) is unaffected by the size of the circle. Because minimizing execution time is an obvious design objective, the number of circles must be kept as low as possible. On average, the overlap

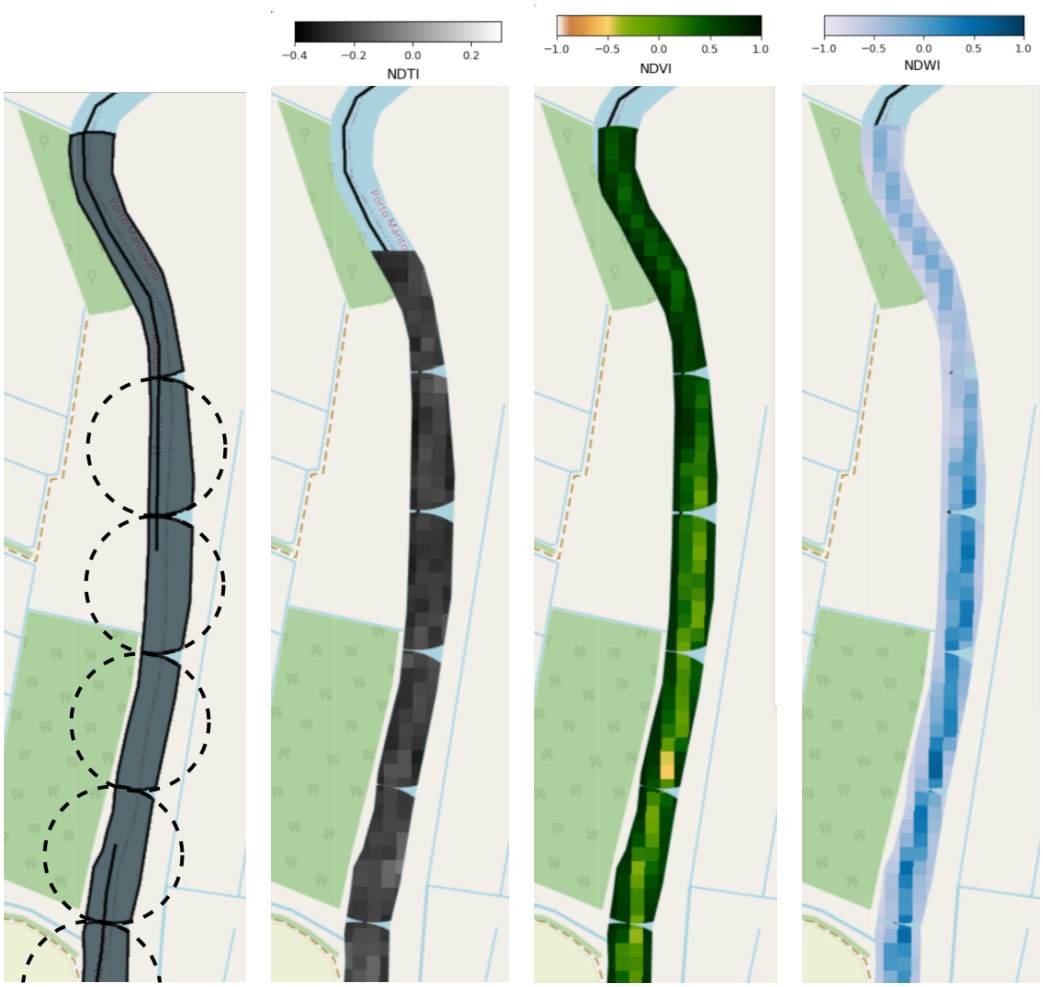

(a) Five hot dogs (b) NDTI areas (c) NDVI areas (d) NDWI areas

Figure 4.13: To tackle the river segmentation task, the designed algorithm cuts out circular lenses along the river's course. The remote sensing indices are averaged across the resulting small surfaces, which resemble hot dogs. This study uses turbidity, vegetation, and water indices to assess the fundamental aspects that characterize a river.

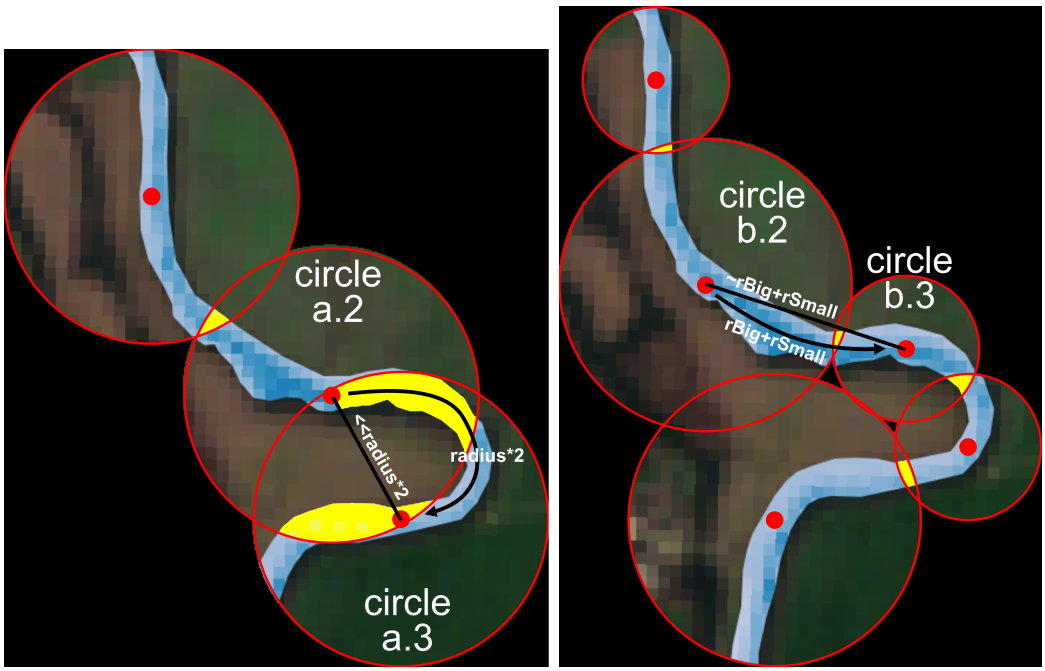

(a) Fixed radius mode (250 mt). The distances of the centers, along the river and in a straight line, are very different.

(b) Adaptive (250 and 125 mt). The distances of the centers, along the river and in a straight line, are quite similar.

Figure 4.14: Reduction of defects (overlapping yellow areas) by using observation lenses that adapt to the sinuosity of the river, in a narrow bend of Mincio. The pixels of the river surface show NDWI values, in shades of blue.

between consecutive processing areas produced by the adaptive radii strategy is about 2%, though it may occasionally reach 20%. A worst case example for the fixed-radius mode is reported in Figure 4.14. Such an unacceptable situation is due to that very winding stretch, as revealed by the markedly short straight-line distance between the centers of circles a.2 and a.3. Even though the adaptive strategy performs better between circles b.2 and b.3, the author has already proposed a more advanced algorithm designed to eliminate overlaps. Nonetheless, a key advantage of the present approach is the complete coverage of the river surface. Before returning the mean NDTI values for each river segment, the algorithm applies a normalization step to account for cases in which reduced-radius circles were employed, as shown in Figure 4.14b. This radius reduction (by factors of 2 or 4) facilitates the proper alignment of the output data.

The outcome of the Feature Extraction for the river use case is a structured table reporting the mean values of NDTI, NDWI, and NDVI—along with the possibility of incorporating additional indices—and other relevant statistical descriptors, all prepared for subsequent processing and visualization, including graphical outputs. Each record also integrates algorithm-specific parameters along with detailed georeferenced information, such as progressive distances, circle centers, tangent locations, and the complete profile of each computed surface. The example in 4.15 refers to the confluence with a tributary. This comprehensive data structure ensures full traceability and reproducibility of the analytical workflow, thereby enabling a robust reconstruction of the operations performed on the images of the river.

distance	tributaries	meanTI	deltaTI	meanVI	meanWI	xCenter	yCenter	intra centers	area	overlap	%
125		-0,284		0,717	-0,563	10,691356	45,202981	distance	9.677		
375		-0,255	0,029	0,646	-0,489	10,690124	45,201445	196	7.342	818	11,1%
625	GOLDONE	-0,212	0,043	0,376	-0,211	10,690453	45,199257	245	7.523	46	0,6%
875		-0,186	0,026	0,329	-0,186	10,689975	45,197036	250	7.544	4	0,0%
1.125		-0,161	0,024	0,256	-0,122	10,689235	45,194856	249	9.054	8	0,1%
1.375		-0,218	-0,057	0,462	-0,289	10,688488	45,192670	250	9.255	0	0,0%
1.625		-0,197	0,021	0,459	-0,308	10,688706	45,190453	247	8.943	59	0,7%
1.875		-0,205	-0,008	0,456	-0,311	10,689536	45,188282	250	9.568	1	0,0%
2.125		-0,185	0,020	0,274	-0,123	10,689743	45,186049	249	8.272	22	0,3%
2.375		-0,212	-0,028	0,474	-0,327	10,688298	45,184375	218	6.768	235	3,5%
2.625		-0,212	0,001	0,408	-0,239	10,685471	45,183350	250	7.051	15	0,2%
2.875		-0,225	-0,013	0,381	-0,208	10,683498	45,181622	247	7.568	29	0,4%

Figure 4.15: The results of the extraction on a short stretch of the river. For each area, the NDTI, NDVI and NDWI indices are reported as averages and shown with conditional gradient formatting to highlight their clear correlation. The values in the deltaTI column highlight the significant change in water at the point of confluence with a dense drainage channel.

Feature Extraction for the lake use case

Figure 4.16 illustrates the steps carried out in the Feature Extraction phase for the lake use case. First, an index image is acquired from the RGB pixels of the satellite data, corresponding to the area approximately identified with the SWORD dataset for Lake Superior in Mantua. The figure refers to the month of January, characterized by almost no vegetation cover. The NDWI index, which represents the portion with the greatest water coverage throughout the year, is extracted from the image. A thresholding operation on the index then produces a binary mask that is considered to be the profile of Lake Superior. This surface area is used as the baseline for subsequent processing during the Feature Extraction phase. Typically, this is to observe the dynamics of the expansion over time of the plant island located in the center of the lake, which has a minimum in Winter and a maximum in Summer. They are clearly visible by comparing the NDWI index images for January and August, both of which are shown in the figure. The NDVI index reinforces the island profile,

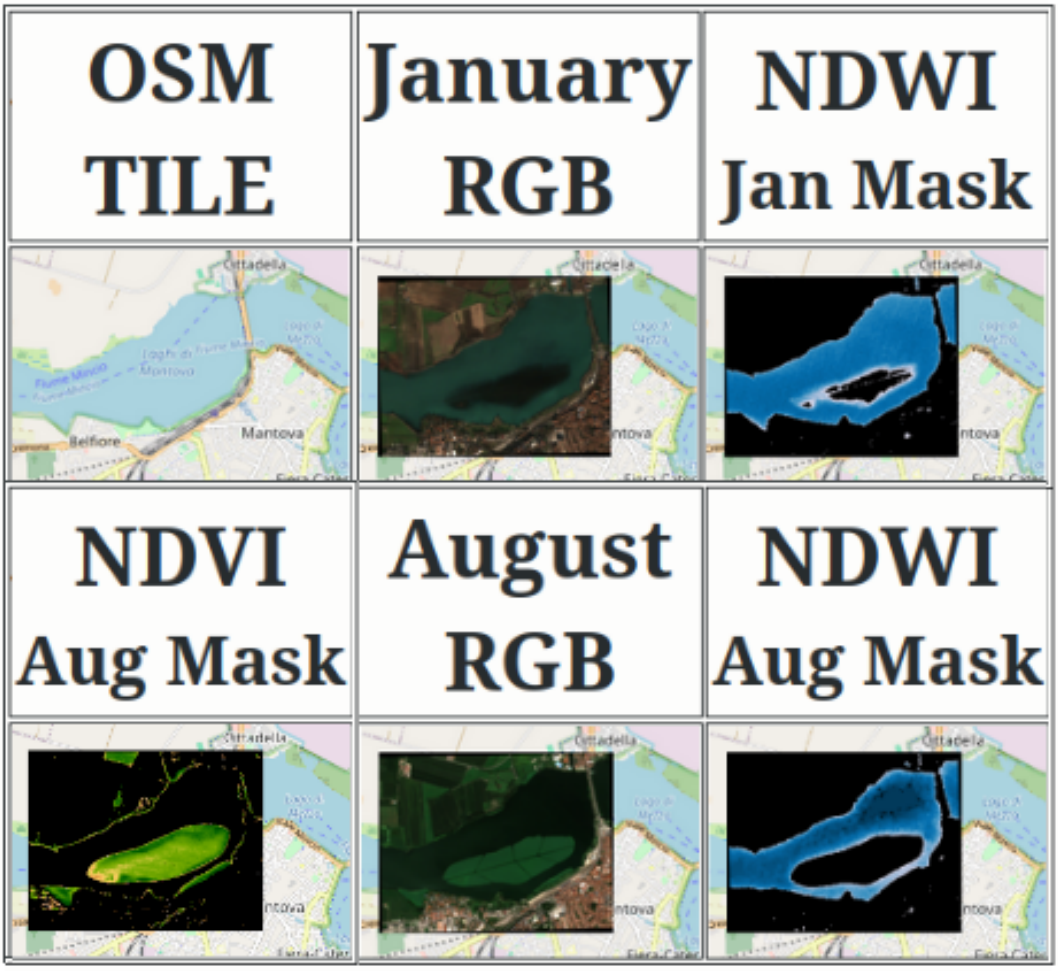

Figure 4.16: Highlights of the feature extraction phase applied to the lake research topic: the steps aimed to transform high-quality raster images into relevant and standardized information, using two classic RS indices in a combined way, NDVI and NDWI.

yr/mth	1	2	3	4	5	6	7	8	9	10	11	12	AVG
2017					11	25	41	39	42	19	38	2	27
2018	4	0	3	12	23	36	39	34	34	23	1	5	18
2019	2	1	0	21	35	23	22	37	31	27	31	9	20
2020	1	2	6	8	34	26	33	35	36	14	11	2	17
2021	7	1	2	15	47	29	25	40	39	37	33	0	23
2022	13	0	0	2	26	28	30	34	34	9	33	0	17
2023	4	5	4	11	51	42	33	39	41	31	38	16	26
2024	3	10	3	17	26	7	27	39	44	21	28	19	20
AVG	3	1	3	14	30	28	32	37	36	21	20	4	20

Figure 4.17: A result of the feature extraction phase on a small lake similar to the lakes of Mantua, thanks to the Copernicus images. The extents are expressed in hectares. The analysis can be extended further back in time using images from the thorough Landsat mission, since these calculations do not require high resolution.

as it complements the observations obtained with the NDWI index. In fact, in the area where the former is bright green, the latter is black. Conversely, blue areas of the NDWI index appear black in the NDVI. By appropriately identifying the filter thresholds to apply to the images calculated from the two indices, the resulting masks fit almost perfectly, allowing us to establish the island's extent with greater confidence. Figure 4.17 shows the results obtained for a similar lake, Fimon, in the Vicenza area.

4.2.4 Post-processing Phase

In the post-processing phase, the results are refined, integrated, and subjected to comparative analysis, thereby adding interpretive value and transforming raw outputs into actionable information. Typically, the generated maps are enriched with study-specific datasets. A representative example is the analysis of areas impacted by flooding: municipal authorities may overlay

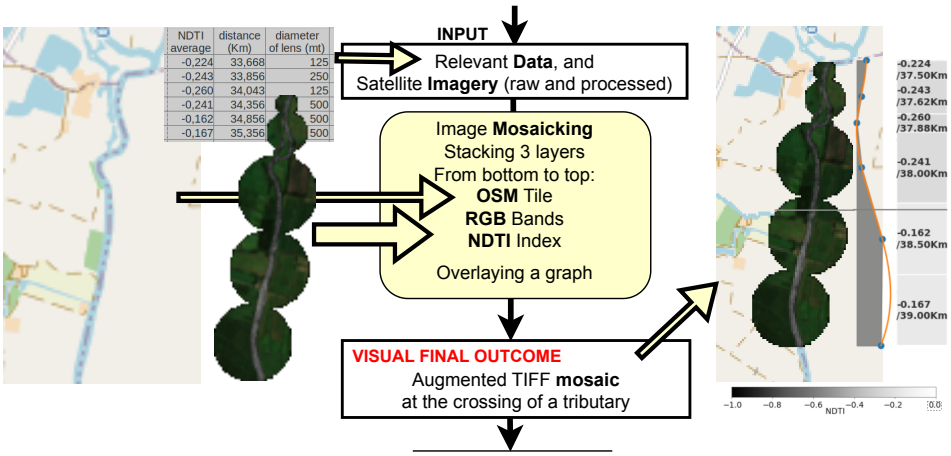

Figure 4.18: The Post Processing Phase: how to integrate diversified data to obtain a meaningful georeferenced result.

architectural and cadastral datasets to estimate potential damages, while the integration of topographic attributes (e.g., road width and slope) can support Civil Protection agencies in planning evacuation routes and ensuring access for emergency vehicles.

The overlay of raster and vector data on a single map provides immediate visual validation of results and may reveal issues not evident in earlier processing stages, such as false positives. Figure 4.18 illustrates an example developed in this study, showing the investigated river at its confluence with a tributary that carries turbid waters. The impact on turbidity is substantial. The resulting composite image integrates all data sources, displaying them in a contextualized framework to facilitate comprehensive interpretation.

Graphical representations further enable comparisons across information layers, temporal frames, spatial locations, or scales. Animations and plots often provide the most effective visualization of results, as illustrated in the following section. While certain satellite platforms incorporate such tools

natively, researchers often rely on external software solutions to obtain these results.

An effective framework for managing the described remote sensing workflow should also include a user interface, enabling users to define the spatial extent of the study area, the temporal range, desired quality thresholds, and output specifications through a dedicated control panel.

4.3 Experimental Evaluation

This section of the thesis reports the results of data observations derived from satellite imagery. The research required the development of a considerable amount of processing code and its execution over a significant number of hours on the selected cloud platform chosen to carry out the work. The technological aspects addressed constitute an important part of the overall effort. Subsequently, particular attention was devoted to rendering the extracted information in graphical form or by combining maps and charts to facilitate a better understanding of the results. The findings are primarily empirical in nature; the observations call for further elaboration and will be validated in subsequent studies.

The research activities are based on Google Earth Engine (GEE), a planetary-scale platform for Earth science data and analysis that combines a multi-petabyte catalog of satellite images and geospatial datasets with extensive large-scale analytical capabilities. GEE was also chosen because it offers a free, unlimited-use license for researchers. This tool has been fully proven to be fit for its purpose. The analyzes are conducted through scripts written in the Python programming language. The rich GEE API can be

efficiently accessed within Jupyter Notebook documents using the geemap [2], a recently developed package designed for interactive geospatial analysis and visualization with Google Earth Engine, allowing comprehensive access to all GEE functionalities. For graphical rendering, the matplotlib [3] library was employed, which required the implementation of a dedicated set of Python routines.

4.3.1 Datasets

The GEE platform provides access to thousands of datasets, each containing tens of thousands of terrestrial images acquired by satellite sensors that have been orbiting the planet for decades. The dataset lists can be consulted through the Earth Engine Data Catalog [4], the publicly available official repository, along with those included in other open-source catalogs published online by expert communities, [5]. Following the Pipeline described previously (to which reference is made for explanatory diagrams), the catalogs were preliminarily examined in search of datasets covering the studied area and ensuring the quality required for their specific processing needs.

Two raster datasets were thus identified (containing images of the Po Valley captured by satellite, whether raw or pre-processed), provided by the U.S. Landsat and European Copernicus (Sentinel satellites) missions, selected for their extensive coverage, relevance, and continued operational status. They are widely used because they cover the entire globe, except for the polar regions in the case of Copernicus. Containing dozens of bands in the visible spectrum and beyond, they are well-suited for calculating remote

[2]Geemap Python Library for GEE: `https://geemap.org/`

[3]Matplotlib, Visualization with Python: `https://matplotlib.org/`

[4]GEE Data Catalog: `https://developers.google.com/earth-engine/datasets`

[5]GEE Community Catalog: `https://gee-community-catalog.org/`

sensing indices, including the previously mentioned NDVI, NDWI, and NDTI. While somewhat alternative, the "USGS Landsat 8 Collection 2 Tier 1 TOA Reflectance" dataset, operational since 2013, was set aside in favor of the "Harmonized Sentinel-2 MSI: MultiSpectral Instrument, Level-2A" dataset, operational since 2017. If needed, these satellite missions also provide older imagery, with Landsat extending back to the 1980s. Copernicus imagery is highly detailed, with certain bands reaching a Ground Sample Distance (GSD) of 10 meters per pixel—compared to Landsat's 30 meters—an essential feature for the detailed analysis of a narrow river such as the Mincio. As already mentioned, providing an exact estimate of the Revisit Interval (RI) of these satellites is misleading; however, it can be stated that Landsat revisits the river approximately 50 times per year, with an RI of about 8 days, whereas Copernicus does so more frequently—approximately 150 times per year, every 2–3 days. This allows for a broader selection of cloud-free images.

To focus the analysis on the river stretch of interest, vector datasets were also employed, containing the objects to be observed and georeferenced to allow for their accurate identification within the imagery. For this case study, datasets containing traces of freshwater rivers were sought. Initially, the SWOT River Database (SWORD) [6], a river-specific version of the more widely known SWOT dataset, was considered, as its integration into the GEE platform seemed to provide a natural solution. It was helpful in identifying the surface of the lake under observation, even if it was approximate, to such an extent that further passage was required. However, when tested in the river study, it proved highly approximate in tracing the course of the Mincio, as demonstrated in Figure 4.7. The second candidate, the

[6]SWOT River DB: `https://gee-community-catalog.org/projects/sword/`

widely used OpenStreetMap (OSM) database [7], was therefore selected, as it contains a precise vector description of the river, including its meanders. It provides both the riverbank vectors—necessary to delimit the surface for NDTI calculations—and the river axis, which enables its "linearization" and segmentation (both are shown in 4.30), leading to the calculation of spatial averages. Since it is not accessible through the GEE APIs, it was integrated using the geemap library.

Considering the spatial and temporal characteristics described, a weighted selection of the datasets most suitable for the specific use case was made. In particular, it was necessary to combine multiple datasets, including rasters and vectors, while exploiting the specific strengths of each.

4.3.2 Evaluation Metrics

The lake study focuses on vegetation resources in watercourses and utilizes the two most commonly used remote sensing indices in this field: NDVI and NDWI. These indices are derived by applying mathematical formulas to data contained in the spectral bands of satellite images, producing values within the range $[-1, +1]$.

Specifically, the Normalized Difference Vegetation Index (NDVI) quantifies vegetation health and density using the formula:

$$NDVI = \frac{NIR - Red}{NIR + Red} \tag{4.1}$$

where NIR represents the Near Infrared band. Since healthy vegetation strongly absorbs red light (for photosynthesis) and reflects near-infrared light due to chlorophyll, NDVI provides a measure of vegetation vigor. NDVI

[7] Open Street Map free world map: `https://www.openstreetmap.org/`

values close to +1 indicate dense, healthy vegetation, while values near 0 or negative indicate barren land, water bodies, or urban areas.

The Normalized Difference Water Index (NDWI) is used to identify and monitor water bodies and soil moisture. It is based on the difference between reflectance in the near-infrared (NIR) and green bands, following the formula:

$$NDWI = \frac{Green - NIR}{Green + NIR} \tag{4.2}$$

Positive NDWI values indicate the presence of water, while negative values correspond to land, vegetation, or dry surfaces. Various modified versions of these indices exist, which may be considered in future research to draw more effective conclusions. For instance, in [74], the authors employ the Modified Normalized Difference Water Index (MNDWI), which minimizes signal interference from built-up areas, making it superior for "Water Body Detection" studies in urban contexts.

Turbidity is a measure of the degree to which water loses its transparency due to the presence of suspended particles. It is the physical characteristic on which the study of the river is based. It is commonly used to monitor water quality and assess the health of aquatic ecosystems. The river study employs a classical remote sensing index derived from the spectral bands of satellite imagery, which is widely used for this purpose: the Normalized Difference Turbidity Index (NDTI):

$$NDTI = \frac{Red - Green}{Red + Green} \tag{4.3}$$

As explained in [8], in pure water, the reflectance is weak in the green band (less than 10%) and becomes very low in the red band. As turbidity levels increase due to the growth of suspended particles, red band reflectance exceeds green band reflectance. NDTI exploits this spectral characteristic of turbid water to detect pixels associated with turbidity.

Like any normalized differential index, NDTI is dimensionless and produces values within the interval $[-1, +1]$, where higher values indicate greater turbidity. In this study, the index is computed along the 44-kilometer northern reach of the Mincio River to identify river sections and temporal instances in which turbidity values are extreme. In the remainder of this thesis, NDTI and turbidity will be used interchangeably, given their close correspondence. Additional metrics proposed in this study are described below.

The availability of NDTI values also made it possible to examine their variations along the river course; this study identified roughly ten spots with significant changes in turbidity. To facilitate the understanding of these dynamics, specific definitions are introduced:

- JUMP = an intense change in turbidity experienced by the water between measurement points.
- BASELINE = the turbidity value before the disturbance.
- RECOVERY = the return of turbidity to its pre-disturbance value (its baseline).
- GAP = the percentage of NDTI variation that is not recovered.

To quantify these dynamics, a specific speed metric has been defined:

$$NDTI_s = \frac{\Delta NDTI}{\Delta s} \quad \left[\ \mathrm{km}^{-1}\right] \tag{4.4}$$

where $NDTI_s$ represents the rate of NDTI variation as a function of the spatial distance Δs, in terms of velocity. An example is shown in Figure 4.19.

If high turbidity values indicate poor water quality, then rapid increases in turbidity should reflect more severe disturbances. Conversely, sharp declines in turbidity are expected to signal strong self-purification capacities of the river,

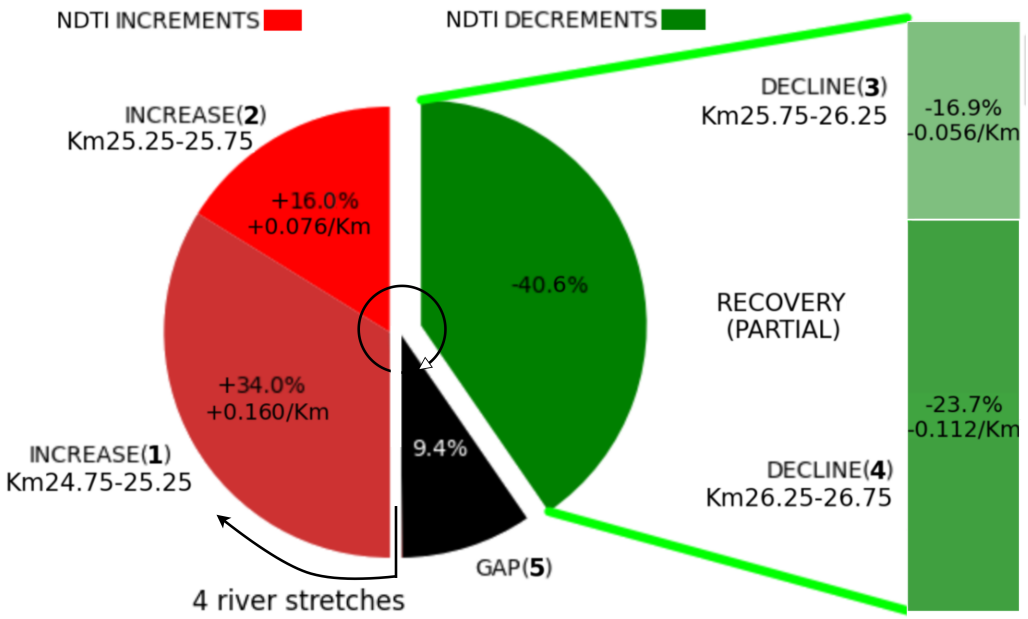

Figure 4.19: An NDTI peak with a partial RECOVERY, as measured in **Corte Merlesco** on 02-02-2024, shown with the specific metrics. Turbidity remained significantly higher than the BASELINE where the perturbation began, as reported by the black GAP(**5**) slice. The 4 measurements range from (**1**) to (**4**) and concern consecutive stretches of the river each 500 metres long, reported clockwise, starting from the bottom. The pie chart shows the progression of the 4 fluctuations (red increments followed by green decrements) along space and their relative magnitude, also in terms of NDTI velocity expressed per kilometer. This NDTI disturbance has been circumscribed with the red balloon in the spatial plot of the entire river in Figure 4.32a.

especially when a jump is fully compensated by recovery. Jumps and their dynamics have been represented through dedicated graphical outputs, allowing for the identification of recoveries, gaps, and variation rates. Interpreting these metrics can guide the investigation of factors influencing turbidity in the river and its fluctuations, whether of natural or anthropogenic origin.

4.3.3 The Lake Use Case

This chapter focuses on the first application scenario addressed by this thesis, which applies the Remote Sensing approach in a lacustrine context.

The Challenge

The challenge of this research is to develop an automated tool that, through the analysis of satellite data, can distinguish areas of water bodies colonized by floating vegetation, determine the profile of these blooms, and quantify their extent over time. The research focused on the plant island that expands in Lake Superior near Mantua with a very constant periodicity over the years, as clarified in figures 4.22 and 4.25. Both NDVI and NDWI, two classic remote sensing indices, can be used to provide the required profile by applying masking operations that use a threshold value to determine whether an image pixel represents water or plants. NDVI provides the profile of the plant island; NDWI provides the profile of the surrounding water. These two figures are complementary. Here, we propose a combined use of the two indices, cross-referencing the profiles so that the results obtained reinforce one another. In practice, by fine-tuning the threshold values of the two indices, we aim to find the combinations that lead to the most compatible profiles. The goal is to develop a recognizer that minimizes conflicting pixels attributed to both categories or to neither. The availability of approximately fifty satellite

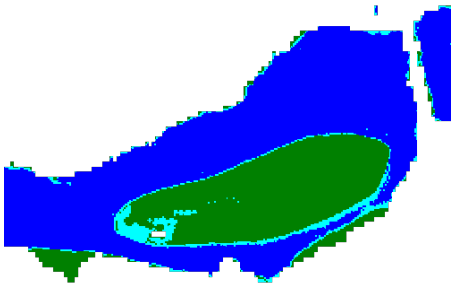

(a) Many unclassified pixel

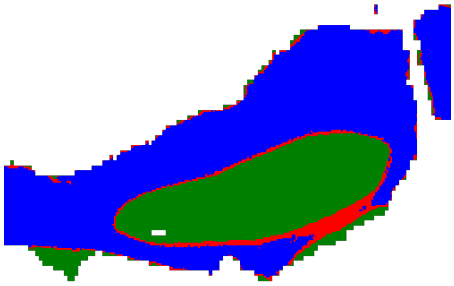

(b) Conflicting attributions

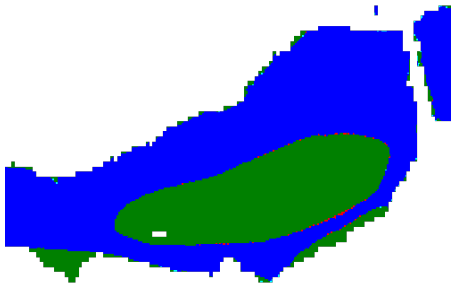

(c) Good segmentation

NDVI \ NDWI	-0,55	-0,5	-0,45	-0,4	-0,35	-0,3	-0,25	-0,2	-0,15	-0,1	-0,05	0	0,05	0,1	0,15	0,2
0,15	(c) 7,78	7,25	6,80	6,46	6,15	5,85	5,56	5,26	4,96	4,59	4,18	3,73	3,28	2,73	2,25	2,06
0,2	6,71	6,18	5,73	5,39	5,08	4,78	4,49	4,20	3,89	3,53	3,13	2,69	2,29	1,87	1,72	2,10
0,25	5,78	5,24	4,80	4,46	4,14	3,85	3,57	3,28	2,98	2,64	2,24	1,83	1,51	1,36	1,70	2,48
0,3	4,96	4,42	3,97	3,63	3,32	3,02	2,75	2,47	2,18	1,85	1,50	1,17	1,08	1,32	2,06	3,08
0,35	4,24	3,71	3,26	2,92	2,62	2,33	2,06	1,79	1,51	1,22	0,94	0,81	1,04	1,63	2,56	3,66
0,4	3,64	3,11	2,66	2,33	2,02	1,76	1,49	1,22	0,98	0,78	0,67	0,83	1,35	2,06	3,04	4,20
0,45	3,07	2,53	2,08	1,76	1,47	1,22	0,97	0,76	0,63	0,62	0,78	1,15	1,77	2,54	3,55	4,75
0,5	2,63	2,09	1,66	1,35	1,06	0,83	0,63	0,56	0,59	0,77	1,07	1,50	2,17	2,95	3,99	5,19
0,55	2,18	1,66	1,25	0,95	0,69	0,53	(d) 0,46	0,56	0,76	1,09	1,48	1,93	2,61	3,40	4,44	5,63
0,6	1,80	1,29	0,90	0,65	0,47	0,44	0,56	0,80	1,08	1,44	1,85	2,31	3,00	3,79	4,83	6,03
0,65	1,38	0,89	0,57	0,43	0,46	0,66	0,90	1,19	1,49	1,87	2,29	2,76	3,44	4,23	5,28	6,47
0,7	0,97	0,56	0,46	0,59	0,83	1,10	1,38	1,68	1,99	2,37	2,79	3,26	3,94	4,73	5,78	6,97
0,75	0,85	0,79	1,07	1,38	1,69	1,98	2,26	(b) 2,56	2,87	3,25	3,67	4,14	4,83	5,62	6,66	7,85

(d) Threshold combinations performance. The table (shown with conditional gradient formatting, green is good, red is bad) reports the percentage of pixels with uncertain attribution between water and vegetation, as a function of the thresholds used for NDWI and NDVI masking. The combinations in the central area produce less uncertain pixels. At the top of the picture there are three significant outcomes, reported in the table with their respective letters.

Figure 4.20: The Aquatic Vegetation vs Water segmentation algorithm uses two thresholds to filter in or out pixels from the two clusters. Unclassified pixels in the three maps are expressed in color. **Cyan**: neither water nor vegetation. **Red**: both water and vegetation.

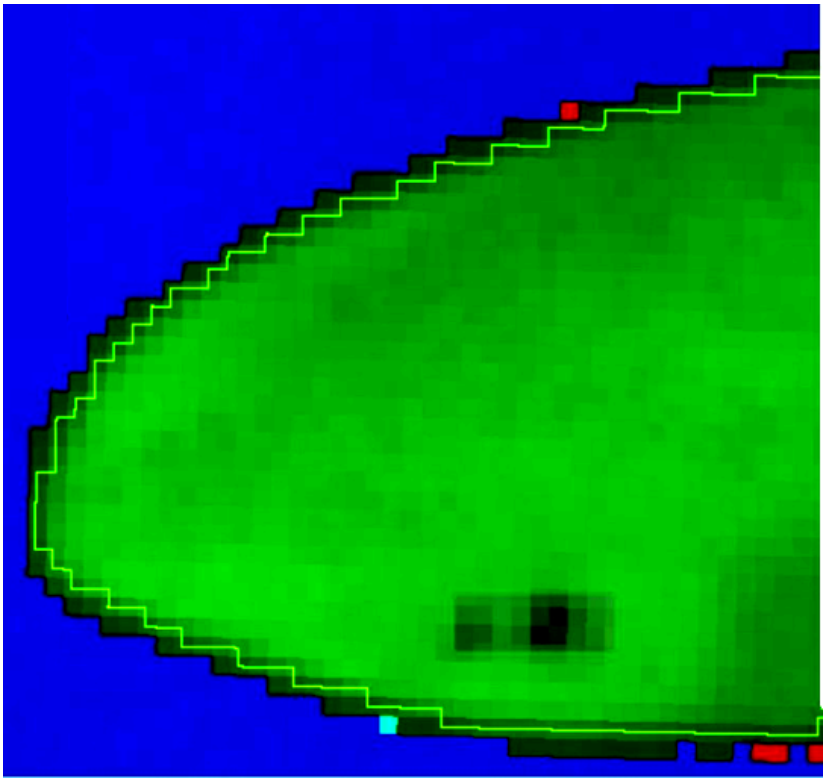

Figure 4.21: Comparison of two results of the segmentation task overlaid on the mosaic of NDVI values for the green carpet together with the water area represented by its NDWI values, colored in blue. One result is shown with the thin outer black curve, the other with the inner green one. These nearly matching curves are what one would expect by even slightly changing the masking thresholds of the two indices. Some unclassified pixels stand out due to their cyan and red colors.

images per year for decades provides a significant dataset for calibrating the recognizer.

Experimental Methodology

The masking operation is applied to a satellite image to determine which pixels represent plants, while the remaining pixels represent water. The masking criterion is based on the values obtained with a remote sensing index, which, in the case of NDVI and NDWI, ranges between -1 and +1. Pixels are considered acceptable for the desired characteristic if they exceed a predetermined threshold value. The research evaluates the results obtained using a range of thresholds to segment the NDVI and NDWI images of the lake. The most significant aspects of this process are shown in Figure 4.20. The table lists the unclassified pixels based on the threshold values used for joint masking on the two indices for a summer image when the plant island reaches its maximum extent. The colors of the table cells indicate the quality of the assessment, which reflects how closely the profiles obtained with the two indices match. The large green elliptical area in the center of the table indicates that the two profiles have a strong positive correlation and strengthens the hypothesis underlying this research challenge. The figure shows an example (4.20c) where the profiles fully match, and others (4.20a and 4.20b) where there are several pixels in which the two attributions conflict. These unsatisfactory results tend to increase when choosing pairs of thresholds that stray from the optimal area at the center of the table.

The proximity between the two water-vegetation demarcation lines, shown together in figure 4.21, reiterates the strong correlation between the profiles obtainable from the two remote sensing indices used in this research.

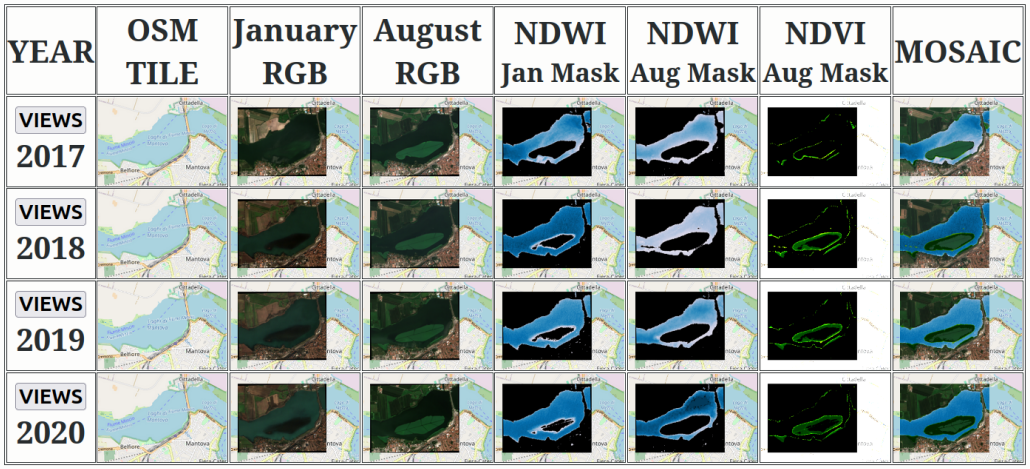

Figure 4.22: Periodic growth of macrophytes: the consistency with which the phenomenon repeats makes its analysis suitable for automation.

Experimental Results

This study requires time to complete. This section presents preliminary results obtained by applying the custom-built extraction tool to Mantua Superior lake and Fimon lake.

Beyond the visual outputs described so far, further analyzes will be conducted by extracting numerical values underlying the images or portions thereof. For instance, this will be achieved by mimicking the transect technique commonly used in aquatic vegetation studies. This method involves taking measurements along a predefined path, typically crossing from one shore to the opposite shore. Similarly, NDVI index values were extracted along a segment that bisects the summer vegetative island visualized in the aforementioned mosaic. The corresponding results are presented in the graph in Figure 4.23.

This research can be extended over long periods. In Figure 4.25, the plant island in Lake Mantua was monitored for two years. Some images show many uncertain red and cyan pixels that deserve further investigation. However,

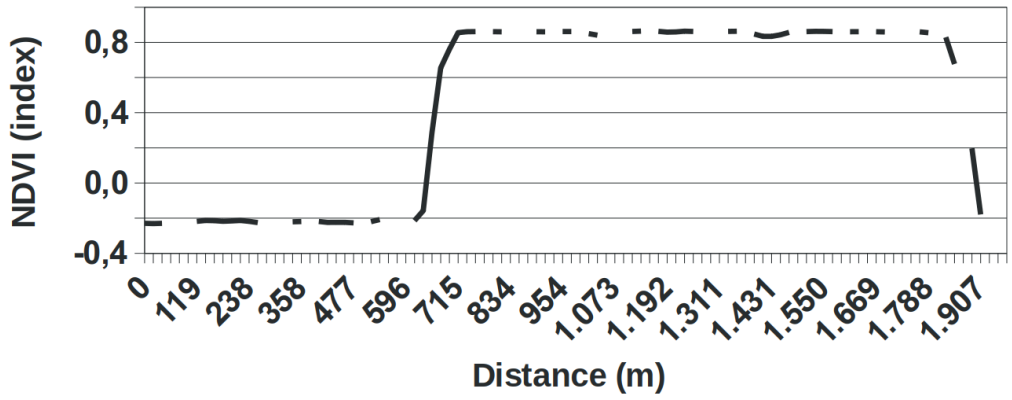

Figure 4.23: NDVI values increase as the transect crosses the vegetation island.

the seasonal trend is clear: plant growth intensifies in the summer. As a reference, similar results for the year 2015, obtained in [79], are highlighted in the graph in figure 4.24, where the authors study a lake exploiting LAI, the ratio of the total leaf surface area to the total soil surface area it covers.

Lake Fimon is another small, shallow lake with stagnant water in northern Italy. It experiences summer eutrophication episodes similar to those in Mantua and was chosen as a second target for testing the vegetation recognizer. The ideal masking thresholds for Mantua do not yield equally good results for Fimon, indicating that each context of use requires specific calibration. Figure 4.26 shows both the 2018 satellite images obtained with the recognizer and the corresponding original satellite images. Some have less than ideal cloud cover and should be replaced with clearer equivalents.

Figure 4.27 shows that the procedure developed for this research saves the underlying data in standard numerical form, which can then be easily imported and processed with any tool and returned in various formats.

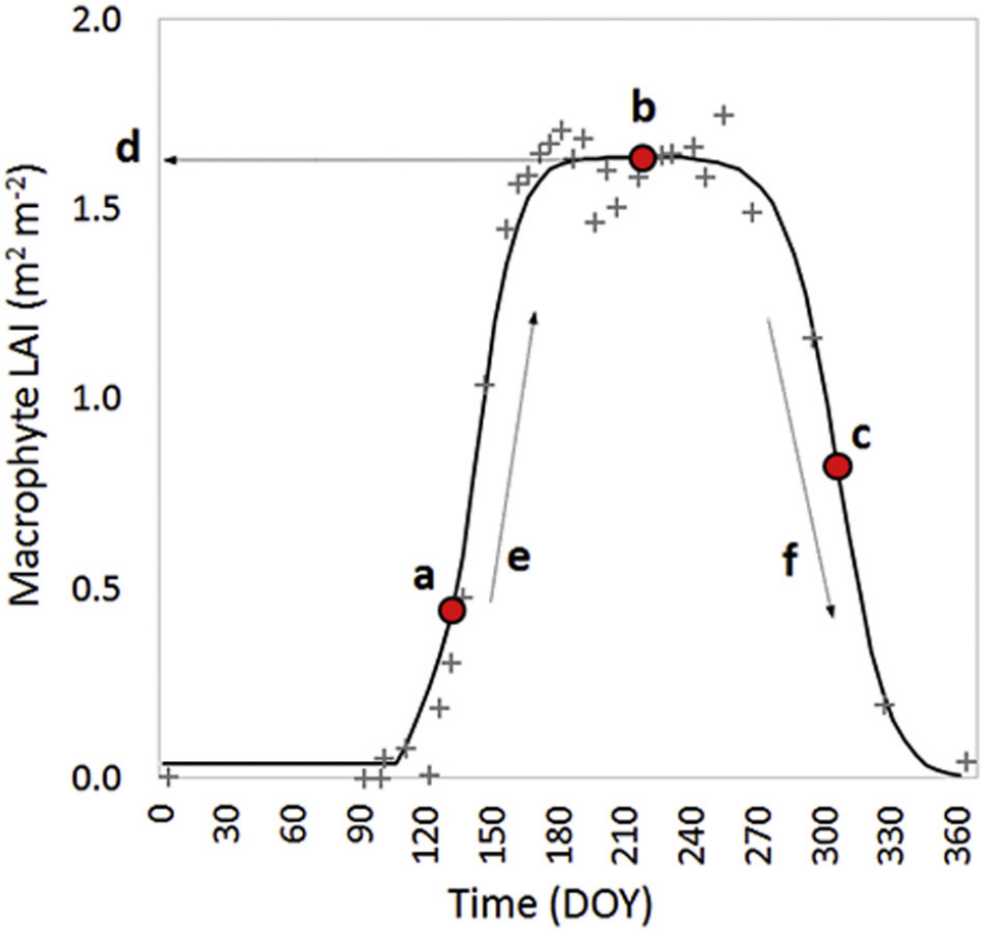

Figure 4.24: Metrics of seasonal dynamics, observed in 2015, derived from macrophyte Leaf Area Index (LAI) time series calculated using datasets obtained from Landsat satellites (Source [79]).

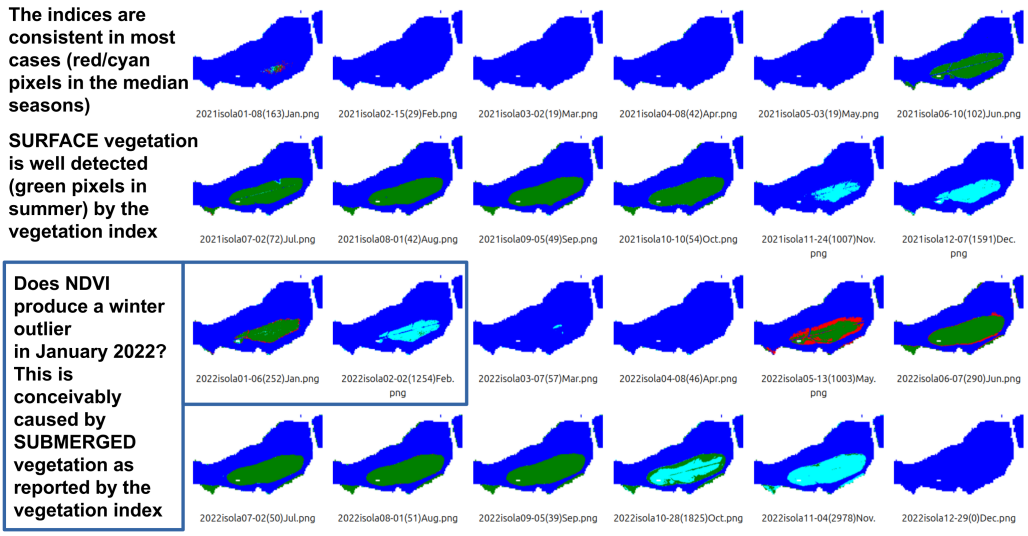

Figure 4.25: Mantua Lake Superior monthly trend [2021-2022].

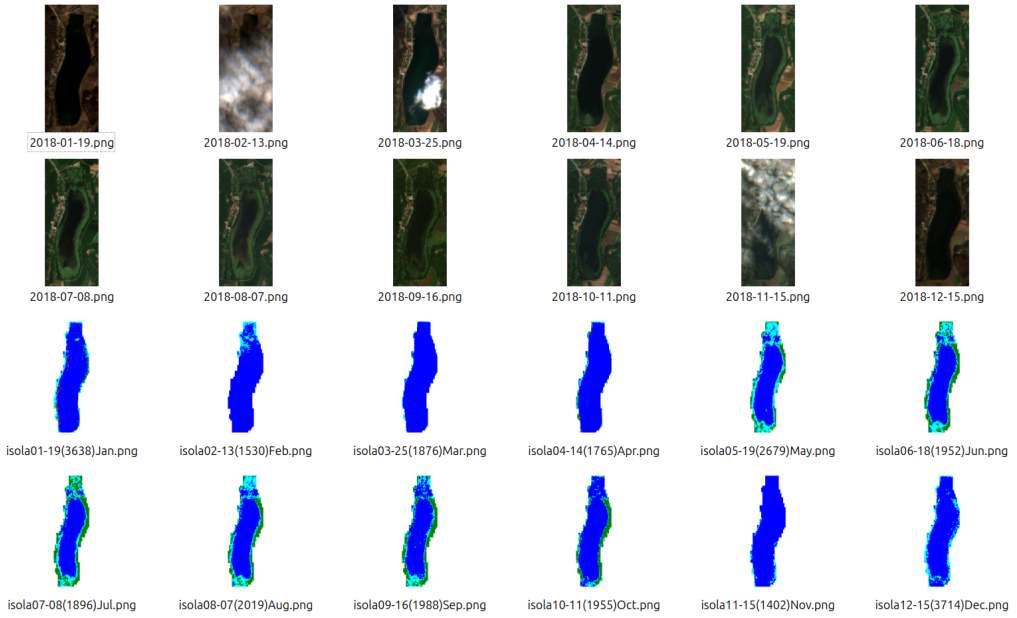

Figure 4.26: Fimon Lake (TV, Italy) Monthly Trend [2018].

Figure 4.27: Pixel classification exported to a csv sheet.

4.3.4 The River Use Case

This chapter focuses on the second application scenario addressed by the thesis, which applies the Remote Sensing approach in a riverine context.

The Challenges

The research challenge is twofold. Develop an automated tool that tracks a river stretch using satellite imagery and transforms the pixels into valuable data about the turbidity of the transported water. Then, visualize the extracted information in the form of explanatory graphs that highlight significant spatiotemporal trends. This represents a complex study domain of multidimensional nature. To explore the data through its three fundamental axes, the plots were organized into corresponding strands, which can be defined as space, time, and turbidity, each deserving further consideration below. Spatially, the river was simplified using a dedicated original algorithm, as described in the section about the Pipeline. The surface traversed by the Mincio River before flowing into Lake Mantua was reduced to a linear span of 44 kilometers, which was then segmented into a sequence of equal-length sections at a chosen granularity of 500 meters. Regarding the temporal factor, the river was observed over the course of a year, selecting one day each month. Significant differences were identified between the cultivation season (warm) and the inactive season (cold). This section reports some highlights of these challenging tasks, using explanatory images.

Turbidity was derived by applying the classical remote sensing index NDTI to the river sections described above. Several increases in turbidity values were detected, significant both in intensity and suddenness at key points along the river. The most important of these were highlighted in the plots to help understand the origin of the phenomenon. Some cases have been subjected

to a more in-depth analysis, among which the confluence with the Goldone tributary has provided indicative results.

Turbidity increases tend to subside, with values often returning to their pre-disturbance state—a circumstance that may be referred to as recovery. Some plots were devoted to describing the characteristics of such recovery events, including the spatial extent and intensity involved, which proved to be highly variable across cases. This representation was intended to facilitate an understanding of the river's apparent self-purifying capacity.

Use Cases and Areas of Interest

The use case of this study aims to develop an automated tool to monitor turbidity values in rivers and their most significant variations. Detecting and quantifying phenomena of rapid and intense increases in turbidity is important, as these may be symptoms of point-source pollution events of various kinds. This phenomenon, explained in the introduction of the thesis, characterizes many rivers, especially in the most anthropized areas of the planet, where natural processes are compounded by intense human activity. The analysis of what happens in the stretches following such disturbances is also significant, as it allows for an assessment of the river's resilience—its capacity to restore initial conditions, how quickly and to what extent, and under which circumstances this recovery occurs more effectively or less effectively.

In the studied case, highly turbid waters are often found downstream of urban settlements. These are caused by a high load of suspended solids and nutrients; however, these particles are also discharged by highly turbid tributaries such as the Osone, which receives drainage water from intensively cultivated areas. This is evidenced by its markedly lighter color compared to the Mincio, into which it flows, as clearly visible in the image in Figure

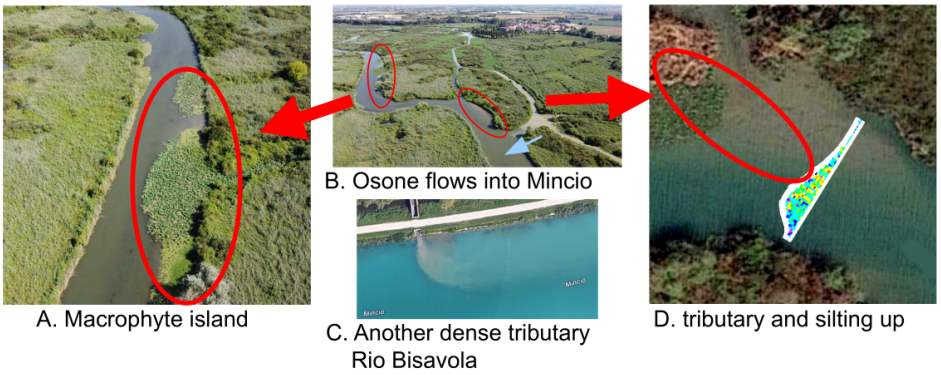

Figure 4.28: Significant locations inside the ROI for this Use Case. a,b,d: archive footage. c:Google Maps.

4.28. It is reasonable to hypothesize that this mass of particles, through deposition, may cause sedimentation events that are hazardous for navigation and accelerate the natural process of riverbed infilling, as illustrated in the figure and posited by a research group at the University of Parma that has studied this phenomenon [5].

The Goldone tributary is another very small watercourse that is equally important for this study. It extends across a long and narrow Area of Interest (abbreviated as ROI or AOI) that follows the upper reaches of the Mincio River. The visible effect of its water flowing into the Mincio is reported in Figure 4.29.

The Mincio originates from Lake Garda and flows across the Po Valley until it feeds into the three lakes of Mantua, which are located within the province of Mantua, Lombardy, in Northern Italy. The river reach under consideration covers approximately 44 kilometers. As explained in the "Processing Pipeline" section, it is linearized using a dedicated algorithm that identifies a sequence of tangent circles, segmenting the river's course into sections of 500 meters each. However, the distance can be customized to suit

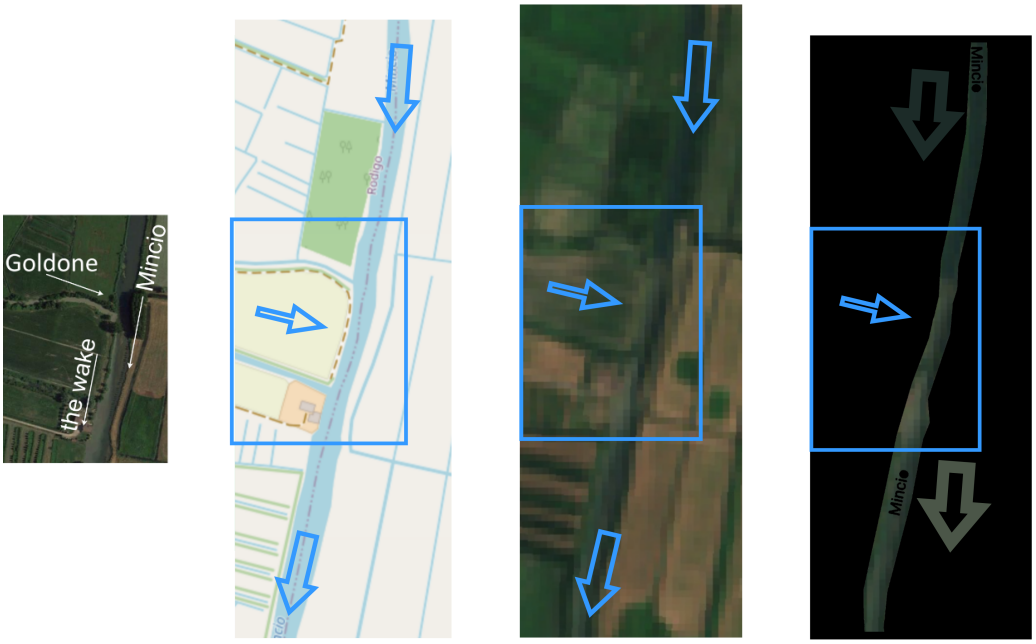

(a) (b) (c) (d)

Figure 4.29: High levels of turbidity are manifested by clearer waters. The wake is visible to the naked eye, caused by the Goldone effluent flowing into the receiving river. Remote sensing techniques detect and quantify it precisely, allowing us to investigate the course of the river and help pinpoint potential sources of pollution. In 4.29a, a drone captured the dense waters of the Goldone canal flowing into the Mincio. In 4.29b, the Mincio river and its tributary are depicted in an OpenStreetMap tile. The arrows indicate the direction of water flow. In 4.29c, the True Color Copernicus image has a Ground Sample Distance (GSD) of 10 meters. In 4.29d, the color of the river turns lighter due to the high-turbidity tributary. Only by masking the background does it become evident and distinct from the surrounding land.

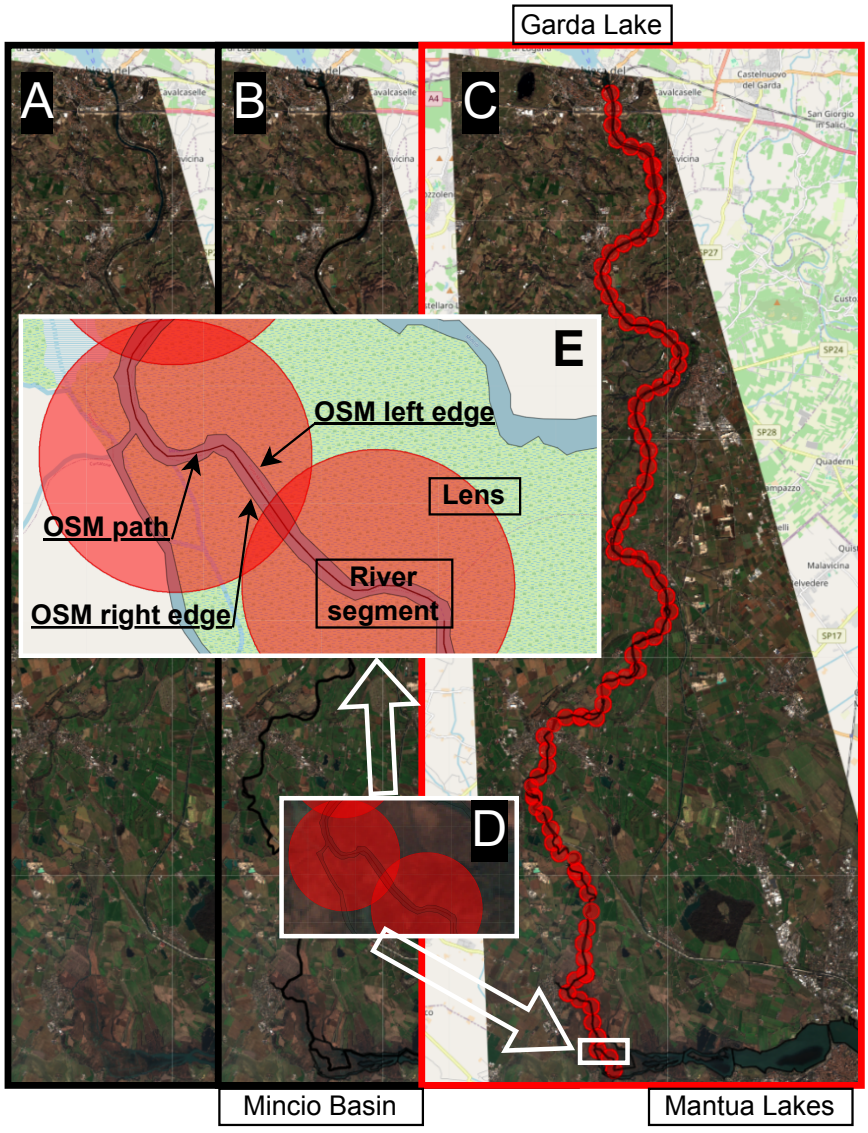

Figure 4.30: The ROI. A) RGB-only view. B) River edge overlay. C) Circular lenses used for NDTI measurements. D) Confluence of the Osone tributary into the Mincio. E) Confluence scaled up, with Open Street Map (OSM) algorithmic contributions, and results.

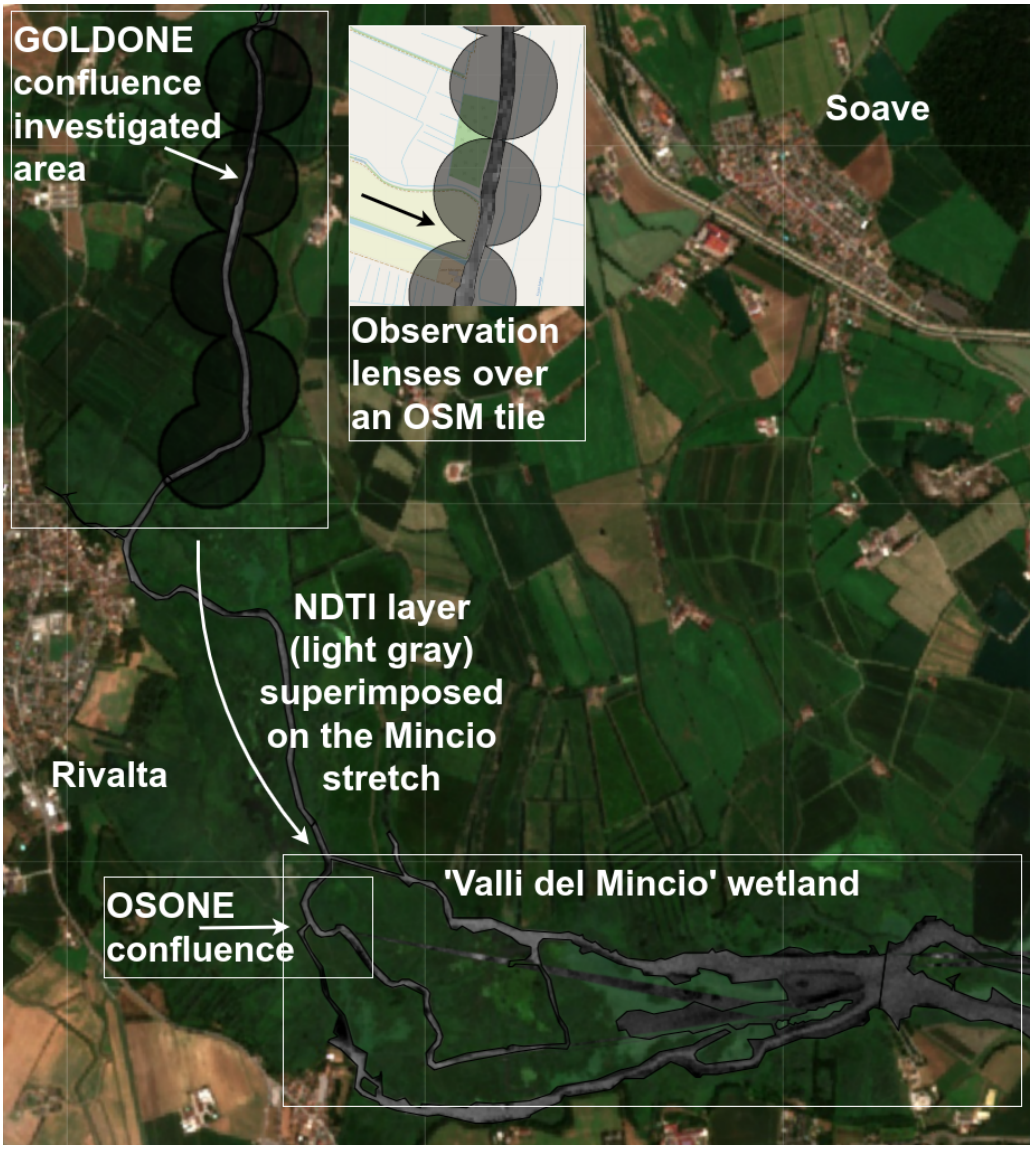

Figure 4.31: A portion of the Mincio River basin, the geographical area studied, captured by the Sentinel satellites. The boxes indicate the confluence with two drainage channels with particularly turbid water. The Goldone has been the subject of a detailed study. The dark circles represent some observation lenses used to calculate the values of the remote sensing indices.

the needs of other searches. These sections are the units for calculating the NDTI index across different seasons, producing datasets containing approximately 90 records—twice the number of kilometers analyzed. The resulting complete sequence of lenses is illustrated in Figure 4.30, which includes two insets showing the aforementioned Osone confluence. Figure 4.31 shows a particular area of the region of interest that includes the confluences of the Goldone and Osone tributaries into the main river, the Mincio.

The preliminary results obtained from this study are described later in the 4.3.4 section.

Experimental Methodology

This research extracts information from satellite images of the Copernicus mission, with the purpose of analyzing turbidity data and its variations in the waters of the Mincio River, a mid-sized river in the Po Valley. The study focuses on the upper course of the river, from its origin at Lake Garda to the outskirts of Mantua. The dataset is structured as a three-dimensional domain, described as follows. The spatial axis follows the river's path for 44 km, with discrete measurements taken every 500 meters, reporting the average for that stretch of the river. The temporal axis covers the year 2024, the most recent complete dataset available. Twelve satellite images were analyzed, one for each month, selecting a representative day with clear sky conditions. This dataset was complemented by a partial analysis of the 2023 data. The third axis concerns turbidity, the physical variable under investigation, estimated by calculating the Normalized Difference Turbidity Index (NDTI) from the images. In the observed conditions, the NDTI values varied continuously between -1 and approximately 0.

The working hypothesis is that the turbidity of the upper Mincio is

influenced by agricultural activities, effluents from the wastewater treatment plant at Lake Garda, and discharges from settlements encountered along the river course.

The observations, conjectures, and conclusive evidence were developed according to the three aforementioned dimensions of the study domain (space, time, and turbidity) and were supported by sets of visualizations: space-centric, time-centric, turbidity-focused, and 3D graphs. The latter proved particularly useful for providing an overall perspective and facilitating comparative analysis.

To gain an initial understanding of this broad and multidimensional space, the study began with spatial analysis. Turbidity was measured along the entire course of the river, following a precise procedure described herein. August was analyzed first, as it is representative of the summer season when agricultural and livestock activities are at their peak in the Mincio plain. Their inevitable by-products are released into the soil and subsequently drained into watercourses, as suggested by several studies, including those conducted by Prof. Bartoli's group [63]. Turbidity measurements may, therefore, provide insight into this impact. The analysis was then repeated on February imagery, representing the winter season when such activities are largely halted. November was also processed for completeness, yielding intermediate results as expected. This initial analysis was effective in highlighting significant differences in turbidity levels between seasons and in identifying approximately ten points along the river where substantial variations occur. These points were marked on a geographical map.

With respect to temporal trends, two specific segments among those identified earlier were examined in greater detail. Due to their limited length (a few kilometers), it was possible to extend the analysis to include all twelve

months of 2024. The confluence of the Goldone canal with the Mincio was selected as a case study. The Goldone collects runoff from agricultural fields and is one of the tributaries notoriously responsible for introducing significant amounts of suspended solids into the Mincio. Indeed, these tributaries are characterized by a light coloration during the summer, as highlighted by the drone imagery reported in previous sections. This analysis confirmed the significant seasonal trends observed earlier and further revealed the existence of two seasonal clusters, corresponding to productive and quiescent periods, marked by clear differences in turbidity dynamics across the twelve months.

At this stage, to study turbidity simultaneously in space and time, it has proven effective to employ a dedicated set of three-dimensional plots. A 3D visualization was generated for NDTI values at the confluence with the Goldone in 2024 and was subsequently extended to 2023 data, as well as to the confluence with the Fossa Redone Superiore, another drainage canal. This approach allowed us to highlight differences among these three cases.

The analysis concludes with a set of plots providing a refined examination of the most significant turbidity variations, applying the specific metrics proposed for this study (see the Evaluation Metrics section 4.3.2). The turbidity spikes were compared both across sites and between seasons, enabling an assessment of differences in intensity and variation rates, and highlighting cases where a persistent gap remained, i.e., where the river was unable to fully recover its pre-disturbance state.

All data processing scripts were developed in Python 3.12.3, using the geemap library (v0.35.1) within Jupyter notebooks executed in the integrated Visual Studio Code environment (v1.104.1). Graphs were generated with matplotlib (v3.10.5) on a Linux Ubuntu 24.04.1 system in 2025. Data storage and exchange were managed using Microsoft Excel spreadsheets in the

2007–365 .xlsx format.

Results and Critical Analysis

Spatial Analysis The objective of this analysis, the results of which are represented by graphs a–c in Figures 4.32 and 4.33, is to observe the turbidity dynamics in the upper stretch of the Mincio River (44 km) on two specific days in 2024: during the cold season (February 2) and the warm season (August 8). Turbidity was measured using the standard remote sensing index NDTI (Normalized Difference Turbidity Index), which is derived from satellite imagery. The primary axis reflects spatial variation, with graphs extending widely along the horizontal axis to mirror the river's length. On this basis, time is introduced as a comparative factor, contrasting cold- and warm-season data to reveal different trends. This approach highlights the points where turbidity reaches extreme values and where the river undergoes the most abrupt changes. These locations are subsequently selected for detailed temporal analyzes. Seasonal data are conventionally color-coded: blue (cold) and orange (warm). Orange was chosen instead of red for greater visual accessibility, particularly for visually impaired readers.

Graph 4.32a presents turbidity values. The upper horizontal axis reports the river kilometers downstream from the source at Peschiera del Garda. The vertical axis represents turbidity, ranging from -0.84 (very clear water, near the source; tick marks shaded in green) to +0.01 (more turbid water; tick marks shaded in red). The two data series represent the original values extracted from 500-meter raster segments. The lower horizontal axis indicates the progressive measurement number (corresponding to twice the distance in kilometers). The turbidity excursion is substantial, with a clear decline in transparency along the course. At the source, NDTI is approximately -0.45,

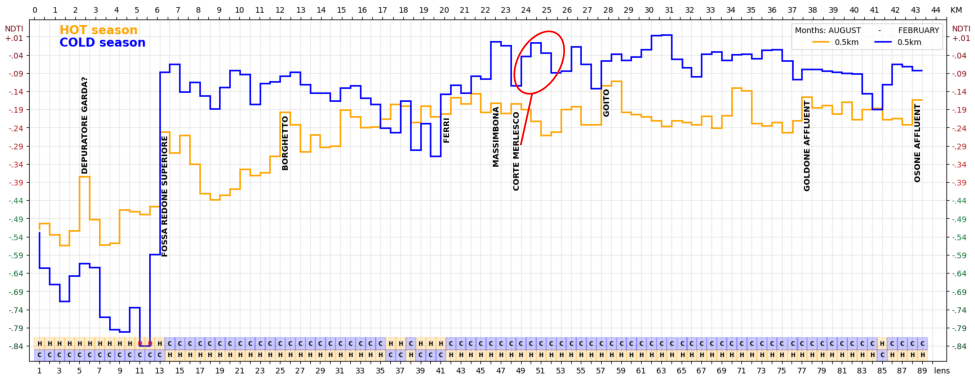

(a) NDTI VALUES - Average on 500 mt segments (seasonal comparison) (MORE TURBID stretches at the top). The peak circled in red is depicted in Figure 4.19. Among the reported locations (vertical texts) also appear the six peaks of the NDTI index examined in detail in the graph 4.37.

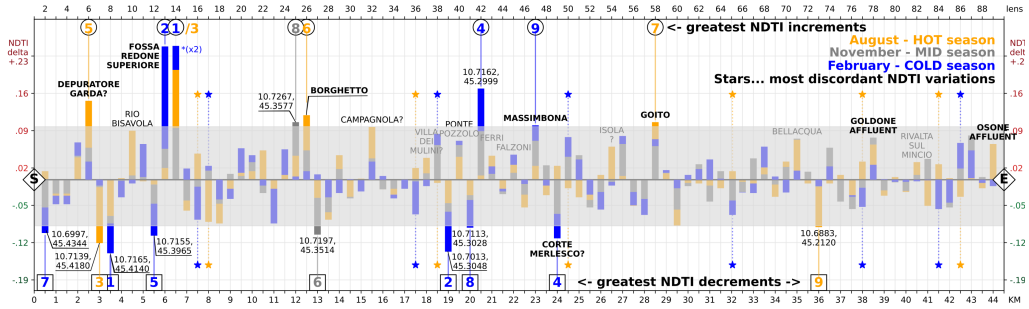

(b) NDTI VARIATIONS of 500 mt-long stretches - three seasons (UPWARDS bars in places that get THICKER, downwards -> cleaner)

(c) River Basin - High Mincio (from Garda Lake to Mantua) - OSM background, spots from GMaps or Sentinel-2 or drone

Figure 4.32: Spatial Analysis - 2024 NDTI values and variations along the entire upper course of the Mincio river.

while downstream it approaches -0.15, although there are seasonal differences.

In the cold season (blue), water from Lake Garda is initially very clear but becomes markedly turbid after 6 km, at the confluence with the Fossa Redone Superiore canal. Although variability persists, water quality does not return to initial levels. This reduced recovery in winter may be explained by the diminished phytodepurative activity of aquatic vegetation, which is less active or less abundant during this period.

In the warm season (orange), the water is moderately clear at the source but quickly becomes turbid after 3 km, near Salionze, coinciding with the discharge from the Gardesana community wastewater treatment plant. Its impact appears more pronounced in summer, likely due to the substantial seasonal increase in tourism around Lake Garda. The discharge from the Fossa Redone Superiore also contributes significantly during the summer. However, from that point downstream to the Mantua lakes, turbidity generally remains higher during the cold season, as highlighted by the comparative box plots at the bottom of the graph (labeled "Hot" and "Cold"), which are color-coded according to seasonal prevalence.

Graph 4.32b illustrates variations in turbidity rather than absolute values. The horizontal scale matches Graph 4.32a. Its purpose is to highlight the most intense spikes, i.e., points where turbidity shifts sharply. Bars diverge from a central baseline: upward bars indicate increasing turbidity, while downward bars mark decreases relative to the preceding 500-meter segment. Major fluctuations are labeled with local place names or GPS coordinates. As shown in Graph 4.32a, colors distinguish the seasons (blue for cold, orange for warm), with gray bars representing the intermediate season (November 3). Bars are overlaid, not stacked, so extreme values emerge clearly at the tips of the bars.

Turbidity changes ranged from a maximum decrease of -0.138 to a maximum increase of +0.25, except for one outlier spike (+0.5), which was truncated to prevent graph distortion. A gray rectangle hides smaller bars and highlights the most intense fluctuations, defined as those exceeding one-third of the maximum spike magnitude. This results in 18 prominent spikes (9 positive, 9 negative). Each is labeled with its name, ranked (1 = strongest), and marked with the season's color—circled for increases and boxed for decreases. Color segments within the vertical bars allow for immediate visual comparison across the three seasons and the 88 observed river segments. Results indicate that the cold season displayed the most intense variations (41 times), followed by the warm season (29 times) and the intermediate season (18 times). The graph also identifies locations where seasonal variations diverge, with turbidity rising in one season and falling in another, highlighted with star markers.

Graph 4.32c depicts the study area (upper Mincio) on a geographic map. The datasets used to plot the graphs were linearized to represent the river's course. Key locations where turbidity variations occur are marked on the map and illustrated with aerial imagery, satellite orthophotos, or drone images, including the circular masks applied by the remote sensing algorithm. Numbered labels correspond to critical positions highlighted in Graphs 4.32a and 4.32b. The map is rotated horizontally to facilitate reference with Graph 4.32a and Graph 4.32b.

Figure 4.33 presents three heat maps. Graph 4.33a shows the turbidity values for August 2024 (500-meter resolution) compared across increasing levels of spatial aggregation. The choice of a 500-meter sampling step is visually validated. Moving downstream, a clear trend toward increasing turbidity is observed, suggesting an accumulation of suspended particles

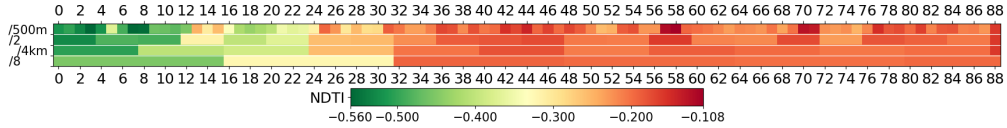

(a) NDTI Values - Spatial aggregations along the lenses (HOT season - August)

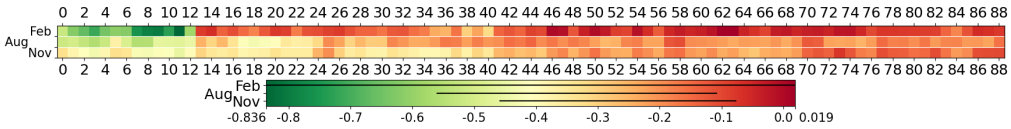

(b) NDTI Values - Seasonal comparison (February vs August vs November)

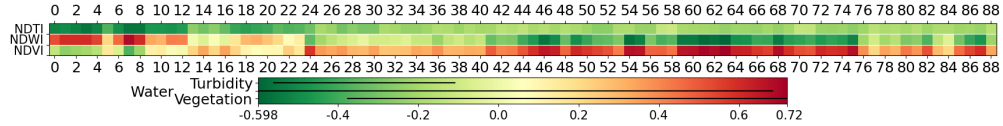

(c) NDTI, NDWI, NDVI Values - Remote Sensing indices comparison (Turbidity, Water, Vegetation) - August data

Figure 4.33: Spatial Analysis - Year 2024 data - Heat Maps - Aggregations, seasonal and indices comparisons.

discharged into the river.

Graph 4.33b compares NDTI values across the three seasons, confirming earlier observations. The accessory color bar below the graph, featuring black segment markers, facilitates interpretation.

Graph 4.33c compares turbidity data from August 2024 with values derived from two other popular remote sensing indices: NDWI (water) and NDVI (vegetation), extracted alongside NDTI. Unlike the previous graphs, the color ranges differ because NDWI and NDVI vary more widely than NDTI, as indicated by their respective color bar segments. An inverse relationship is evident between NDWI and NDVI, as expected from their antithetical meanings. Their relationship to NDTI, however, remains unclear and warrants further study beyond the scope of this work. Importantly, the developed extraction algorithm is adaptable to compute any RS index, provided that the required spectral bands are available in the satellite imagery.

Conclusion. The waters flowing from Lake Garda into the Mincio are objectively very clean, as civil and industrial wastewater is collected by an extensive and efficient sewer system around the lake. However, these substances eventually enter the river further downstream, along with substantial agricultural and livestock effluents during the warm season. This seasonal input significantly affects turbidity dynamics.

Temporal Analysis The following set of visuals, graphs a–e in Figure 4.34 and Figure 4.35, highlights more explicitly the temporal dimension, illustrating the values and variations of the turbidity index along nearly three kilometers of the Mincio River, centered on the confluence with its tributary, the Goldone. The data in this analysis have a finer spatial resolution—250 meters, half of that used in the preceding spatial analysis—in order to enable

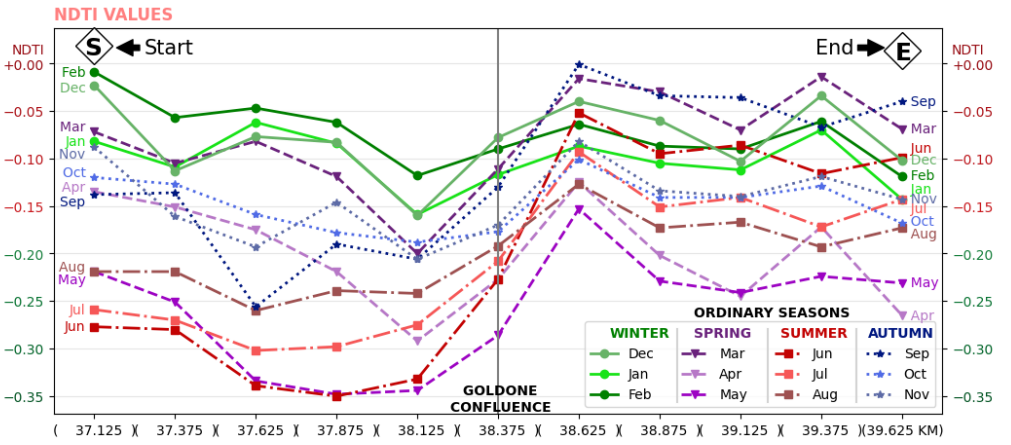

(a) Monthly TIME SERIES

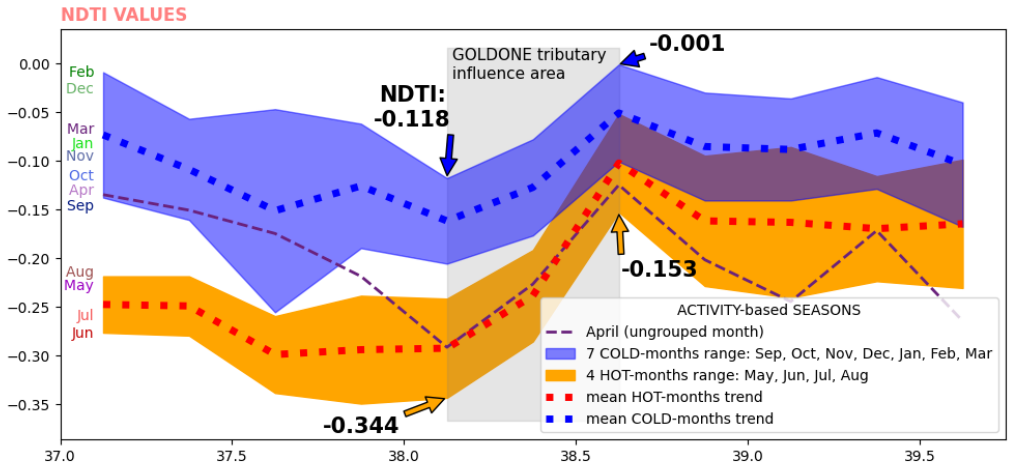

(b) Seasonal TRENDS

Figure 4.34: Temporal Analysis - Goldone/Mincio confluence - NDTI data along 3 Km stretch - year 2024.

more detailed observations. On the horizontal axis, brackets above the ticks schematically represent the spatial extent of the eleven circular windows employed in calculating the values displayed in the graphs (the kilometer marks indicate the distance of their centers from the river's source). The exact confluence point is indicated in gray: as a vertical line in Graph 4.34a and as a shaded area in Graph 4.34b. In the observed section, between km 37.000 and km 39.750, the NDTI values range from –0.349 to –0.001, showing significant temporal variability across the selected days over the twelve months of 2024. Higher NDTI values (highlighted in red on the vertical axes) correspond to more turbid waters. The same three-dimensional data domain used in the previous figures is explored here through different two-dimensional perspectives designed to facilitate interpretation, stimulate hypotheses, and support conclusions. Particular attention was paid to effective visualization strategies for this highly specific dataset. For example, the color scheme used to represent the months also differentiates the four seasons, as indicated in the legend of Graph 4.34a.

Graph 4.34a presents the temporal series and helps identify the months with stronger correlations. A seasonal trend is perceptible, albeit faintly. This pattern is better represented in Graph 4.34b, which highlights two seasonal clusters: seven months forming a "cold period," marked by a blue band, and four months forming a "warm period," highlighted in orange. April does not fit neatly into either cluster and is represented individually. The two bands remain separated, with their mean lines, shown as dashed curves, remaining consistently apart. These seasonal tendencies potentially reflect the differing natural dynamics and anthropogenic activities along the river across the two periods. The impact of the tributary is clearly visible; it consistently produces an increase in turbidity across all twelve months. It is also noteworthy that

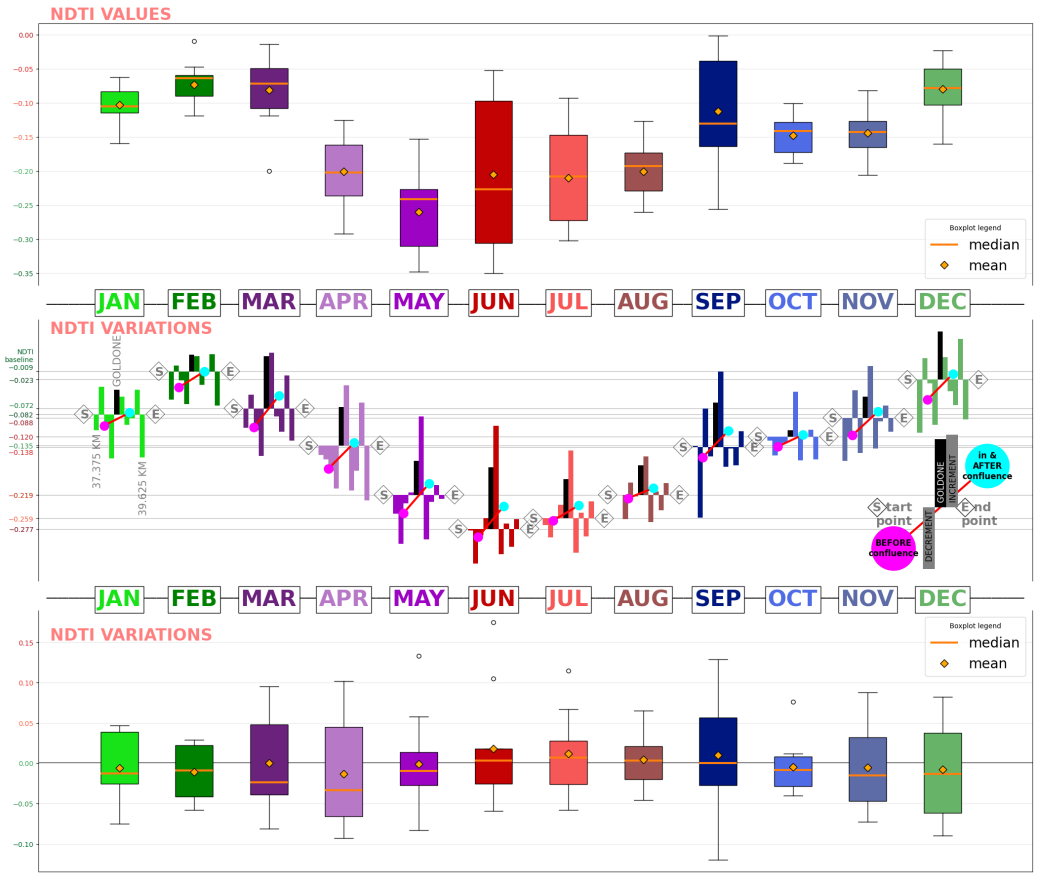

Figure 4.35: At the top : Monthly Excursions (along 3 Km centered stretch at the Mincio-Goldone confluence). In the middle : Monthly Increments/Decrements (drawn over each month's baseline at Km 37.125) At bottom : Monthly Variations.

winter waters remain more turbid overall (as already indicated in the spatial analysis). Graph 4.34b shows that turbidity, at the end of the studied reaches, tends to return to levels observed at the beginning. This "recovery effect," discussed in the metrics section, is weaker during the summer—an observation that warrants further explanation.

In Graph 4.34a, comparing the slope of the twelve monthly curves at the confluence reveals that turbidity variations are less intense in winter, being approximately half as strong, as suggested by the four highlighted arrows. This supports the hypothesis that the tributary carries a lower suspended sediment load during this period when agricultural activities are reduced. However, despite these insights, the heavy overlap of the monthly curves in Graph 4.34a makes interpretation difficult, necessitating the complementary use of the subsequent graphs. Later, three-dimensional plots will also allow comparisons across different years and locations.

The Graphs in Figure 4.35 provide a sharper temporal focus, displaying the twelve-month behavior across the eleven equidistant sampling points spanning the observed 3 km reach. The horizontal axis separates the months, avoiding the clutter of overlapping lines in Graph 4.34a. Metaphorically, it is as if the observer were traveling along the reach on a given day each month, drifting with the current and recording turbidity values along the way. This layout allows for a clearer assessment of temporal variation. Graph 4.35.top reports turbidity values for each month, while Graphs 4.35.middle and 4.35.bottom present their variations across the eleven points (2.75 km in total). The monthly color scheme is consistent with Graphs 4.34a and 4.34b. Bars extending above the axis midpoint indicate high or increasing turbidity; those extending downward indicate low or decreasing turbidity.

These three graphs emphasize the strongest absolute values and varia-

tions—indicating where and when the sharpest increases or decreases occurred. For each month, the box-and-whisker plots in Graphs 4.35.top and 4.35.bottom summarize the NDTI data, values, and variations, respectively, including the median, mean, and outliers. In contrast, Graph 4.35.middle uses histograms to represent the spatial variation across the eleven segments of the reach. Prolonged turbidity variations across longer sections are evident when adjacent bars show concordant patterns. In both Graphs 4.35.top and 4.35.middle, the vertical scale of turbidity is consistent, so that when examined sequentially, the monthly data form a sinusoidal pattern: higher in winter and lower in summer. This finding confirms what was already suggested by the spatial analysis; however, it is demonstrated here as a consistent trend without discontinuities.

This analysis aims to reveal the effect of the Goldone tributary on turbidity. Accordingly, in Graph 4.35.middle, the bars corresponding to the tributary's outlet are colored black for each month. Superimposed on each histogram are paired circles—cyan to the right of the confluence and magenta to the left—indicating the average magnitude of NDTI variation within the respective sub-reach. The connecting red segments linking the paired circles across months express spatial differences in turbidity. The slope of these segments is consistently positive, indicating an increase in turbidity across all months. However, the degree of slope varies, with stronger differences from March to June and again in September, November, and December. These are the periods when the gap between pre- and post-confluence turbidity is greatest.

Comprehensive Graphs The 3D graphs presented here, a–c in Figure 4.36, aim to replicate the three-dimensional structure of the dataset under study: along the X-axis is the river course, along the Y-axis is time (in months), and

along the Z-axis are the NDTI values (turbidity). The twelve bars represent the changes in turbidity along the study reach over the twelve months. The confluence with the Goldone is depicted in Graph 4.36a, based on 2024 data, and in Graph 4.36b, based on 2023 data. Graph 4.36c shows the confluence with the "Fossa Redone Superiore" canal in 2023. The three-dimensional visualization facilitates comparisons across different locations and years.

Along the X-axis, the bars report mean NDTI values calculated over 500-meter segments, yielding six measurements per month and a total of 72 data points across the twelve months. Despite this aggregation, many bars still overlap, which prompted a reordering strategy. Months are displayed starting from May rather than January, thereby foregrounding the lower summer block. To further reduce visual confusion, the 3D graphs employ a set of six distinguishable colors, repeated twice for the twelve months. The points corresponding to the tributary outlet are highlighted on four horizontal planes and along the four connecting edges, marked with dark dashed lines. Corresponding segments along the bars representing turbidity values are also emphasized with white dashed lines. These are the steepest slopes, confirming the abrupt turbidity shifts caused by the Goldone inflow. In all graphs, including these, turbidity increases upward, with reddish ticks on the vertical axis denoting higher NDTI values (more turbid waters) and green ticks indicating lower values (clearer waters).

The two YZ planes are also used to display additional information. They show turbidity excursions through twelve vertical segments, which are projections of monthly NDTI values extending from the bars to both sides. Their vertical extent indicates the magnitude of monthly variation. Colored areas on the rear-left plane connect these monthly excursion bars, thereby reaffirming the seasonal clusters described earlier: orange for the warm season, blue for

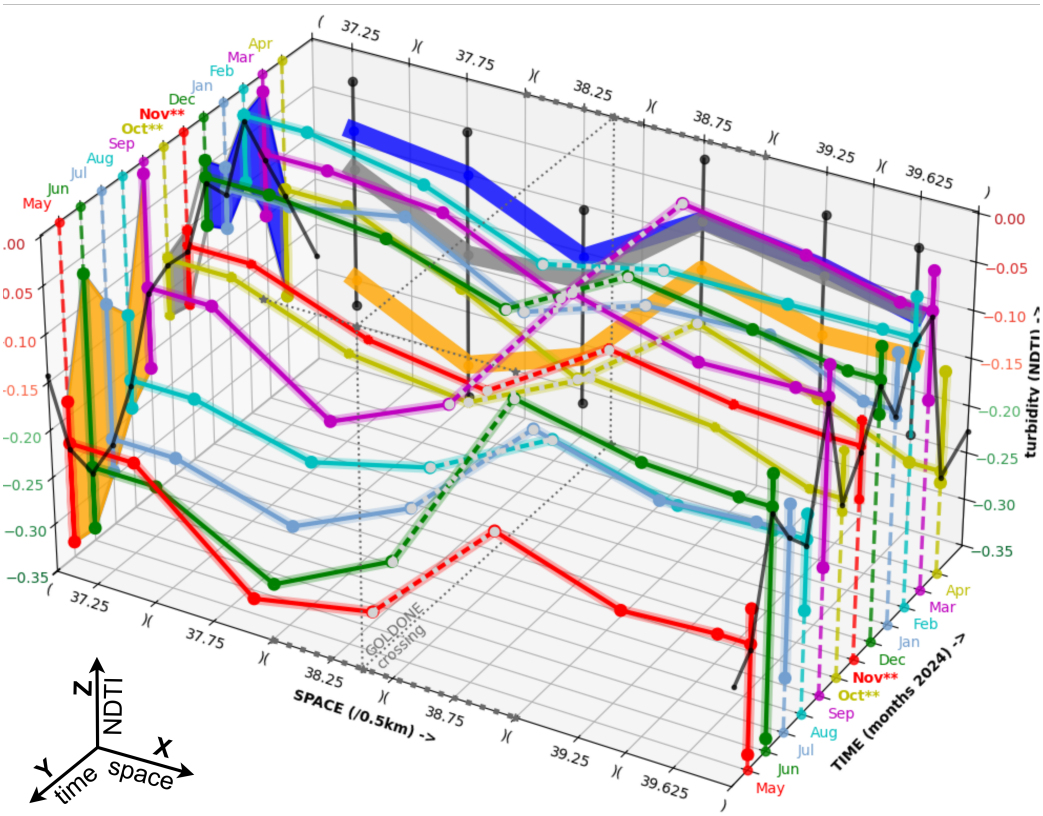

(a) Goldone confluence in 2024

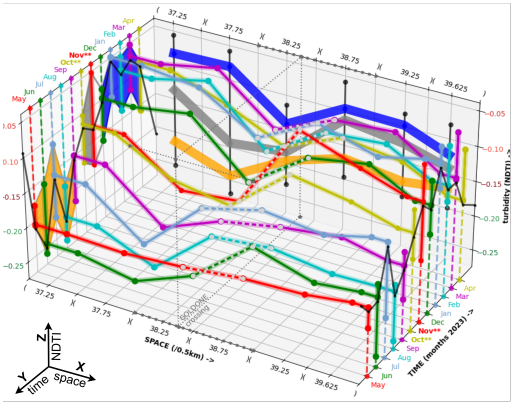

(b) Goldone confluence in 2023

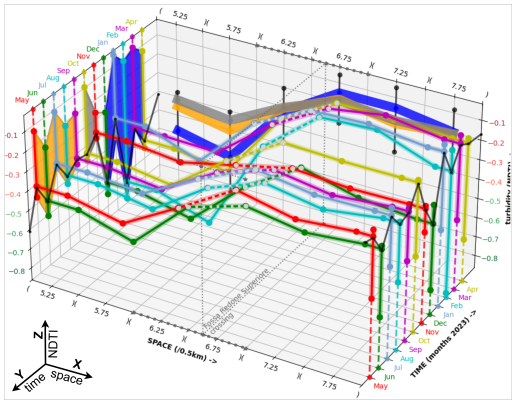

(c) 'Fossa Redone Superiore' in 2023

Figure 4.36: 3D Comprehensive Graphs - Space, Time and NDTI values and excursions on two major tributaries.

the cold season, and gray for the transitional period.

On the rear-right plane, which is also visible in the background, turbidity excursions are shown in a "transversal" direction. These are projections of the measurements recorded at the six observation windows across the twelve months of the year. This dual perspective, afforded by the 3D visualization, provides greater interpretive power. On the rear plane, median seasonal lines are also drawn—the three colored bands (orange, gray, and blue) that confirm the dynamics observed in Graph 4.36a of the temporal analysis. In 2023, these bands are clearly separated; in 2024, the cold and transitional bands partially overlap.

Beyond faithfully representing the spatial structure of the study area, the 3D graphs offer the advantage of displaying the underlying dataset in a compact form while enabling additional insights that confirm or complement findings from the previous 2D analyzes. For instance, the 2023 graph of the Goldone confluence clearly suggested reclassifying September into the warm cluster and shifting October and November closer to the cold group. This adjustment was possible because, unlike two-dimensional representations, the 3D layout places sequential turbidity changes side by side with less visual overlap, and their excursions, projected onto the planes, provide decisive interpretive leverage. In the case of the Goldone confluence in 2023, the seasonal assignment of these months appears less clear-cut.

Graph 4.36c, showing 2023 data for a different location—the confluence with the "Fossa Redone Superiore"—suggests further observations. The twelve bars exhibit much greater uniformity, with less temporal variability than the two Goldone graphs. This is confirmed by the three seasonal bands in the background, which overlap substantially. Only the blue band diverges, and only in the initial segment, a pattern corroborated by the excursion traces

projected onto the rear-left plane, which indicate greater NDTI variability during the cold season. The black polyline connecting the initial NDTI values along the left axis further distinguishes the two sites. In the Fossa graph, the polyline consistently lies at the base of the three colored surfaces, indicating that turbidity starts low and rises steadily along the reach in all months. In contrast, at the Goldone confluence, the black polyline remains low during the warm season (orange area) but shifts upward during the cold season (blue area) in both 2023 and 2024. This confirms that turbidity begins low and increases in the summer, whereas in winter, it starts high from the outset.

Analysis of Turbidity Spikes The aim of this set of graphs, represented in Figure 4.37, is to investigate intense turbidity spikes—specific points along the river where turbidity undergoes significant perturbations. Six notable spikes, selected from those identified in the previous spatial analysis, are reported. These spikes are analyzed across the two seasons, resulting in twelve visualizations. The individual behavior of each spike is depicted in detail, highlighting seasonal differences, the spatial extent, the speed of recovery (i.e., how quickly turbidity returns to baseline), and the magnitude of restoration. Reference is made to the dedicated section of this thesis on the original metrics specifically designed to quantify these phenomena.

These graphs demonstrate that recovery occurs following each spike, but to varying degrees. If increases in turbidity are interpreted as potential pollution events, the subsequent return to clarity can be understood as a process of natural remediation. Consequently, studying the characteristics of these recoveries—intensity, temporal and spatial dynamics, and modality—is of particular interest. Each graph pairs the turbidity increase with the subsequent decrease along the horizontal axis, which represents distance,

allowing for the assessment of the river's resilience.

Each spike is labeled with a circled number, following the numbering adopted in Graph 4.32b of the spatial analysis. For each location, the graphs for the two seasons are displayed side by side, with summer data on an ochre background and winter data on a light blue background. Bar charts highlight the contribution of individual river segments to each spike, which is also expressed as a percentage of the total turbidity variation. The intensity of the twelve spikes is represented using a uniform scale to facilitate visual comparison. At the base of each graph, the baseline NDTI value and the magnitude of the spike are indicated.

The increase and subsequent decrease that constitute each spike occur at a specific rate (i.e., the magnitude of change per kilometer), which is visually encoded using a color scale at the top of the graph. Two scales are employed: red hues for increases and green hues for decreases, with more intense colors corresponding to faster NDTI variations. Spikes that do not fully recover are highlighted, with the last bar on the right (representing the incomplete decrease) colored black and accompanied by the corresponding percentage of the unrecuperated drop, referred to as the "gap."

Eight of the twelve cases examined display a gap, in some instances of moderate magnitude (30%), but more often, the gap is substantial. A particularly notable case is the confluence with the Fossa canal, where the winter spike is very pronounced (NDTI increase +0.774), and only 10% of the lost clarity is recovered. In summer, the Fossa-induced spike is much smaller (+0.174), and recovery is considerably more complete. This pronounced seasonal difference warrants further investigation. Overall, the spikes exhibit highly variable characteristics between seasons at each location. The six examined sites are presented in order of their distance from the river source;

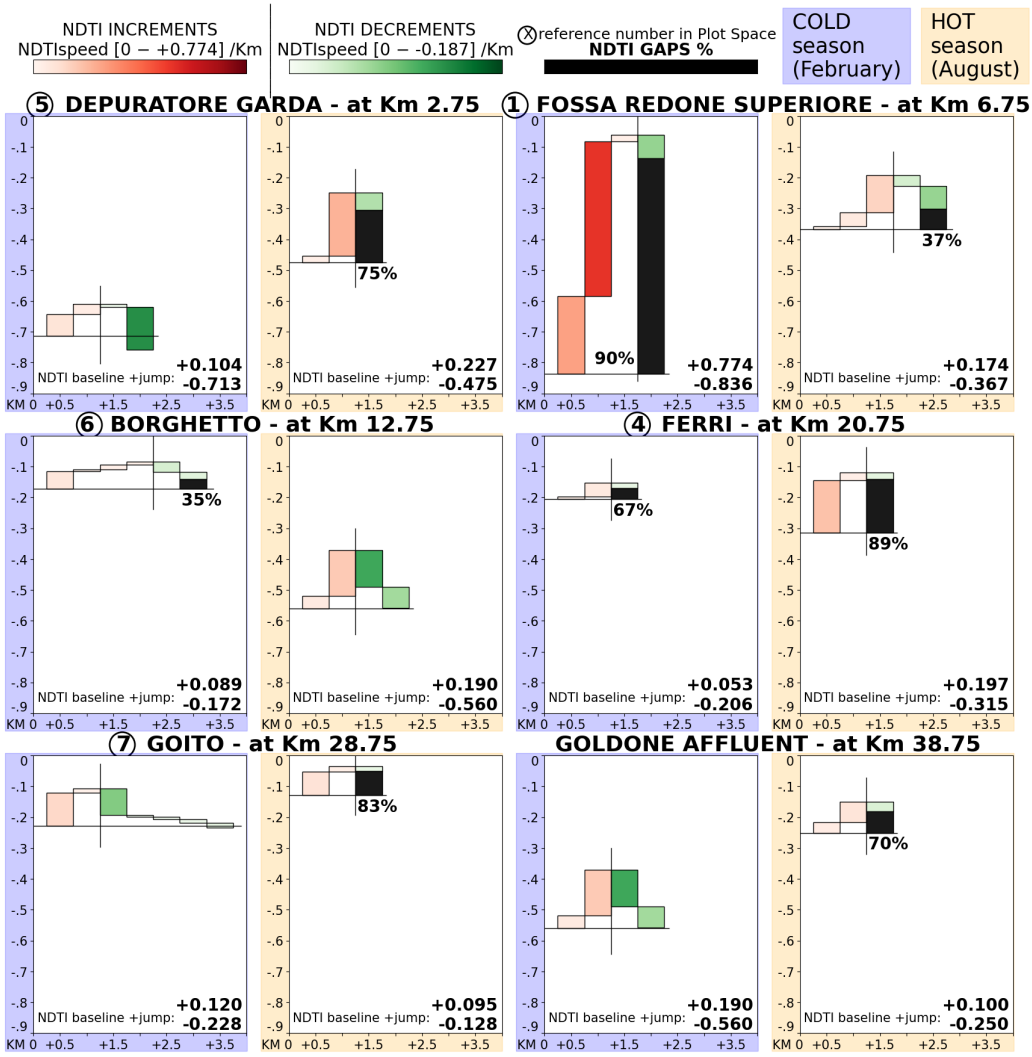

Figure 4.37: Spike Focused Plots - The Six Most Intense NDTI Spikes along the Mincio - year 2024. NDTI metrics described in section 4.3.2.

however, this variable does not appear to influence the nature of the spikes.

Limitations

As with many remote sensing studies, this research faces certain technical and methodological limitations. This section outlines some difficulties encountered during the development of this research. Some have been successfully addressed, while others remain open issues with only partially defined solutions.

During the image acquisition phase, the need for a dataset capable of resolving the fine-scale details of a narrow river, such as the Mincio, became evident. Consequently, the Copernicus platform was preferred over Landsat, as discussed in the section dedicated to the processing pipeline. Nonetheless, the restriction of analyzing areas of 10 square meters limits the spatial refinement achievable in the evaluation.

Temporal constraints also affect the study. Although the analyzes presented here have yielded significant insights, they are limited to a single year of observation. Expanding the temporal window is necessary to strengthen the robustness of the findings and to enable long-term observations and comparisons. Further assessment may also suggest replacing the current daily measurements with monthly-averaged analyzes to mitigate the influence of transient anomalies.

The pre-processing phase presents an additional limitation: it does not account for the presence of bridge and dam structures along the river course. These features, clearly visible in satellite imagery, tend to artificially increase NDTI values within the observation windows in which they appear. In practice, bridges are frequently located near populated areas, amplifying the NDTI spikes already caused by typical urban discharges. This contamination of results occurs because the riverine OSM dataset used in this study rarely

filters out regions occupied by such structures. A suitable solution would involve integrating the current focusing algorithm with a complementary pass on the cartographic OSM dataset in order to exclude unwanted surfaces from index computation.

Further evaluations of the model's limitations—and potential refinements—could also arise from collaboration with domain experts. Their contributions, including in-situ measurements and photographic documentation, would provide valuable validation and verification support for the ongoing development of the research.

4.4 Conclusion

My doctoral research concluded with the study of surface water bodies, which play a fundamental role in providing ecosystem services but are increasingly threatened by unsustainable agro-industrial practices. By monitoring turbidity trends and fluctuations, as well as the evolution of the extension of the aquatic plant island of floating species at the surface, the system allows us to identify the various impacts that affect the water quality of rivers and lakes subjected to eutrophication pressures. It produces output such as maps, graphs, and data tables through an efficient processing pipeline, providing meaningful information for medium-sized rivers and lakes in the Po River basin, a heavily anthropized area. The study required the development of an open-source, cloud-based remote sensing tool conceived specifically to support this analysis. However, the application is not limited to the Mincio River and the Mantuan lakes; its potential extensions are significant.

By integrating higher-resolution satellite datasets, the tool could be applied to narrower channels and tributaries—for instance, the aforementioned

Figure 4.38: The narrow Osone canal flows into the Mincio.

Goldone and Osone streams, which flow into the Mincio and are only 10 meters wide. Technically, this would also make it possible to trace back the pollution sources responsible for the turbidity peaks reported in this study through the tributaries that produce them. Hopefully, even the finer ones, like the one shown in Figure 4.28. Indeed, the Osone is significantly narrower than the Mincio, as clearly shown again in Figure 4.38. It is so narrow that it is not included in the OSM dataset; therefore, it should be treated with a different technique than the one used in this work. The analysis could be expanded to other rivers experiencing similar environmental challenges. A preliminary attempt on the nearby Oglio river has already yielded promising results.

The turbidity analysis framework developed in this work could be further extended to new applications, such as following the course of rivers to detect anomalous vegetative islands or sediment accumulation—examples are shown

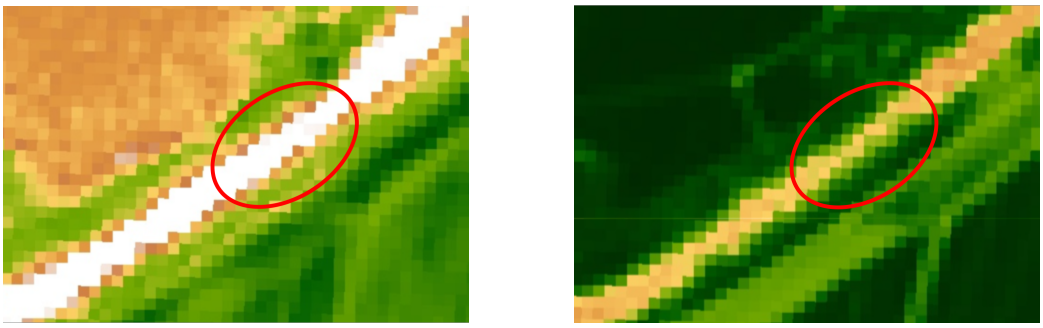

(a) Winter NDVI index.

(b) Summer NDVI index.

Figure 4.39: The possible presence of potentially dangerous vegetation on the banks of the Mincio, visible through the narrowing in the summer image calculated using the vegetation index. In winter, the river is much wider at that point.

in Figure 4.28—phenomena that can significantly hinder navigation and water flow. This goal could be achieved by complementing the NDTI index with vegetation and water indices, such as NDVI and NDWI, which are already produced as outputs in the current version, as reported in Figure 4.33. Figure 4.39 shows a point on the river where the vegetation index indicates a critical situation worthy of further study.

It would be interesting to integrate this research to study other promising correlations. For example, the fluctuations reported in the Analysis of Turbidity Spikes section could be cross-referenced with rainfall, river meandering, and flow velocity to assess whether these factors impact turbidity variability dynamics.

Conclusions

This thesis addresses the challenges posed by intensive agro-livestock practices in the Po Valley through the development of a coherent set of Environmental Informatics tools and methodologies aimed at multi-scale monitoring of manure management processes and their impacts on ecosystems. The contributions presented integrate process modeling, Internet of Things (IoT) architectures, simulation, and automated analysis of remote sensing data, outlining a unified and scalable methodological framework.

During the initial phase of the study, the foundations for the research were established. Extensive documentation activities were carried out regarding the geographical context under investigation and the environmental issues affecting the main water bodies of the provincial territory—the primary river and the lakes of Mantua. This involved reviewing analyzes conducted by local authorities, consulting the scientific literature, engaging with domain experts and leading manufacturers of environmental analysis instruments, as well as participating in conferences and trade fairs. Both the state of the art, discussed in detail in the introductory chapter of the thesis, and the exchange with peers proved to be essential for developing awareness and understanding of the topic and the available tools to investigate these issues, as well as for designing a pragmatic and sustainable research plan.

From an operational and architectural perspective, the thesis proposed a

modular IoT-based approach for the real-time monitoring of livestock manure transport and spreading operations. The systematic modeling of operational phases and interactions among heterogeneous actors enabled the design and prototyping of a system capable of supporting traceability, continuous data collection, and interoperability among sensors, vehicles, and control systems. This contribution addresses a significant gap in the current scientific literature and regulatory practice: while environmental studies have widely documented the pressure exerted by livestock and agricultural activities, and several IoT solutions have been proposed for monitoring soil and crop conditions, very limited attention has been devoted to the intelligent and continuous monitoring of livestock waste spreading activities. Moreover, existing regulatory frameworks, such as those derived from the EU Nitrates Directive and regional policies, generally rely on ex-post reporting and do not provide mechanisms for continuous operational monitoring, making enforcement and environmental accountability particularly challenging. Within this context, the thesis introduces an original technical contribution consisting of a low-cost IoT-based real-time navigation and monitoring system designed specifically for manure transport and spreading operations. The proposed solution integrates a web-based interface and real-time communication capabilities to guide drivers toward designated spreading locations, monitor operational activities, track tanker routes, and report both the quantity and the geographic distribution of effluent spreading. Beyond simple tracking, the system represents the initial step toward an operational supervisory platform capable of improving the transparency, coordination, and environmental sustainability of manure management practices. To support the design and validation of the architecture, a simulation environment was developed to emulate realistic manure spreading missions in the Po Valley, including an emulator of drivers'

operational behaviors and the simultaneous management of multiple tanker trucks. This level of simulation made it possible to explore critical issues, limitations, and scalability requirements prior to field deployment, thereby reducing implementation costs and risks.

In parallel, the thesis addressed the problem of downstream environmental impact monitoring, focusing on surface water systems and phenomena such as eutrophication, macrophyte growth, and turbidity variations. Although remote sensing techniques and spectral indices have been widely applied to study water bodies and aquatic vegetation, the scientific literature reveals a limited exploration of the spatiotemporal variation of turbidity along river courses, particularly when continuous and spatially structured observations are required. This represents a relevant research gap, considering that turbidity dynamics in rivers can act as a direct indicator of environmental pressures related to agri-food activities and land management practices. To address this limitation, the thesis proposes an original methodological framework for extracting and analyzing turbidity patterns from satellite imagery. The approach introduces several technical innovations designed to enable precise and scalable monitoring of river systems. First, a graphical technique was developed to accurately follow the morphological profile of a river, allowing the extraction of satellite-derived information along complex hydrographic paths rather than through conventional pixel-based sampling. Second, the method allows turbidity data to be reconstructed at user-defined spatial resolutions, enabling flexible analysis depending on the scale of the study. Third, the framework includes an innovative set of visualization tools, including three-dimensional plots that support the exploration of turbidity dynamics and highlight the most significant fluctuations over time and space. These capabilities are embedded within a specially designed automated workflow,

referred to as the pipeline, which structures the complete processing chain from satellite data acquisition and filtering to feature extraction and analysis. The pipeline is complemented by a set of specifically designed evaluation metrics that allow the systematic characterization of turbidity variability and support comparative analyses across different temporal windows and spatial segments of the river network. A further methodological contribution is represented by the integration of satellite raster data with georeferenced vector data from open sources, which enabled analysis along complex hydrographic structures through novel spatial segmentation and aggregation techniques. Applications to real-world case studies, including urban lakes and river courses within the Po River basin, demonstrated the ability of the proposed tools to quantify complex spatiotemporal dynamics and to produce interpretable outputs in the form of maps, charts, animations, and structured datasets. Together, these contributions provide a novel and operational framework for the remote sensing–based monitoring of turbidity in river systems, addressing a previously underexplored aspect of environmental monitoring related to agricultural impacts.

The results obtained also highlight several limitations. Prospective future developments include the validation of the IoT system prototype developed in this work within real operational scenarios, in collaboration with companies operating in the region, in order to collect longitudinal data useful for analyzing operational behaviors, detecting anomalies, and optimizing decision-making processes.

With regard to remote sensing, the analyzes are strongly dependent on the availability of high-resolution satellite imagery, particularly when applied to small-section watercourses. Moreover, extending the tools to more heterogeneous environmental contexts requires the introduction of additional

variables, increased algorithmic complexity, and more advanced management of uncertainty related to the quality of observational data. In this perspective, the integration of higher-resolution satellite datasets would enable the extension of the analyzes to minor channels and tributaries, facilitating the identification of point-source pollution. Further improvements include the exploration of alternative and combined indices, the integration of exogenous factors such as precipitation, river morphology, and flow velocity, as well as the adoption of Machine Learning approaches to more effectively manage the increasing complexity of the models.

Overall, this thesis demonstrates how the integration of IoT, simulation, and remote sensing data analysis can constitute a general and reusable approach to continuous environmental monitoring. The frameworks and datasets produced represent a solid foundation for future studies, as well as for scientific, operational, and decision-support activities aimed at promoting more sustainable management of agro-livestock practices and their impacts on ecosystems.

Acknowledgements

I would like to express my sincere gratitude to all the people who accompanied me throughout my doctoral studies and made this important experience possible, allowing me to successfully complete this valuable opportunity for professional growth.

First and foremost, I would like to thank my supervisor, Prof. Marko Bertogna, who welcomed me three years ago and encouraged me to undertake this stimulating research project at the FIM Department of the University of Modena and Reggio Emilia. I am grateful for his continuous support in major decision-making processes and in all administrative matters, including access to research funding; for closely following the progress of my work, including my publications; and for authorizing my participation in the various initiatives during my doctoral journey. I am also thankful to him for suggesting a highly valuable tutor.

I would like to extend my heartfelt thanks to my tutor, Prof. Marco Picone, for his constant support, for the invaluable scientific discussions, and for the scientific and technical advice provided throughout my research activities. I am deeply grateful to him for his meticulous and patient guidance in teaching me how to write publications worthy of submission, including his fundamental contribution to the writing and revision of this thesis. I also thank him for his guidance in selecting research projects to pursue, conferences to attend,

and journals to which to submit our work.

I would also like to thank the Coordinator of the PhD Program, Prof. Andrea Marongiu, for carrying out his role with great professionalism, ensuring that all students received the essential support needed to comply with the required administrative obligations and for organizing very interesting and enjoyable academic events. I would like to thank Prof. Antonio Virdis and Prof. Carlo Giannelli for kindly reading and reviewing my thesis. I am also grateful to all the doctoral students with whom I shared the lectures of the fifteen courses attended during the first two years of the program. In particular, I would like to mention Federico Motta and Andrea Artioli (student representative) for their help and advice whenever I needed it, as well as for their encouragement during some challenging moments in my first year of study.

I would also like to acknowledge the value of the Earth Engine satellite data processing platform and express my gratitude to Google for providing it to the scientific community. This resource enabled me to carry out the remote sensing project, free of charge, and successfully complete the final part of my research work, which can be considered the "cherry on the cake."

I thank all of you for these three years, which have brought me great satisfaction and of which I will always be proud. I will strive to carry this enthusiasm with me into the educational community to which I now return.

Bibliography

[1] Putu Abel Nugraha Ardyan and Redondo. Water turbidity qualitative analysis based on sentinel imagery in jeneberang river downstream, makassar, south sulawesi. *IOP Conference Series: Earth and Environmental Science*, 1525(1):012028, jul 2025.

[2] Laura Agneessens, Jeroen De Waele, and Stefaan De Neve. Review of alternative management options of vegetable crop residues to reduce nitrate leaching in intensive vegetable rotations. *Agronomy*, 4:529–555, 12 2014.

[3] Nat assia Jersak Cosmann, Silvio C. Sampaio, F G da S Pinto, Denise Palma, Jonathan Dieter, Meindl Claudia, S. Cordovil, and Amarílis de Varennes. Transport of nutrients and bacteria in runoff after the application of swine wastewater. In *2012 International Journal of Food, Agriculture and Environment (JFAE)*, 2012.

[4] Analy Baltodano, Afnan Agramont, Ils Reusen, and Ann van Griensven. Land cover change and water quality: How remote sensing can help understand driver–impact relations in the lake titicaca basin. *Water*, 14(7), 2022.

[5] M. Bartoli, M. Faggioli, E. Severini, C. Ferrari, J. Bianchetti, M. Lanzoni, M. Magri, M. Pinardi, B. Grandi, and R. Bolpagni. Analisi ecologiche e misure di portata per la definizione dei fattori correttivi nel calcolo dei deflussi nel mincio e la calibrazione dei sistemi di misura. In *Valli Del Mincio - Un Delicato Equilibrio*, 2022.

[6] Francisco Bautista, Yameli Aguilar, and E. Diaz-Pereira. Soils as natural reactors for swine wastewater treatment. *Tropical and Subtropical Agroecosystems*, 13, 01 2011.

[7] Wondimagegn T Beshah, Jane Moorhead, Padmanava Dash, Robert J. Moorhead, James Herman, M. S. Sankar, Daniel Chesser, Wes Lowe, Jessica Simmerman, and Gray Turnage. Iot based real-time water quality monitoring and visualization system using an autonomous surface vehicle. In *OCEANS 2021: San Diego – Porto*, pages 1–4, 2021.

[8] Sumanta Bid and Giyasuddin Siddique. Identification of seasonal variation of water turbidity using NDTI method in panchet hill dam, india. *Modeling Earth Systems and Environment*, 5, 12 2019.

[9] Joann Burkholder, Bob Libra, Peter Weyer, Susan Heathcote, Dana Kolpin, Peter Thorne, and Michael Wichman. Impacts of waste from concentrated animal feeding operations on water quality. *Environmental health perspectives*, 115:308–12, 03 2007.

[10] Zhen Cao, Yuchao Zhang, Zhaomin Liu, Baohua Guan, Lai Lai, Qiduo Yang, and Xi Chen. Recent decade expansion of aquatic vegetation covering in china's lakes. *Ecological Indicators*, 159:111603, 2024.

[11] Jana Chovancova. Economical and ecological consequences of the management of biological wastes arising in the intensive agricultural livestock production. Master's thesis, Sumy State University, 2014.

[12] European Commission. Waste framework directive, 2023.

[13] Amine Dahane, Rabaie Benameur, Manel Naloufi, Sami Souihi, Thiago Abreu, Françoise S. Lucas, and Abdelhamid Mellouk. Iot urban river water quality system using federated learning via knowledge distillation. *ICC 2024 - IEEE International Conference on Communications*, pages 1515–1520, 2024.

[14] André Doblinski, Silvio Sampaio, Lúcia Nóbrega, Simone Gomes, and Tatiane Bosco. Nonpoint source pollution by swine farming wastewater in bean crop. *Revista Brasileira de Engenharia Agrícola e Ambiental*, 14, 01 2010.

[15] Baili Dong, Yongqiang Zhou, Erik Jeppesen, Boqiang Qin, and Kun Shi. Six decades of field observations reveal how anthropogenic pressure changes the coverage and community of submerged aquatic vegetation in a eutrophic lake. *Science of The Total Environment*, 842:156878, 2022.

[16] ERSAF Lombardia. Gestione sostenibile dei nitrati in agricoltura. `https://www.ersaf.lombardia.it/agricoltura/gestione-sostenibile-dei-nitrati`, 2022. Accessed: 2026-03-09.

[17] The Python Software Foundation. The python official site, 2025.

[18] Gustavo Furquim, Geraldo P. R. Filho, Roozbeh Jalali, Gustavo Pessin, Richard W. Pazzi, and Jó Ueyama. How to improve fault tolerance in

disaster predictions: A case study about flash floods using iot, ml and real data. *Sensors (Switzerland)*, 18(3), 2018. Cited by: 49; All Open Access, Gold Open Access, Green Open Access.

[19] Romeu Gerardo and Isabel P. de Lima. Monitoring duckweeds (lemna minor) in small rivers using sentinel-2 satellite imagery: Application of vegetation and water indices to the lis river (portugal). *Water*, 2022.

[20] Lorenzo Gianquintieri, Daniele Oxoli, Enrico Gianluca Caiani, and Maria Antonia Brovelli. Implementation of a geoai model to assess the impact of agricultural land on the spatial distribution of pm2.5 concentration. *Chemosphere*, 352:141438, 2024.

[21] A. Arun Gnanaraj and J. Gnana Jayanthi. An application framework for iots enabled smart agriculture waste recycle management system. In *2017 World Congress on Computing and Communication Technologies (WCCCT)*, pages 1–5, 2017.

[22] Megan Gomes, Timothy J. Ralph, Marc S. Humphries, Bradley P. Graves, Tsuyoshi Kobayashi, and Damian B. Gore. Waterborne contaminants in high intensity agriculture and plant production: A review of on-site and downstream impacts. *Science of The Total Environment*, 958:178084, 2025.

[23] Google. Earth engine code editor, 2025.

[24] Google. Earth engine data catalog, 2025.

[25] Google. Google earth engine, 2025.

[26] Dagne Hill, William Owens, and Paul Tchoounwou. Impact of animal waste application on runoff water quality in field experimental plots.

International journal of environmental research and public health, 2:314–21, 09 2005.

[27] Xuejiao Hou, Lian Feng, Xiaoling Chen, and Yunlin Zhang. Dynamics of the wetland vegetation in large lakes of the yangtze plain in response to both fertilizer consumption and climatic changes. *ISPRS Journal of Photogrammetry and Remote Sensing*, 141:148–160, 2018.

[28] Mohammad Ariful Islam Khan, Mohammad Akidul Hoque, and Sabbir Ahmed. Iot-based system for real-time water pollution monitoring of rivers. 2021. Cited by: 10.

[29] Paul Jansen. The tiobe programming community index, 2025.

[30] Poornima Jayaraman, Kothalam Krishnan Nagarajan, and Pachaivannan Partheeban. Smart water quality monitoring using iot for metropolitan city lakes. *Environmental Engineering and Management Journal*, 24(8):1705 – 1721, 2025. Cited by: 0.

[31] Won Seok Ju, Seokho Kim, Jae-Yeong Lee, Haesun Lee, Jingu No, Seunghoon Lee, and Keonbong Oh. Gene editing for enhanced swine production: Current advances and prospects. *Animals*, 15(3), 2025.

[32] Bong-Hyun Kim and Ju-Ri Kim. Implementation of smart agricultural water management system using iot-based remote monitoring. *International Journal of Advanced Science and Technology*, 28(5):44 – 52, 2019. Cited by: 3.

[33] Seung-Hee Kim, Dong-Hun Lee, Min-Seob Kim, Han-Pil Rhee, Jin Hur, and Kyung-Hoon Shin. Systematic tracing of nitrate sources in a complex river catchment: An integrated approach using stable isotopes and hydrological models. *Water Research*, 235:119755, 2023.

[34] Avantika Latwal, Shaik Rehana, and K.S. Rajan. Spatiotemporal analysis of turbidity in tropical reservoirs using sentinel-2 satellite imagery under catchment dynamics. *Remote Sensing Applications: Society and Environment*, 39:101631, 2025.

[35] LEGAMBIENTE. Mal'aria di cittÀ, 2025.

[36] Regione Lombardia. Normativa nitrati in regione lombardia, 2022.

[37] Lin LU, Xiu dong LIAO, and Xu gang LUO. Nutritional strategies for reducing nitrogen, phosphorus and trace mineral excretions of livestock and poultry. *Journal of Integrative Agriculture*, 16(12):2815–2833, 2017.

[38] Juhua Luo, Ruiliang Pu, Hongtao Duan, Ronghua Ma, Zhigang Mao, Yuan Zeng, Linsheng Huang, and Qitao Xiao. Evaluating the influences of harvesting activity and eutrophication on loss of aquatic vegetations in taihu lake, china. *International Journal of Applied Earth Observation and Geoinformation*, 87:102038, 2020.

[39] María López, Javier García, et al. The identification of manure spreading on bare soil through the development of multispectral indices from sentinel-2 data. *Remote Sensing*, 16(12):2150, 2024.

[40] Yagoub M. M., Yacob Tesfaldet, Marwan Elmubarak, and Naeema Hosani. Extraction of urban quality of life indicators using remote sensing and machine learning: The case of al ain city, united arab emirates (uae). *ISPRS International Journal of Geo-Information*, 11:458, 08 2022.

[41] Daniele Malferrari, Angela Laurora, Maria Brigatti, Massimo Coltorti, Dario Giuseppe, Barbara Faccini, Elio Passaglia, and Giovanna Vezzalini. Open-field experimentation of an innovative and integrated zeolitite

cycle: Project definition and material characterization. *Rendiconti Lincei-Scienze Fisiche E Naturali*, 24:141–150, 06 2013.

[42] Michael A. Mallin and Lawrence B. Cahoon. Industrialized animal production—a major source of nutrient and microbial pollution to aquatic ecosystems. *Population and Environment*, 24(5):369–385, May 2003.

[43] Devesh Mishra, Tanuja Pande, Krishna Kant Agrawal, Ali Abbas, Akhilesh Kumar Pandey, and Ram Suchit Yadav. Smart agriculture system using iot. In *Proceedings of the Third International Conference on Advanced Informatics for Computing Research*, ICAICR '19, New York, NY, USA, 2019. Association for Computing Machinery.

[44] George Mois, Silviu Folea, and Teodora Sanislav. Analysis of three iot-based wireless sensors for environmental monitoring. *IEEE Transactions on Instrumentation and Measurement*, 66(8):2056–2064, 2017.

[45] Alexandre Moura, SILVIO SAMPAIO, Marcelo Remor, ADRIANA SILVA, and Pâmela Maldaner Pereira. Long-term effects of swine wastewater and mineral fertilizer association on soil microbiota. *Engenharia Agrícola*, 36:318–328, 04 2016.

[46] Urs Niggli, Andreas Fliessbach, Paul Hepperly, and Nadia Scialabba. Low greenhouse gas agriculture: Mitigation and adaptation potential of sustainable farming systems. *Ökologie & Landbau*, 141, 01 2009.

[47] Jacineumo Oliveira, Fernando Rodrigues, Ronaldo Fia, Dayana Cristine Mafra, and Daniela Landim. Percolate quality in soil cultivated with application of wastewater from swine slaughterhouse and dairy products. *Engenharia Agrícola*, 37:1222–1235, 12 2017.

[48] Dr. Bhagwati Patel, Ram Tripathi, and Naveen Goel. Iot an overview: Advantage, disadvantage and applications. *International Journal of Computer Applications Technology and Research*, 10:119–122, 05 2021.

[49] Tuyen Phong Truong, Bao Duc Le, and Hoang Huu Nguyen. An iot-based water level monitoring and management system for open ditch drainage. page 109 – 115, 2022. Cited by: 0.

[50] M.C.K. Pinto, R.L. Cruz, E.P. Frigo, M.S. Frigo, and E. Hermes. Nitrogen groundwater contamination consequential of irrigation with effluent from sewage treatment. *IRRIGA*, 18:270–281, 01 2013.

[51] Plant Research International. *N management in agrosystems in relation to the Water Framework Directive*, Maastricht, 2005.

[52] Anton Prafanto and Edy Budiman. A water level detection: Iot platform based on wireless sensor network. page 46 – 49, 2018. Cited by: 22.

[53] Devendra Prasad, Afshan Hassan, Deepak Kumar Verma, Pradeepta Sarangi, and Sunny Singh. Disaster management system using wireless sensor network: A review. 2021. Cited by: 11.

[54] Annette Pronk and Marius Heinen. Increased plant density to increase nitrogen use efficiency and reduce nitrate losses. 01 2006.

[55] Song Qing, Runa A, Buri Shun, Wenjing Zhao, Yuhai Bao, and Yanling Hao. Distinguishing and mapping of aquatic vegetations and yellow algae bloom with landsat satellite data in a complex shallow lake, china during 1986–2018. *Ecological Indicators*, 112:106073, 2020.

[56] Regione Campania. Piano dei controlli sull'utilizzazione agronomica degli effluenti di allevamento. https://agricoltura.regione.campania.it/reflui/piano-controlli.html, 2021. Accessed: 2026-03-09.

[57] Regione Lombardia. Direttiva nitrati: monitoraggio della corretta applicazione. https://www.regione.lombardia.it/wps/portal/istituzionale/HP/DettaglioRedazionale/servizi-e-informazioni/Imprese/Imprese-agricole/direttiva-nitrati/monitoraggio-corretta-applicazione-direttiva-nitrati, 2022. Accessed: 2026-03-09.

[58] P. Rekha, K. Sumathi, S. Samyuktha, A. Saranya, G. Tharunya, and R. Prabha. Sensor based waste water monitoring for agriculture using iot. In *2020 6th International Conference on Advanced Computing and Communication Systems (ICACCS)*, pages 436–439, 2020.

[59] Dr. Samapriya Roy. The awesome gee community catalog, 2025.

[60] Jalpa Shah and Biswajit Mishra. Iot enabled environmental monitoring system for smart cities. In *2016 International Conference on Internet of Things and Applications (IOTA)*, pages 383–388, 2016.

[61] Naresh Sharma and Rohit Sharma. Real-time monitoring of physicochemical parameters in water using big data and smart iot sensors. *Environment, Development and Sustainability*, 26(9):22013 – 22060, 2024. Cited by: 24.

[62] Acbang Caya Shyra. Effects of manure and fertilizer on soil fertility and soil quality, 2013.

[63] Elisa Soana, Erica Racchetti, Alex Laini, Marco Bartoli, and Pierluigi Viaroli. Soil budget, net export, and potential sinks of nitrogen in the lower oglio river watershed (northern italy). *CLEAN – Soil, Air, Water*, 39:956 – 965, 11 2011.

[64] S.G. Sommer. *Animal Manure - From Waste to Raw Materials and Goods*, pages 1–4. Wiley, 07 2013.

[65] Jose Antonio Souza, Débora Moreira, Rafael Batista, Alexander Osorio Saraz, and Olga Marín. Chemical alterations in soils fertirrigated with wastewater from swine facilities. *Revista Colombiana de Ciencias Pecuarias*, 25:360–368, 09 2012.

[66] Chao Sun, Jialin Li, Luodan Cao, Yongchao Liu, Song Jin, and Bingxue Zhao. Evaluation of vegetation index-based curve fitting models for accurate classification of salt marsh vegetation using sentinel-2 time-series. *Sensors*, 20(19), 2020.

[67] Yedla Suneetha and Mareddy Reddy. Spatial and temporal analysis of landsat data to retrieve the ndwi, ndvi and land surface temperature by thermal remote sensor: A case study of hyderabad metropolitan city, telangana. *E3S Web of Conferences*, 472, 01 2024.

[68] The SWOT Science Team. Swot river database (sword), 2025.

[69] Giovanni Triboli, Marco Picone, and Marko Bertogna. Integrating iot and simulation for efficient livestock waste spread in the po valley. In *2024 28th International Symposium on Distributed Simulation and Real Time Applications (DS-RT)*, pages 144–145, 2024.

[70] Giovanni Triboli, Marco Picone, and Marko Bertogna. Intelligent livestock waste sensing & management: Architecture and challenges in the po

valley. In *2024 IEEE Symposium on Computers and Communications (ISCC)*, pages 1–6, 06 2024.

[71] Giovanni Triboli, Marco Picone, and Marko Bertogna. Satellite-based processing pipeline for vegetation assessment in water bodies and urban landscapes. In *2025 21st International Conference on Distributed Computing in Smart Systems and the Internet of Things (DCOSS-IoT)*, pages 952–959, 2025.

[72] Emanuela Tullo, Alberto Finzi, and Marcella Guarino. Review: Environmental impact of livestock farming and precision livestock farming as a mitigation strategy. *Science of The Total Environment*, 650:2751–2760, 2019.

[73] Murat Uzun. Analysis of manyas lake surface area and shoreline change over various periods with DSAS tool. *Turkish Journal of Remote Sensing*, 6:35–56, 04 2024.

[74] A Vasanthi and K. Joshitha. Water body detection utilizing ndwi, ndvi and nmdwi indices in sen-12 spectral imagery. In *2024 First International Conference on Electronics, Communication and Signal Processing (ICECSP)*, pages 1–5, 08 2024.

[75] Yaroslav Vasyunin. y-vasyunin/ee-ita-lago-fimon: Monitor aquatic plants from space: the case of lake fimon, April 2022.

[76] Gerard Velthof, Sébastien Barot, Jaap Bloem, Klaus Butterbach-Bahl, Wim Vries, Johannes Kros, Patrick Lavelle, Jørgen Olesen, and Oene Oenema. *Nitrogen as a threat to European soil quality*, pages 495–510. Cambridge University Press, 04 2011.

[77] Gerard L. Velthof, Daniel Oudendag, et al. A broad-scale spatial analysis of the environmental benefits of fertiliser closed periods implemented under the nitrates directive in europe. *Journal of Environmental Management*, 303:114132, 2022.

[78] G.L. Velthof, Andre Bannink, O. Oenema, H.G. Meer, and S.F. Spoelstra. Relationships between animal nutrition and manure quality; a literature review on c, n, p and s compounds. *Wageningen, Alterra, 2000. Alterra-rapport 063, 44 pp*, 01 2000.

[79] Paolo Villa, Monica Pinardi, Rossano Bolpagni, Jean-Marc Gillier, Peggy Zinke, Florin Nedelcuţ, and Mariano Bresciani. Assessing macrophyte seasonal dynamics using dense time series of medium resolution satellite data. *Remote Sensing of Environment*, 216:230–244, 2018.

[80] Huaijing Wang, Yunmei Li, Shuai Zeng, Xiaolan Cai, Shun Bi, Huaiqing Liu, Meng Mu, Xianzhang Dong, Junda Li, Jiafeng Xu, Heng Lyu, Yuxin Zhu, and Yu Zhang. Recognition of aquatic vegetation above water using shortwave infrared baseline and phenological features. *Ecological Indicators*, 136:108607, 2022.

[81] Farmers Weekly. What farmers need to do to use sewage sludge safely, 2018.

[82] Qiusheng Wu. The geemap official site, 2025.

[83] Jinru Xue and Baofeng Su. Significant remote sensing vegetation indices: A review of developments and applications. *Journal of Sensors*, 2017:1–17, 05 2017.

[84] Jining Yan and Lizhe Wang. Suitability evaluation for products generation from multisource remote sensing data. *Remote Sensing*, 8(12), 2016.

[85] Gang Yang, Ke Huang, Weiwei Sun, Xiangchao Meng, Dehua Mao, and Yong Ge. Enhanced mangrove vegetation index based on hyperspectral images for mapping mangrove. *ISPRS Journal of Photogrammetry and Remote Sensing*, 189:236–254, 2022.

[86] Xin Zhang, Ya'nan Zhou, and Jiancheng Luo. Deep learning for processing and analysis of remote sensing big data: a technical review. *Big Earth Data*, 6(4):527–560, 2022.

[87] Ziqian Zhu, Xin Li, Qiurong Bu, Qingcheng Yan, Liqun Wen, Xiaolei Chen, Xiaodong Li, Ming Yan, Longbo Jiang, Gaojie Chen, Shuai Li, Xiang Gao, Guangming Zeng, and Jie Liang. Land–water transport and sources of nitrogen pollution affecting the structure and function of riverine microbial communities. *Environmental Science & Technology*, 57(7):2726–2738, 2023. PMID: 36746765.